

EXPERIMENTAL INVESTIGATION OF FUNDAMENTAL VISCOSITY, DENSITY,
AND LEACHING CHARACTERISTICS OF SODIUM-IRON-SILICATE SLAGS

by
Doug Schriener

A thesis submitted to the Faculty and the Board of Trustees of the Colorado School of Mines in partial fulfillment of the requirements for the degree of Doctor of Philosophy (Metallurgical and Materials Engineering).

Golden, Colorado

Date _____

Signed: _____

Doug Schriner

Signed: _____

Dr. Patrick Taylor
Thesis Advisor

Golden, Colorado

Date _____

Signed: _____

Dr. Angus Rockett
Professor and Head
Department of Metallurgical and Materials Engineering

ABSTRACT

Environmental regulations govern the emission of sulfur dioxide for lead smelters. Because of this, some have adopted a hydrometallurgical desulfurization step, which results in a sodium-iron-silicate slag being generated in their furnaces. This slag must be disposed of, but the behavior of impurities from the solidified slag and the physical properties of the molten phase are not well understood. In this work, the leaching characteristics, viscosity, and density of a sodium-iron-silicate system representing a modern secondary lead smelter's slag have been studied.

Slag viscosity increased with decreasing temperature and increasing silica content. At constant silica content, more iron led to a higher viscosity while more sodium led to a lower viscosity. An Arrhenius-type model was produced to predict slag viscosity as a function of composition and temperature. It showed good agreement between predicted and measured values. Density measurements conducted by this study were not precise enough to establish trends with temperature or composition.

The slag samples tested in this study formed iron oxides and sodium silicates upon cooling. Satmagan analysis suggested the iron was mostly, but not completely reduced ($\text{Fe}^{3+}/\Sigma\text{Fe} = 0.167$). The impurities formed barium silicates and sodium-barium-silicates, lead silicates, and sodium arsenates.

In the composition region studied, the samples with more silicon tended to leach less. Further investigation revealed that compositions in the center of the phase diagram (not simply those with less silica) produced extracts with the highest concentration of barium (which exceeded the TCLP regulatory limits). Similarly-high extract concentrations were seen with lead and arsenic from the same high-sodium composition. Composition appears to be a more significant predictor of the extract impurity concentration than temperature in the moderate range of cooling rates. However, when quenching and extra-slow cooling are considered, the cooling rate becomes significant. Barium concentrations were higher for the high-sodium samples which had been cooled more slowly. Quenching, however, can lead to morphological effects which can be detrimental when high-silicon compositions are used.

Relating the two phenomena, the compositions which had the lowest viscosities also leached the most. While this would be beneficial for phase separation (as viscosity is in the denominator for terminal velocity of a sphere in a fluid), the leaching characteristics of this slag when solidified would be industrially undesirable. An economic incentive for avoiding this region is that increasing the TCLP pass rate will reduce the expense of hazardous slag disposal. By increasing the TCLP pass rate by 25%, daily profit can be increased by 2.43%.

TABLE OF CONTENTS

ABSTRACT.....	iii
LIST OF FIGURES	viii
LIST OF TABLES	xii
ACKNOWLEDGMENTS	xiv
DEDICATION	xv
CHAPTER ONE INTRODUCTION	1
CHAPTER TWO LEAD PROCESSING	2
2.1 Traditional Lead Processing	2
2.1.1 Reverberatory Furnaces	2
2.1.2 Blast Furnaces	4
2.1.3 Containing the Blast Furnace melt:.....	5
2.2 Primary Operations	6
2.3 Modern Secondary Lead Processing	11
CHAPTER THREE SLAG FUNDAMENTALS	13
3.1 Liquid Slag Structure.....	13
3.1.1 Theory and Fundamentals.....	13
3.1.2 Empirical Investigations of Molten Slag Structure.....	16
3.2 Viscosity	17
3.2.1 Theory and Fundamentals of Viscosity Measurement.....	22
3.2.2 Empirical Investigations of Viscosity	24
3.3 Density.....	30
3.3.1 Theory and Fundamentals of Density Measurement	31
3.3.2 Empirical Investigations of Density.....	33
3.4 Solid Slag Structure	35
3.4.1 Phase Separation	35

3.4.2	Phase Diagrams of Relevant Oxide Systems	38
3.4.2.1	Na ₂ O-FeO.....	39
3.4.2.2	Na ₂ O-SiO ₂	39
3.4.2.3	FeO-SiO ₂	40
3.4.2.4	BaO-SiO ₂	40
3.4.2.5	PbO-SiO ₂	42
3.4.2.6	As ₂ O ₃ -SiO ₂	42
3.4.2.7	Na ₂ O-FeO-SiO ₂	42
3.4.2.8	Na ₂ O-BaO-SiO ₂	46
3.4.2.9	Na ₂ O-PbO-SiO ₂	48
3.4.2.10	Other Oxide Systems.....	48
3.4.3	Empirical Investigations of Solidified Slags.....	49
3.5	Environmental Behavior.....	52
3.5.1	Toxicity Characteristic Leaching Procedure (TCLP)	53
3.5.2	Empirical Investigations of Slag Environmental Behavior.....	54
CHAPTER FOUR EXPERIMENTAL METHODS AND MATERIALS		56
4.1	Selection of Slag Recipes	56
4.2	Thermodynamic Modeling	57
4.3	Measurement of Viscosity and Density	57
4.4	Determination of Leaching Characteristics	58
4.5	Analytical Techniques	59
4.5.1	ICP-OES	59
4.5.2	Microscopy and Spectroscopy	60
4.5.3	Satmagan Analysis.....	60
CHAPTER FIVE EXPERIMENTAL QUALITY CONTROL		62
5.1	Slag Composition	62
5.1.1	Reagent Purity.....	62

5.1.2	Crucible Interactions	62
5.1.3	Before-and-after Comparison	65
5.2	Furnace Environments	66
5.2.1	Temperature Verification and Profiles.....	66
5.2.2	Establishment of Protective Atmosphere	68
5.3	TCLP Slag Preparation	68
5.4	Calibration of Instruments	68
5.4.1	Viscometer Calibration	68
5.4.2	Balance Calibration.....	70
5.4.3	Satmagan Calibration.....	71
5.5	Discussion of Errors	72
5.5.1	Viscosity	72
5.5.2	Density	74
5.5.3	Leaching Results.....	76
CHAPTER SIX RESULTS AND DISCUSSION		77
6.1	Viscosity Tests.....	77
6.2	Density Tests	84
6.3	TCLP Slag Preparation.....	86
6.4	Phase Analysis.....	88
6.4.1	Satmagan Analysis.....	88
6.4.2	Predicted Equilibrium Phases	88
6.4.3	Spectroscopic Analysis	91
6.5	TCLP Leach Tests	99
CHAPTER SEVEN ECONOMIC ANALYSIS		106
CHAPTER EIGHT CONCLUSIONS		108
CHAPTER NINE RECOMMENDATIONS FOR FUTURE WORK.....		109
REFERENCES		110

APPENDIX A VISCOSITY DATA.....	115
APPENDIX B DENSITY DATA.....	122
APPENDIX C TCLP SAMPLE DATA.....	124

LIST OF FIGURES

Figure 2.1	Schematic of a Lead Blast Furnace.....	5
Figure 2.2	Cutaway of a Lead-Acid battery. From [4].....	11
Figure 2.3	Lead-Acid Battery Recycling Flowsheet. From [5].....	12
Figure 3.1	The structure of silica (crystalline, left; molten, right). From [11]	14
Figure 3.2	Illustration of a divalent metal oxide in molten silica. From [11].....	15
Figure 3.3	Abundance of anionic structural units in binary metal oxide-silica systems as a function of Z/r^2 of the metal cation for bulk melt NBO/Si-values as indicated in the figure. From [14].....	18
Figure 3.4	Shear Stress – Strain Rate relationships for various fluid types. Adapted from [11].....	19
Figure 3.5	Applicable ranges for methods and materials used in the study of viscosity. From [23].....	24
Figure 3.6	Viscosity of Alkali Silicates. From [28]	25
Figure 3.7	Activation Energy for Viscous Flow in Alkali and Alkaline-Earth Silicates. From [29].....	25
Figure 3.8	Graphic representation of experimental points used by Dingwell and Virgo. [32].....	26
Figure 3.9	Viscosity as a function of ferric iron to total iron in Acmite and NS4F40 melts. Adapted From [17].....	27
Figure 3.10	Viscosity as a function of ferrous to total iron. From [33].....	28
Figure 3.11	Viscosity as a function of temperature, immersion depth, and spindle RPM. Adapted from [35]	29
Figure 3.12	Illustration of an object's apparent weight as it is lowered into a fluid.....	32
Figure 3.13	Illustration of Free Energy Changes Associated with Growth of a Spherical Particle. From top to bottom, the lines represent the surface energy contribution, the total free energy, and the volumetric energy contribution.....	37
Figure 3.14	Rate Components' Contributions to Nucleation. From [50].....	38
Figure 3.15	Generalized TTT-Diagram for a phase transformation. From [50].....	38
Figure 3.16	Calculated optimized FeO-Na ₂ O phase diagram. From [51].	39
Figure 3.17	Calculated Na ₂ O-SiO ₂ phase diagram showing presently calculated and previously reported (in parentheses and brackets) temperatures. From [52].	40
Figure 3.18	Calculated FeO-SiO ₂ phase diagram. From [53].	41
Figure 3.19	Calculated BaO-SiO ₂ phase diagram. From [54]	41
Figure 3.20	The PbO-SiO ₂ phase diagram. From [55].	42

Figure 3.21	The $\text{As}_2\text{O}_3\text{-SiO}_2$ phase diagram. From [55]	43
Figure 3.22	Primary Phase Regions with Experimental Points in the $\text{Na}_2\text{O-FeO-SiO}_2$ System. From [56]	44
Figure 3.23	$\text{FeO-Na}_2\text{O-SiO}_2$ Phase Diagram, based on Schairer, Yoder, and Keene. From [57]	44
Figure 3.24	Calculated Primary Phase Regions and Previous Experimental Points in the $\text{Na}_2\text{O-FeO-SiO}_2$ System. From [51]	45
Figure 3.25	Calculated Liquidus Contours (in °C) and Primary Phase Regions for the $\text{Na}_2\text{O-FeO-SiO}_2$ System. From [51]	46
Figure 3.26	Calculated Primary Phase Regions and Previous Experimental Points in the $\text{Na}_2\text{O-Fe}_2\text{O}_3\text{-SiO}_2$ System. From [51]	47
Figure 3.27	Calculated Liquidus Contours (in °C) and Primary Phase Regions for the $\text{Na}_2\text{O-Fe}_2\text{O}_3\text{-SiO}_2$ System. From [51]	47
Figure 3.28	Primary Phase Regions with Liquidus Contours for the $\text{Na}_2\text{O-BaO-SiO}_2$ System. From [58]	48
Figure 3.29	Approximation of the liquidus projection of the $\text{Na}_2\text{O-PbO-SiO}_2$ system. From [55].....	49
Figure 3.30	SEM backscattered images of desulfurized reverb-blast slag. Left: 200X magnification silicate matrix. Right: 620X, enlargement of upper-right corner of right image.	50
Figure 3.31	Relationship between Grain Diameter and Particle Density. From [66].....	51
Figure 3.32	SEM images of a secondary lead slag. From [65].....	52
Figure 4.1	Experimental Points presented in the $\text{Na}_2\text{O-FeO-SiO}_2$ ternary space. TCLP tests' labels are bold, successful viscosity tests' labels are <i>italicized</i> , and unsuccessful viscosity tests' labels are red.....	56
Figure 4.2	A Batch of Powder-Filled Crucibles Ready to be Heated.....	58
Figure 5.1	TGA curves for (I) recrystallized barium hydroxide octahydrate and (II) barium hydroxide octahydrate prepared by the rehydration of the monohydrate. From [72]	63
Figure 5.2	Bottom Face of Slag Contained in a Graphite Crucible. Regions of reduced iron are circled in red.....	64
Figure 5.3	Silicon Carbide Crucible Coated with Boron Nitride. From left to right: before heating slag, immediately after heating slag to 1200 °C, and after cooling to room temperature.....	64
Figure 5.4	Two Crucibles Coated with Different Castable Refractory Compounds Containing a Slag, after heating.	65
Figure 5.5	Alumina Crucible Containing a Slag After Heating. Discoloration due to slag wetting a crack is indicated with red arrows.....	65
Figure 5.6	Tube furnace temperature versus height profile.....	67

Figure 5.7	Box furnace temperature versus time profile.	67
Figure 5.8	Viscosity of Brookfield 5,000-cP standard oil.	69
Figure 5.9	Viscosity of B ₂ O ₃ . Lines represent data taken from Napolitano <i>et al.</i> (from [74]), while points represent experimental observations from this study.	70
Figure 5.10	Satmagan Calibration Curve.	71
Figure 5.11	Viscosity as a function of RPM for Sample 1.	73
Figure 5.12	Ratio of Slurry Viscosity to Carrier Fluid Viscosity as a function of Solids Content. From [75]	75
Figure 5.13	Slag Adhesion to Spindle After (from top to bottom) Tests 1, 8, and 13.	75
Figure 6.1	Shear Stress versus Shear Rate for Sample 1.	77
Figure 6.2	Logarithm of Viscosity as a function of inverse absolute temperature for Sample 1.	78
Figure 6.3	Logarithm of Viscosity as a function of inverse absolute temperature for all tests.	79
Figure 6.4	Calculated Versus Measured Viscosity.	82
Figure 6.5	Calculated versus Measured Viscosity with Emphasis on Current Study Data.	82
Figure 6.6	Overlay of Experimental Points and Projected Liquidus Contours.	83
Figure 6.7	Calculated Densities using Parameters from Lange and Carmichael. [43]	85
Figure 6.8	Predicted and Experimental Densities Ordered by Predicted Density.	86
Figure 6.9	Prepared Slags.	87
Figure 6.10	Poured Slags. From Left, Slags N, F, S, and M.	87
Figure 6.11	XRD Pattern for a Slow-Cooled, High-Silica Sample.	91
Figure 6.12	XRD Pattern for a Slow-Cooled, High-Iron Sample.	92
Figure 6.13	XRD Pattern for a Slow-Cooled, High-Sodium Sample.	92
Figure 6.14	XRD Pattern for a Slow-Cooled, Middle-Composition Sample.	93
Figure 6.15	XRD Pattern for a Fast-Cooled, High-Silica Sample.	93
Figure 6.16	XRD Pattern for a Fast-Cooled, High-Iron Sample.	94
Figure 6.17	XRD Pattern for a Fast-Cooled, High-Sodium Sample.	94
Figure 6.18	XRD Pattern for a Fast-Cooled, Middle-Composition Sample.	95
Figure 6.19	EDS Maps for Slow-Cooled High-Sodium Sample Doped with 8.84 wt% Barium Oxide.	96
Figure 6.20	EDS Maps for Slow-Cooled High-Sodium Sample Doped with 5 wt% Lead Oxide.	96
Figure 6.21	EDS Maps for Slow-Cooled High-Sodium Sample Doped with 5 wt% Arsenic Trioxide.	97

Figure 6.22	Secondary Electron Image of Barium-Doped High-Sodium Sample before (left) and after (right) Leaching.	97
Figure 6.23	Barium EDS Map of Barium-Doped High-Sodium Sample before (left) and after (right) Leaching.....	98
Figure 6.24	Barium EDS Map of Barium-Doped High-Silica Sample before (left) and after (right) Leaching.....	98
Figure 6.25	TCLP Leach Results for Barium.....	99
Figure 6.26	TCLP Leach Results for Lead.....	100
Figure 6.27	TCLP Leach Results for Arsenic.	100
Figure 6.28	TCLP Leach Results (in ppm) for Barium (blue), Lead (red), and Arsenic (green) overlaid on the Na ₂ O-FeO-SiO ₂ ternary diagram. Lead values are centered on the tests' targeted mole percent compositions.	101
Figure 6.29	TCLP Leach Results (in ppm) for all Barium tests. Values are centered on the tests' targeted mole percent compositions.....	102
Figure 6.30	Pseudo-Binary Phase Diagrams for FeO-Na ₂ SiO ₃ (left) and Fe ₂ SiO ₄ -Na ₄ SiO ₄ (right).....	102
Figure 6.31	Overlay of TCLP Experimental Points onto Liquidus Contours. The dashed line is the Fe ₂ SiO ₄ -Na ₂ SiO ₄ join and the solid line is the FeO-Na ₂ SiO ₃ join.....	103
Figure 6.32	Image of Quenched Samples N (left) and S (right), taken after drying.	104
Figure 7.1	Daily Profit Sensitivity Analysis.....	106
Figure 7.2	Daily Profit Sensitivity Analysis, Excluding Lead Price and Throughput.....	107

LIST OF TABLES

Table 2.1	North American Lead Smelting Operations and Capacities. From [1]	3
Table 2.2	Composition of a Reverb Slag	4
Table 2.3	Representative Charge Compositions	7
Table 2.4	Typical Analyses of Materials Charged.....	8
Table 2.5	Typical Analyses of Smelter Products	9
Table 3.1	Structural Relationships in basic oxide-silicate melts. Adapted from [11].....	15
Table 3.2	Arrhenius constants for sodium-iron-silicate melts. From [32]	27
Table 3.3	Results of curve-fitting procedure for viscosity correlations. From [35].....	30
Table 3.4	Regression results for Reddy and Zhang's viscosity equation. From [37]	31
Table 3.5	Fitted oxide PMV parameters; one standard error in parentheses. Units are cm ³ /mole and cm ³ /mole-K. From [43]	34
Table 3.6	Average Composition of Lewis and Hugo's slag samples. [65].....	51
Table 3.7	Relative mobilities of elements in soils and sediments exposed to weathering (From [67], [68]).....	53
Table 3.8	Regulatory Limits for EPA contaminants relevant to metallurgical slags	54
Table 3.9	Target composition of slag samples from [71].....	55
Table 3.10	TCLP results for slag samples from [71]	55
Table 4.1	Experimental Compositions (in weight percent). Bold entries signify TCLP tests, <i>italicized entries</i> signify successful viscosity tests, and red entries signify unsuccessful viscosity tests.	57
Table 5.1	Reagent Specifications.....	63
Table 5.2	Calibration Values for 94.6 ± 10 cP Standard Fluid	70
Table 5.3	Density Setup Room-Temperature Validation Data	71
Table 5.4	Regression Statistics for Sample 1.	73
Table 5.5	Viscosity data as a function of RPM.....	74
Table 6.1	Experimentally-Calculated Activation Energies.....	79
Table 6.2	Regression Coefficients for Equation 6.2.	81
Table 6.3	Recovery of Lead Particles Through Slag After Fifteen Minutes.....	84
Table 6.4	Magnetite Content from Satmagan Analysis.	88

Table 6.5	Phase Distribution (wt%) According to HSC at 1200 °C.	89
Table 6.6	Phase Distribution (wt%) According to HSC at 700 °C.	90
Table 6.7	Barium Leached from Temperature Outlier Tests.	105
Table A.1	Viscosity Test Data for Sample 1.....	116
Table A.2	Viscosity Test Data for Sample 2.....	117
Table A.3	Viscosity Test Data for Sample 5.....	118
Table A.4	Viscosity Test Data for Sample 8.....	119
Table A.5	Viscosity Test Data for Sample 12.....	120
Table A.6	Viscosity Test Data for Sample 13.....	121
Table B.1	Density Data for Tests 1, 2, and 3.....	122
Table B.2	Density Data for Tests 4, 5, and 6.....	123
Table C.1	TCLP Leach Data for Barium Oxide-Doped Samples.....	125
Table C.2	TCLP Leach Data for Lead Oxide-Doped Samples.....	126
Table C.3	TCLP Leach Data for Arsenic Oxide-Doped Samples.	127
Table C.4	TCLP Leach Data for Quality Control Samples.	128

ACKNOWLEDGMENTS

I would like to acknowledge the support of others, without whom this research would not have been completed and this thesis would not have been written:

- My parents Robert and Arlene Schriener, for their unconditional love and support
- My brothers Andy and Scott, for their technical discussions at the dinner table
- My sister Beth, for including me on her adventures

- My committee members Patrick Taylor, Corby Anderson, Emmanuel DeMoor, and Rod Eggert, for their knowledge, expertise, and guidance through the duration of this project
- My sponsors at Gopher Resource (especially Joe Grogan), for their direction, motivation, and financial support of this project, as well as conducting the TCLP analysis
- Scott Pawelka and Bruce Yoshioka, for providing technical support when I broke things
- My former and current colleagues in the Kroll Institute for Extractive Metallurgy, for acting as sounding boards for my (often bad) ideas; specifically
 - Husni Usman, Caelen Anderson, Mark Manganello, Hunter Sceats, Jordan Rutledge, Tom Boundy, Victoria Vaccarezza, and Philip Keller, for putting up with me as an office mate
 - Allie Anderson and Brett Carlson, for completing this long journey together

- The Mines Club Ultimate team and Denver area ultimate community, for distracting me when I needed it (and moreso for when I most certainly did not)
- My friends near and far, for listening to me, counseling me, and encouraging me

- Those whose names have not been listed, but whose numerous contributions were vital to the success of this project

DEDICATION

To my grandfather, Ronald Schriener, who listened to updates on the progress of this thesis but passed away before it was submitted. He would be proud to see it has now been completed.

CHAPTER ONE INTRODUCTION

Lead's affinity for yielding a pure product from secondary feeds at extremely high recoveries has created a unique situation. In the United States, all lead produced comes from secondary sources. Of that feed, the vast majority is lead-acid batteries. The lead recovered from batteries is often alloyed with other elements to improve the properties of the battery while in service. When the battery is recycled pyrometallurgically, these impurities are often separated from the metallic lead and end up in the oxide slag. The slag is a waste product, and as such, must adhere to stringent environmental regulations for disposal. If the waste qualifies as hazardous, it can still be disposed of, but doing so is much more expensive. A much more economically attractive option for a lead producer is to control the chemistry of their slag so that it will meet those regulatory limits.

The slag system and impurity elements under consideration for this study are sodium-iron-silicates containing barium, lead, and arsenic. Together the sodium, iron, silicon, and oxygen make up most of the slag's composition. Sodium is used as a slag component as a result of upstream desulfurization. Barium enters the system because it is an additive to the plastics and separators. Lead can enter the slag in two ways: chemically, as an oxide from upstream processing; or physically, as entrained metallic lead. Lead in the slag is a source of lost revenue for a smelter, so keeping the lead content of the slag to a minimum is of primary importance. Arsenic is introduced into the system with the lead, with which it is alloyed to improve hardness.

Slags are subject to the regulations of the Toxicity Characteristic Leach Procedure (TCLP). A sample of the material is crushed and leached in an acetic acid solution for 18 ± 2 hours. The leachate from this test is then analyzed, and the elements must have concentrations under the given limits: barium, 100 parts per million (ppm); arsenic, 5.0 ppm; and lead, 5.0 ppm. Solid waste can pass the test if the concentration in the solid is above these limits, but will fail if the concentration in the liquid extract exceeds them. Therefore, it is ideal to design slags which retain those elements in insoluble phases.

The primary goal of this work was to analyze a variety of sodium-iron-silicate slag systems containing barium, arsenic, and lead to determine which slags, when cooled either quickly or slowly, had lower impurity concentrations when subjected to the TCLP. Qualitative phase information was also gathered to predict into which phases the impurities would congregate. Additionally, the physical properties of those molten slags were investigated in order to understand how they changed as the composition was adjusted to produce a slag which would pass the TCLP.

CHAPTER TWO LEAD PROCESSING

Lead was hardly considered to be a noteworthy metal in ancient times due to its dull appearance, but sees wide use today. It was commonly mined as a byproduct of silver, which was valued for currency and decoration. Transmuting this undesirable metal into gold was an early goal of the study of alchemy. Classical times brought a rise in the appeal of lead as it was used in water distribution, roofing systems, and stained glass. With the Industrial Revolution in the 18th and 19th centuries, lead began to see widespread use in plumbing and as an additive in paints. Concrete evidence recognizing the health dangers of lead began to spread in the late 19th and 20th centuries, which caused bans in lead from paints, pipes, and gasoline – the last major product to contain potentially harmful lead. Modern lead is used primarily in automotive lead-acid batteries, where it can be almost perfectly recycled with the assistance of refining steps.

The most common primary source of lead is the mineral galena: PbS. Two other lead-bearing minerals are anglesite and cerussite: PbSO₄ and PbCO₃, respectively. Lead deposits are often associated with zinc, tin, bismuth, antimony, arsenic, silver, and gold. Traditional smelting of lead-bearing ores occurred in reverb (short for reverberatory) furnaces, but several methods have since been developed. Blast and rotary furnaces have come into use; in some cases, in conjunction with a reverb. Table 2.1 lists North American lead producers' furnace types and capacities (in short tons) as of 2015. Worldwide primary production of lead has recently been eclipsed by secondary production as a result of the ease of recycling spent lead-acid batteries. Lead production in the United States is sourced entirely from secondary feeds, almost all of which consists of lead-acid batteries. [1]

2.1 Traditional Lead Processing

There are two main furnace types which have been traditionally employed in lead smelting. They are the reverberatory furnace (or reverb) and the blast furnace.

2.1.1 Reverberatory Furnaces

Lead is easily reduced in the reverb. Antimony, arsenic, and tin are not. The latter three are selectively slagged in the reverb. The primary reactions to be considered are the conversion of lead sulfate, sulfide, carbonate, and oxide to lead sulfide, oxide, oxide, and metallic lead; respectively:



Table 2.1 North American Lead Smelting Operations and Capacities. From [1]

Country	Company	Location	Furnace Type	Primary	Secondary	Subtotal
Canada	Cominco	Trail, BC	Kivcet	90,000		
	Xstrata	Belledunne, NB	Blast	80,000		
Mexico	Penoles	Torreon	Blast	120,000		290,000
USA	BRC	Arecibo, PR	Rotary		18,000	
			(idled 5/14)			
	Doe Run	Boss, MO	Reverb/Blast		140,000	
	East Penn	Lyons, PA	Reverb/Blast		100,000	
	Exide	Forrest City, MO	Blast		35,000	
		Muncie, IN	Reverb/Blast		90,000	
		Vernon, CA	Reverb/Blast		95,000	
			(idled 5/14)			
	JCI	Florence, SC	Rotary		120,000	
	Gopher	Eagan, MN	Reverb/Blast		130,000	
		Tampa, FL	Reverb/Blast		110,000	
	RSR	City of Industry, CA	Reverb/Elec		120,000	
		Indianapolis, IN	Reverb/Elec		120,000	
		Middletown, NY	Reverb/Blast		120,000	
Sanders	Troy, AL	Blast		100,000	1,298,000	
Canada	Nova Pb	Montreal, QC	Long Rotary		80,000	
	Tonnolli	Toronto, Ontario	Rotary		45,000	125,000
Mexico	JCI	Cienega de Flores, NL	Rotary		125,000	
		Garcia, NL	Rotary		135,000	
	M3	Roynosa	Rotary		30,000	
	Omega	Planta Dr Gonzoles, NL	Rotary		25,000	
	Pipsa	Garcia, NL	Rotary		25,000	
	Riasa	St. Caterina, NL	Rotary		25,000	375,000
Total				290,000	1,798,000	2,088,000

Reducing all of the metal in the reverb will make a “sticky” slag, one with a viscosity too low to pour. In light of this, lead is retained in the slag as result of a conscious effort to avoid reducing the impurities and ruining the soft lead. A generalized composition of the reverb slag may be similar to that in Table 2.2:

Table 2.2 Composition of a Reverb Slag

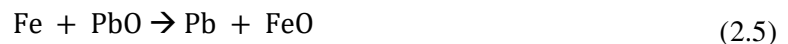
Constituent	Percent
Lead	58 to 72
Antimony	5 to 12
Tin	0.65 to 1.00
Arsenic	0.35 to 0.65
Sulfur	2.00 to 3.50
Silica	1.00 to 2.00

A historical smelter may have achieved a slag-to-lead ratio of approximately 1:3 when one includes the sulfur-based matte phase as slag, but desulfurization (and therefore, extremely limited matte production) can decrease that to 1:6 or less.

2.1.2 Blast Furnaces

An early objection to the use of reverb furnaces was the considerable metallurgical losses to smoke. Metallurgists from Germany recognized that baghouses attached to a blast furnace allow for retention of this value, and were the first to bring the blast furnace to the western US. [2] In operation, keeping the slag easy to handle without containing too much lead is the smelter’s biggest struggle.

A lead blast furnace is operated at a lower temperature and has a lower coke requirement than an iron blast furnace. The conditions are not strongly reducing, so iron oxide is kept in the slag. To generate a slag, scrap iron can be used as a reductant:



The slag will melt around 1200°C and the lead at 330°C. There can be up to four products from a primary lead blast. The crude lead bullion contains the lead and impurities such as antimony, tin, arsenic, copper, silver, and gold. The slag is traditionally an iron silicate with some lime and can also contain zinc oxide. A matte phase will be created when enough sulfur is present in the feed. Copper may also be associated with the matte. Antimony and arsenic in excess may react with iron to form a speiss, which

will contain cobalt and nickel. When the feed to a lead blast furnace is the slag from a reverb, the slag will contain soda in addition to lime, and speiss and matte phases will not be generated.

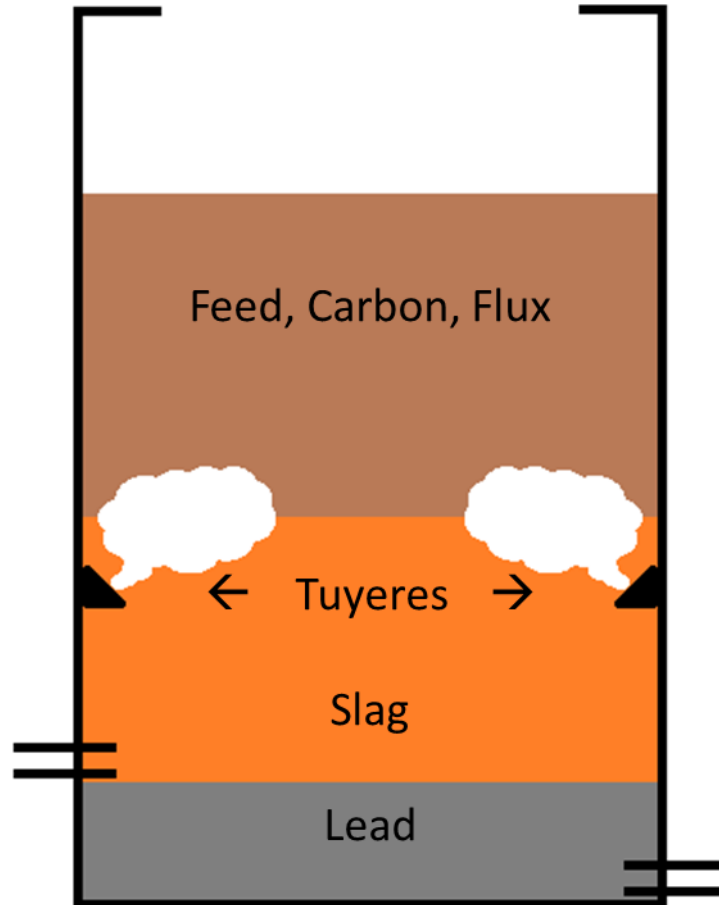


Figure 2.1 Schematic of a Lead Blast Furnace

2.1.3 Containing the Blast Furnace melt:

Used to contain and insulate the melt, refractories must meet several specifications. They should hold their strength up to a high melting point and be resistant to thermal shock. Chemically they must resist attack from the metal and slag, oxidation, and reduction. They should be stable to store. Finally, the cost must be considered when choosing a refractory.

Oxide refractories include silica, fireclay (alumina-silicates), alumina, chromite $[(Fe,Mg)(Cr,Al)_2O_4]$ and magnesia-chromite $(MgCr_2O_4 + MgO)$, magnesite (MgO) and dolomite $(CaO +$

MgO), forsterite (Mg_2SiO_4), more specialized oxides (ZrO_2 , ThO_2 , BeO). The melting points are highest of the pure oxides, which increase in the order: SiO_2 , Al_2O_3 , Cr_2O_3 , CaO , MgO . Carbon, graphite, silicon carbide, and other metals can be used as other refractory materials as well.

To match the acidity and basicity of slags, silica and fireclay are acid refractories whereas magnesite, burned dolomite, and forsterite are basic. Alumina and chromite are generally neutral slags. Where lead slags are created, which are corrosive to all known refractories, a water jacket is used. Cooling water is circulated around a steel shell, which cools a layer of slag on the inside wall of the steel. Once thermal equilibrium is reached and maintained, the solidified slag serves as the refractory.

Refractory bricks can serve several uses. When used as a furnace lining, refractory bricks are bound with a similarly-composed mortar (with the exception of sheet iron between magnesite bricks). Heating the iron oxidizes it and forms a monolithic structure with the bricks. When used for insulation, the bricks are more porous, weaker, and less resistant towards slags.

2.2 Primary Operations

Previous work by Oldwright and Miller was reviewed and critiqued by Ruddle. [3] The operating characteristics of three smelters (Tooele, UT; Kellogg, ID; and Trail, B.C., Canada) and two of their main difficulties were discussed: formation of lead accretions in the furnace and loss of lead to the slag.

The reactions in the furnace are as follows. At the top, the feed is reduced by a gas rich in CO . Sulfur may be distilled off, and PbO is reduced. As the furnace temperature increases the deeper into the furnace the feed travels, more constituents in the feed are reduced. While some sulfur creates the SO_2 , much of it combines with copper and iron to create a matte or with cobalt, nickel, and arsenic to create a speiss. With little matte- and speiss-forming content, the copper and arsenic (if not volatilized) report to the lead bullion. Iron is oxidized and combines with silica and lime to form the slag. Zinc is volatilized, captured in the bag house, and recirculated; or carried out in the slag. The ratio of slag to metal is on the order of three to one.

The operating objective of the three smelters differed. Tooele smelted several ores (24% Pb , 2-3% S , 13-15% coke), Kellogg smelted a lead-rich charge (50% Pb , 2-3% S , 10-11% coke), and Trail smelted a feed high in zinc (30% Pb , 10% Zn , 1% S , 10-11% coke). Representative charge compositions for the three smelters are given in Table 2.3 and material analyses are given in Table 2.4. Every sixth charge at Tooele was a special charge to clean accretions, containing 1,200 lbs lime-rock, 1,000 lbs blast-furnace skimmings, 1,000 lbs converter slag, 4,050 lbs sinter, 500 lbs miscellaneous ores, 250 lbs

siliceous ore, 275 lbs scrap iron and 1,100 lbs coke. At Trail the charge also usually contained small amounts of material from blast-furnace flues, antimonial slag, copper-dross bars, metallic lead from sintering machines, refining dross and silica.

Table 2.3 Representative Charge Compositions
Weight in charge (lbs.)

Material	Tooele	Kellogg	Trail
Sinter	6,075	2,500	2,550
Lime-rock	1,375	25	---
Siliceous ore	550	25	---
Scrap iron	275	---	---
Coke	1,100	300	300
Returned scrap	---	100	---
Refining dross	---	50	---
Zinc plant residue	---	50	100-350
Bag-house dust	---	100	---
Slag shells	---	---	200-400

Accretions formed on the shaft walls and in the crucible of the furnace. The latter may have required a total shut down, as they can prevent the connection between the lead well and the molten lead. It is theorized that they begin as difficult-to-fuse material mixed with pasty sulfides (such as zinc sulfide) several feet above the tuyères, and later material settled on top. The sulfides diffused inwards and a hard, slag-like surface developed on the outside. An alternative hypothesis for their formation (more fitting for Kellogg and Trail) was the vaporization and subsequent condensation of sulfides higher in the shaft. Fluctuations in furnace temperatures are also a likely contributor to shaft accretions.

Table 2.4 Typical Analyses of Materials Charged

Plant	Material	Date	Pb %	SiO ₃ %	Fe %	S %	CaO %	Zn %	Cu %	Sb %	As %
Tooele	Sinter	1929 1951	30.0	21.0	18.5	3.2	2.9	4.3	--	--	--
	Siliceous ore	1929 1951	36.0	45.0	5.0	3.0	1.0	1.0	--	--	--
	Converter slag	1929 1951	3.0	20.0	50.0	2.0	1.0	2.6	--	--	--
	Lime-rock	1929 1951	--	3.1	--	--	52.1	--	--	--	--
	Blast-furnace cleanings	1929 1951	3.9	25.0	23.0	3.0	10.4	4.8	--	--	--
	Sinter*	1930 1951	51.0 30	9.4† 9	12.7 19	2.4 1	6.8 7	5.0 9.5	0.6 --	0.3 --	0.08 --
	Bag-house dust	1930 1951	60.8	2.0†	0.2	7.2	0.6	7.2	0.07	1.2	0.24
	Zinc plant residue*	1930 1951	13.8	12.4†	19.9	8.3	--	9.5	0.5	0.1	0.02
Kellogg	Refining dross	1930 1951	60.2	--	--	--	--	15.8	0.06	5.0	--
	Returned slag	1930 1951	5.0	24.8†	27.1	2.7	10.4	8.0	0.6	--	--
	Siliceous ore	1930 1951	8.0	86.0†	3.0	1.1	--	0.1	0.5	--	--
	Sinter	1931 1951	34.0 35	10.5† 7.5	18.6 16	1.1 2	6.1 5.5	12.4 9.5	-- --	-- --	-- --

*Kellogg sinter (1930) contained 40.9 oz/ton of Ag and 0.15 oz/ton of Au; the zinc plant residue contained 22.6 oz/ton of Ag and 0.052 oz/ton of Au

†Quoted as content of insoluble material

Table 2.5 Typical Analyses of Smelter Products

Percentage

Smelter	Product	Date	Pb	Zn	SiO ₂	Fe	FeO	S	CaO	Mn	As	Cu	Others
Tooele	Dross	1929	67.6	0.3	0.6	2.2	--	1.6	1.0	0.3	2.2	10.50	
	Matte	1929	10.70	2.1	0.8	44.7	--	23.4	0.4	0.3	--	12.6	
	Slag	1929	0.89	5.5	35.35	--	32.0	1.2	20.2	1.1*	--	0.14	{4.3 Al ₂ O ₃ 3.5 MgO
		1951	1.6	15.6	23.0	--	28.5	1.2	15.8	0.75*	0.15	0.3	
	Flue dust	1929	34.7	1.9	--	7.28			Remainder consists of As ₂ O ₃ , carbon, some Cd, etc.				
Kellogg	Slag	1931	1.4	9.6	23.5	--	33.6	1.6	14.0	3.2*	--	--	{6.6 Al ₂ O ₃ 1.3 MgO
		1951	0.9-1.5	13.1	25.0	--	32.5	2.2	13.5	--	--	--	
	Flue dust	1931	60.8	7.2	--	0.2	--	7.2	0.6	--	--	0.07	{7.5 Sb 1.2 As 0.24 Cd
		1951	55.0	6.0	--	--	--	4.0	-	--	3.0	--	
Trail	Slag	1934	4.35	18.0	18.7	--	37.2	1.4	7.8	1.3*	0.05	0.19	{1.2 MgO 3.7 Al ₂ O ₃
		1951	2.8	17.1	20.5	--	35.0	2.8	9.2	--	--	--	
	Flue dust	1951	55.0	14.0	0.3	0.3	--	6.0	1.7	--	--	--	3-6 Cd

*Expressed as the percentage of oxide

The crucible accretions were layers of mainly zinc sulfide mixed with slag-forming constituents and some amounts of lead. Likely, the slag materials reached the lead bath and were submerged, where they fused in the cooler temperature region. This accelerated the formation of accretions by cooling the crucible (and limiting the amount of free smelting space for lead). General solutions to the formation of accretions were limiting sulfur content of the feed, adding zinc-sulfide fluxing agents, and widening the furnace.

Lead lost to the slag is considered in one of two forms: entrained metallic lead and oxide, sulfide, or silicate lead. The cause for lead silicate was found to be low CO near the tuyères, lower temperatures, and shorter dwell times. Kellogg's lead-rich charge has the consequence of bringing in difficult-to-reduce lead silicates and difficult-to-oxidize sulfur fused with lead in the sinter. Charging methods that resulted in fines at the outside, coarse material in the middle, and zinc residue resting on top of the coke and sinter were found to be optimal. Ruddle suggested experimental work in three directions of focus: determining the nature of lead in the slag (dissolved or entrained), examining the effect of the ferric content of the slag on the equilibrium between iron silicate and lead (and the effect of sulfur), and treatment with carbon (or other methods) in a holding furnace. These studies would assist in reducing the amount of lead lost to the slag.

Several notes were made on the behavior of the smelter's slags. Increasing the ratio of oxygen present in silica to oxygen in bases from 0.5 to 2.5 decreased the slags' formation temperature from 1200 to 1100 °C. Further addition of 10% lime reduced it to 1000°C. Lime rejects lead sulfide from the slag and reduces it to metallic lead. Barite was used in the place of lime because it gave a lower temperature and more-fluid slag. It also mitigated difficulties with magnesia and zinc oxide. Replacing lime with alumina raised the formation temperature, but replacing silica with alumina lowered it. Thus, replacing equal parts silica and lime with alumina has no effect. Magnesia raised the formation temperature and made the slag pasty, so it was recommended to be less than 5%. Iron and manganese raised the formation temperature, but reduced lead and other sulfides and prevented lead oxide from combining with silica. Zinc oxide was slagged by raising the iron content while lowering silica and lime additions and by quickly smelting at lower temperatures.

Metallic lead represented a large part of total lead (3.95%) when the slag was slowly cooled (1.27%) as opposed to granulated (0.60%). This could either be due to oxidation of lead during granulation or separation of metallic lead during slow cooling. While more detail is given on forms of constituents of the slag, the accuracy of their methods is disputable.

2.3 Modern Secondary Lead Processing

Lead-acid batteries contain several lead compounds in addition to plastic and silica-based casings and separators. Metallic and oxide lead (Pb, PbO, and PbO₂) make up the grids of the battery, which is immersed in a lead sulfate (PbSO₄) electrolyte paste. Polypropylene is used for the tops and cases of the batteries and glass fibers (silica) separate the grids.

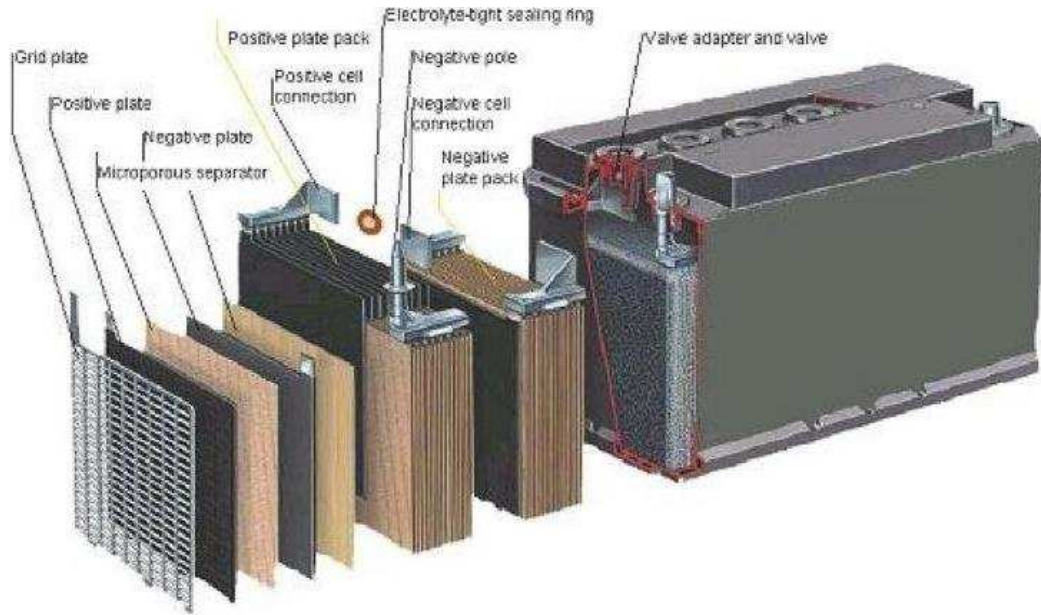
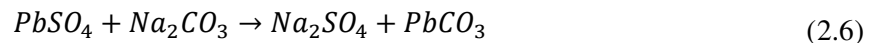


Figure 2.2 Cutaway of a Lead-Acid battery. From [4]

To begin the recycling process (illustrated in Figure 2.3), the batteries must be broken and their components physically separated. Sulfuric acid and plastic can be recovered and treated (extruded, in the case of the polypropylene) and sold as a byproduct.

Hydrometallurgical desulfurization is a modern pretreatment step before the reverberatory furnace. Battery paste can be stirred with soda ash to generate a solid material suitable for feeding into the furnace and a liquid sodium sulfate suitable for crystallization and sale as a byproduct. Because lime or dolomite would create harder-to-separate solid sulfates, they are not used. The reaction is given in Equation 2.6:



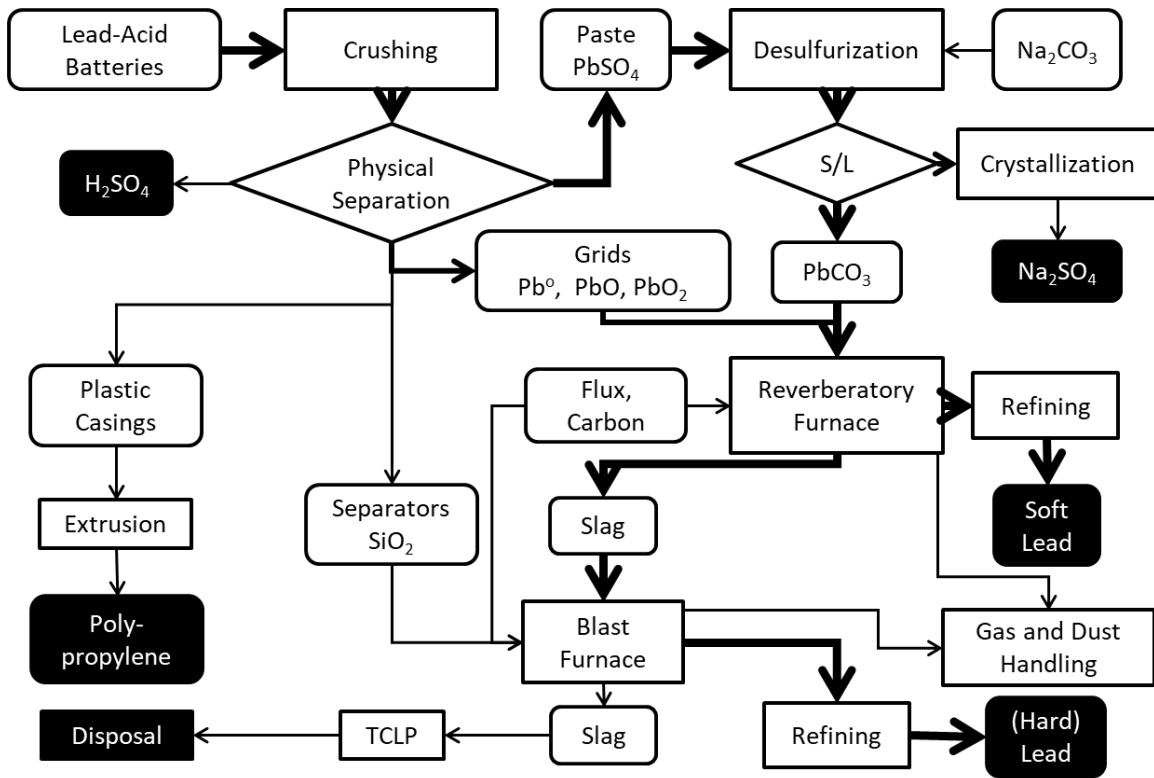


Figure 2.3 Lead-Acid Battery Recycling Flowsheet. From [5]

The desulfurized material, separators, coke and other reductants, and fluxes are then fed into the reverberatory furnace along with the other lead-bearing components. Separators (ethylene and silica) are fluxed in the blast furnace. Alternatively, East Penn converts the sulfur dioxide to ammonium bisulfite liquid fertilizer and purifies it by solvent extraction. Modern reverb feeds are dried in rotary dryers from 20% to <2% moisture, which increases furnace capacity by approximately a third.

CHAPTER THREE

SLAG FUNDAMENTALS

In general terms, a slag is simply a mixture of molten oxides. Extending this definition further quickly exposes a slag's complex technical nature and purpose. Slags appear in pyrometallurgical processes in order to protect a molten metal from reacting with the environment, to remove impurities from a melt, to chemically separate species from the feed, or to serve numerous other purposes. In many instances, a flux is added to a charge in order to generate a slag with certain chemical or physical properties. Some preferred attributes of a slag include: maximum ability to attract undesirable elements, minimum potential to attract valuable components, low liquidus temperature, optimal viscosity, and optimal density. The performance of slags and selection of fluxes can vary greatly due to changing composition of feed materials. A review of the purpose and properties of well-designed slags can be found elsewhere. [6] Slag properties highlighted in this work are structure, viscosity, density, and environmental behavior.

3.1 Liquid Slag Structure

Describing the structure of a slag has been an ongoing pursuit for the metallurgical field. One of the earliest models put forth to describe a liquid slag is that of Flood and Grjotheim. [7] They treated the slag as a mixture of cations and anions and used thermodynamic reaction equilibrium equations and rate constants to determine equations for the slag system. Such a treatment was criticized by Elliott *et al.*, but that criticism was refuted as merely being a limiting case of the original derivation. [8], [9] The Flood-Grjotheim Treatment has been extended to other slag systems, as well. [10] More recent studies have sought to describe the behavior of slags based on their similarities to polymers or the shapes and preferred orientations created by the molecular bonds. A review of slag fundamentals followed by a discussion of existing literature is presented in the following sections.

3.1.1 Theory and Fundamentals

One of the most common slag-forming compounds is silica (SiO_2), so an introduction to their structure will begin with assuming a network exists which is comprised of silicon cations (Si^{4+}) and oxygen anions (O^{2-}). Each silicon ion is surrounded by four oxygen ions which are covalently bonded between that silicon ion and one additional ion, such that the resulting structure is a three-dimensional network of silicon-oxygen-silicon chains. In a crystalline form, the oxygen ions spread out from one another at an angle of 109.5° . But when the silica is molten, that network does not show such long-range

order, and not every bond is at that angle. Figure 3.1 shows an illustration of these two structures as if they were taken through a plane of the three-dimensional structure.

When a different cation is added to the silica melt, the structure changes. As an example, lime (CaO) will be added to the silica, giving it calcium ions (Ca^{2+}) in addition to the silicon and oxygen. The nature of the calcium ion is to dissociate from its oxygen ion, which results in that oxygen ion terminating a chain of the previously-mentioned silicon-oxygen network. However, in order to maintain charge balance (electroneutrality), the calcium ion remains relatively close to the oxygen ion (Figure 3.2). As more and more calcium is added to the melt, the silica network begins to break into smaller pieces as its chains are terminated. These structures and representative formulas are given in Table 3.1.

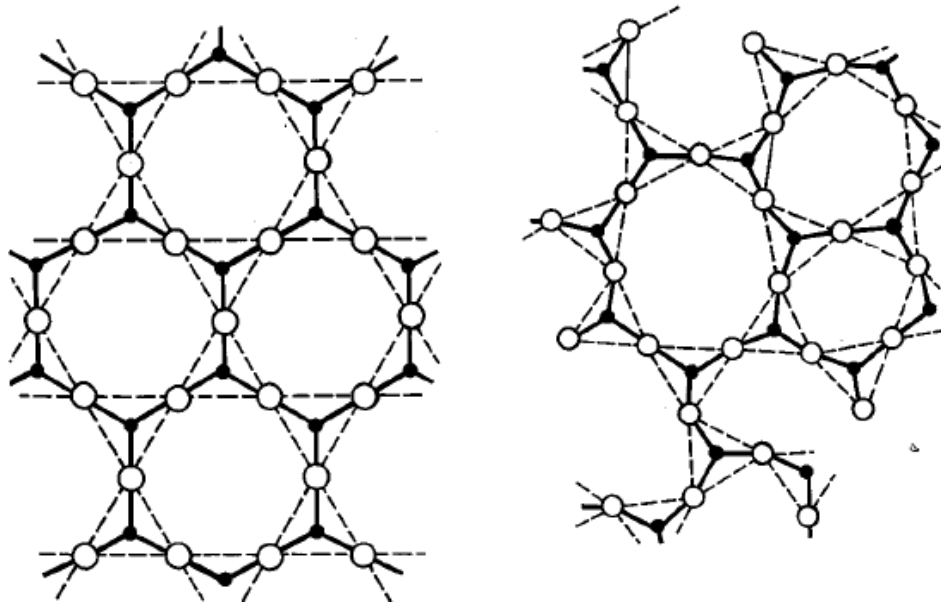


Figure 3.1 The structure of silica (crystalline, left; molten, right). From [11]

It can now be seen that there are two types of cations: those that contribute to the chains and those that break them. Generally, singly- and doubly-valent cations will break the chains while trivalent or more-positive cations will form them. An analogy can be drawn with aqueous chemistry in naming these two types: they are basic components (chain breakers) and acidic components (chain formers). Indeed, when dissolved in water, the pH of a basic slag will be high, and an acidic slag low. Some components, such as alumina, are amphoteric: they can either contribute to or break chains, depending on the overall composition of the slag.

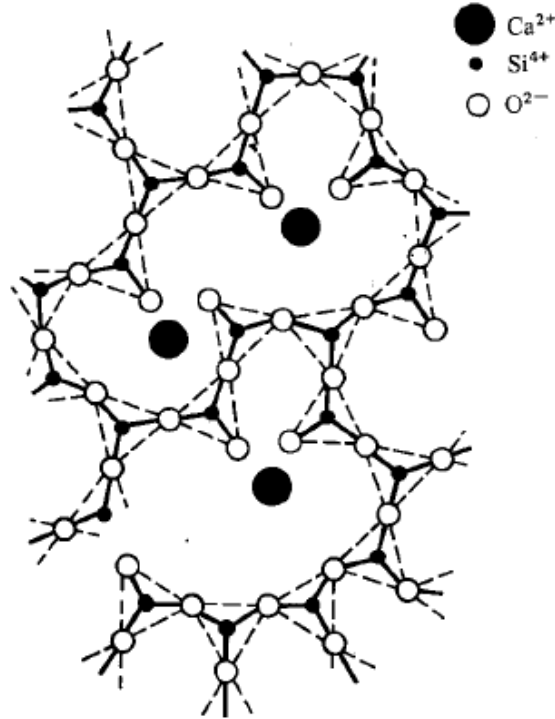


Figure 3.2 Illustration of a divalent metal oxide in molten silica. From [11]

Table 3.1 Structural Relationships in basic oxide-silicate melts. Adapted from [11]

Total Oxygen Atoms to Silicon Atoms	NBO/T	Corresponding binary molecular formula	Structure	Equivalent silicate ion
2:1	0	SiO ₂	All corners of tetrahedral shared	Infinite network
5:2	1	MO•2SiO ₂	One broken link per tetrahedron	(Si ₆ O ₁₅) ⁶⁻ or (Si ₈ O ₂₀) ⁸⁻
3:1	2	MO•SiO ₂	Two broken links per tetrahedron (ring)	(Si ₃ O ₉) ⁶⁻ or (Si ₄ O ₁₂) ⁸⁻
7:1	3	3MO•2SiO ₂	Three broken links per tetrahedron (chain)	(Si ₂ O ₇) ⁶⁻
4:1	4	2MO•SiO ₂ (orthosilicate)	All links broken	Discrete (SiO ₄) ⁴⁻ tetrahedra

If one could measure the oxygen ion activity in a liquid slag, they would have an absolute measure of basicity. However, since only the activity of the neutral oxides can be measured, a relative

measure of basicity must suffice. In industry, the ratio of basic oxides to acidic oxides is often computed as a proxy for basicity. Rosenquist suggests several of these empirical relations: [12]

$$\frac{CaO}{SiO_2}, \quad \frac{CaO - 4P_2O_5}{SiO_2}, \quad \text{or} \quad \frac{CaO + MgO}{SiO_2 + Al_2O_3}. \quad (3.1)$$

Slags with many broken chains, such as those of an orthosilicate composition, are said to be depolymerized. As it is in a pure silica melt, those with fewer, longer chains are referred to as polymerized. The degree of polymerization can be quantified theoretically by the NBO/T ratio for the slag, that is, the ratio of non-bonding oxygen atoms to tetrahedrally-coordinated cations:

$$\frac{NBO}{T} = \frac{2(O) - 4(T)}{T}. \quad (3.2)$$

Cation coordination structures depend on the relationship and relative strength of the cations' bond with oxygen. Basic oxides, which have a lower affinity for oxygen, tend to have an octahedral coordination, while acidic ones are tetrahedrally coordinated. Amphoteric oxides, such as Al^{3+} and Fe^{3+} , can be either octahedrally or tetrahedrally coordinated. [13]

3.1.2 Empirical Investigations of Molten Slag Structure

Raman and Mössbauer Spectroscopy are two common techniques used to study slag structures. When using Raman Spectroscopy, the vibrational modes exhibited by a sample are recorded. These vibrations are a product of specific chemical bonds present in the sample, and can thus be used to determine which atoms are bound together, or to how many different atoms a center atom is bound. Mössbauer Spectroscopy is used on iron-containing samples to determine the oxidation state of the iron ions. Mysen presented four main structural features in silicate melts: network-modifying cations, tetrahedrally-coordinated cations and their associated charge-balancing cations, ferric iron as a network former or modifier, and other cations. [14] In creating these groups, it is shown that the structure of melts can be described by just a small number of structural units.

Network-modifying cations consist of the alkali metals, alkaline earths, and ferrous iron. Their effect on the abundance of depolymerized structural units varies according to the ratio of their atomic number to the radius squared, Z/r^2 . SiO_2 and SiO_4^{4-} units correlate positively with Z/r^2 for all values of NBO/Si, while $Si_2O_5^{2-}$ units correlate negatively. The relationship for SiO_3^{2-} units varies according to the NBO/Si value – for low numbers it is a positive correlation, but at values greater than 1.2 it becomes increasingly negative. Low values of Z/r^2 contain a peak for low NBO/Si melts for $Si_2O_7^{6-}$ units, while melts with $NBO/Si > 2.4$ show an increase in abundance with Z/r^2 .

Given enough available large, electropositive cations to provide charge balance, aluminum exists in tetrahedral coordination. This behavior is shared with ferric iron. The stability of these charge-balanced complexes is positively correlated with Z/r^2 of the charge-balancing cations: $K^+ > Na^+ > Ca^{2+} > (Fe^{2+}) > Mg^{2+}$. The “other” common cations are Ti^{4+} and P^{5+} , which generally act as network formers. In more complex melts, the network-modifying effect of alkali and alkaline-earth cations can be limited by the necessity of charge-balancing tetrahedrally-coordinated aluminum and ferric ions.

Iron presents an interesting challenge because it is commonly found in two valence states (ferrous and ferric); but both are not always considered as separate components. Beyers suggested this is due to different backgrounds of investigation: steelmaking slags (which are generally at iron saturation) or magmatic liquids (which are fully oxidized). [13] Because there is such a small ferric component in steelmaking slags, its contribution is often neglected. Several authors have given evidence for multiple coordination structures for iron ions. Wang *et al.* analyzed the high-temperature structure of oxidized and reduced sodium-iron-silicate and showed that reduced samples are less-polymerized than their oxidized counterparts. [15] In that work, the ferric ions were shown to be tetrahedrally coordinated, while the ferrous ions were octahedrally and tetrahedrally coordinated. Kress and Carmichael showed that as the $Fe^{3+}/\Sigma Fe$ ratio decreases to less than 0.5, the coordination structure of ferric iron changes from tetrahedral to octahedral.[16] Dingwell and Virgo noted that this change is associated with a decrease in viscosity. [17] Because a change in oxidation state could result in a change of polymerization, it has been recommended that ferrous and ferric iron be treated as separate components in models.

3.2 Viscosity

As a liquid, one important property governing the behavior of a slag is its viscosity – its resistance to flow or shear deformation. Some liquids (such as water) have low viscosities, while others have much, much higher viscosities (such as pitch). There are also liquids that have viscosities that change according to the rate at which the shear stress is applied. The SI unit for viscosity is the Pascal-second: $Pa \cdot s = kg/(s \cdot m)$, although the cgs units of poise (P) and centipoise (cP) are also commonly used. The viscosity of water at room temperature is approximately one centipoise, which is equal to one millipascal-second: $1 cP = 1 mPa \cdot s$.

Viscosity can be found as the slope of shear stress τ versus shear strain rate $\dot{\gamma}$. The simplest relationship is that of Newtonian fluids, in which the viscosity is constant for all strain rates. A Bingham plastic will behave like a Newtonian fluid, but some initial shear stress τ_0 must be reached first.

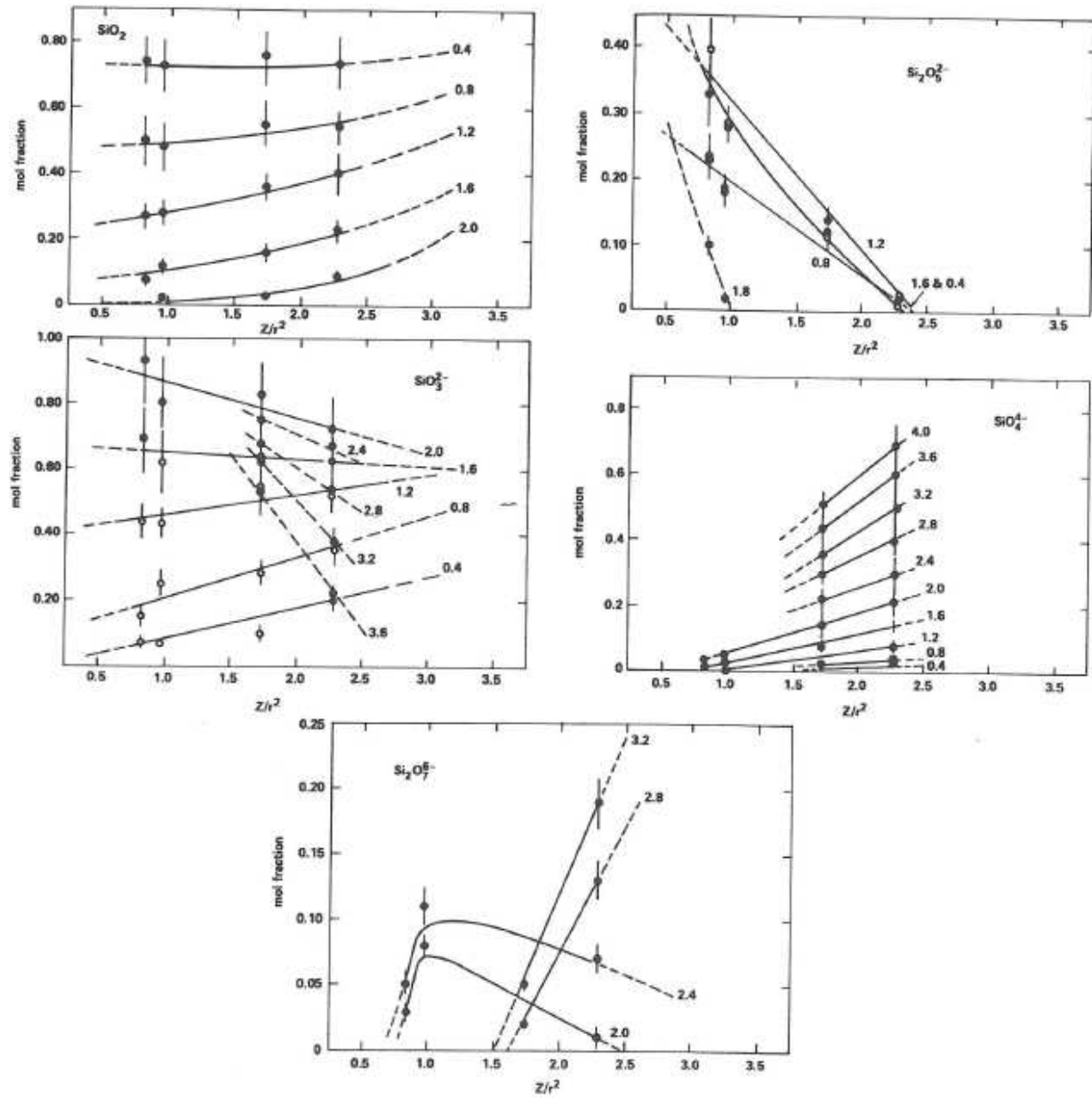


Figure 3.3 Abundance of anionic structural units in binary metal oxide-silica systems as a function of Z/r^2 of the metal cation for bulk melt NBO/Si-values as indicated in the figure. From [14]

Two other fluid types are pseudoplastic and dilatant fluids, which have viscosities that decrease and increase, respectively, with strain rate. The four fluid types are shown in Figure 3.4, which is an adaptation from Poirier and Geiger. [11] Viscosity can also be affected by time spent under agitation: thixotropic fluids will exhibit a decreasing viscosity with time, while rheopectic fluids will exhibit the

opposite. Generally, any fluid whose viscosity is not independent of shear rate or agitation is a Non-Newtonian fluid.

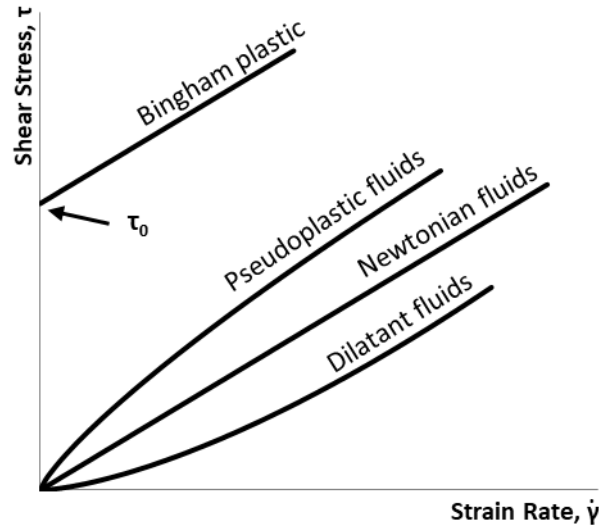


Figure 3.4 Shear Stress – Strain Rate relationships for various fluid types. Adapted from [11]

A fluid’s viscosity factors into all three fundamental transport phenomena. Newton’s Law describes a fluid’s kinematic viscosity, $\nu = \eta/\rho$, as its resistance to momentum transfer:

$$\tau_{yx} = \nu \times \frac{-d(\rho V_x)}{dy} \text{ or } \tau_{yx} = \eta \times \frac{-dV_x}{dy}. \quad (3.3)$$

When using the first formulation and the kinematic viscosity, the constant has units of length squared per time, which makes it analogous to α and D in Fourier’s and Fick’s Laws, respectively. The shear stress τ_{yx} which develops on a stationary plane is a function of the change in momentum ρV_x over the height of the film dy . In this case, the velocity (or momentum) gradient is that between the plane, where it is zero, and the surface of the flowing film, where it is at a maximum.

For a fluid flowing in a pipe, the Reynolds Number describes flow behavior as being laminar ($Re < 2,100$) or turbulent ($Re > 2,100$). Here, when the viscosity increases for a given average flow velocity \bar{V} and pipe diameter D , the Reynolds number will decrease, meaning that a more-viscous fluid will exhibit more-laminar flow, or that a more-viscous fluid will exhibit laminar flow at higher velocities than a less-viscous fluid.

$$Re = \frac{D\bar{V}\rho}{\eta} \quad (3.4)$$

The terminal velocity of a sphere falling through a stationary fluid can be determined by applying a force balance on that sphere. Equation 3.5 shows the result of combining the effects of buoyancy, weight, and drag (through Stokes' Law) on the falling sphere. [11] The fluid's viscosity appears in the denominator, which means that the terminal velocity would increase when the viscosity decreases; all other factors being constant.

$$V_t = \frac{2R^2(\rho_s - \rho)g}{9\eta} \quad (3.5)$$

Because blast furnace slags float on top of the liquid lead but lie below the feed, lead particles must travel through the slag before it is tapped or they risk becoming entrained. If they do not, the entrained particles represent a loss in production. If the slag viscosity is high, the terminal velocity of the particles will be lower, and it will take longer for the particles to settle through the slag. Thus, it is apparent that a lower viscosity is beneficial for maintaining a higher throughput.

A fluid's average heat transfer coefficient h is also a function of its viscosity. Empirically,

$$h = \frac{k \times \text{Nu}}{L} = \frac{k}{L} (0.664\text{Pr}^{0.343}\text{Re}^{0.5}), \quad (3.6)$$

where the Prandtl Number,

$$\text{Pr} = \frac{\nu}{\alpha} = \frac{\eta/\rho}{k/\rho C_p}, \quad (3.7)$$

defines the relationship between momentum and heat transfer. A higher viscosity will increase the Prandtl number, which will increase the momentum transfer boundary layer without affecting the thermal boundary layer. Because the Prandtl number (where viscosity is in the numerator) is raised to a power of 0.343 but the Reynolds number (where it is in the denominator) is raised to a power of 0.5, an increasing viscosity reduces the average heat transfer coefficient of the fluid. Because there will be a lower heat flux per temperature gradient with a more-viscous slag, it will insulate a melt better than a less-viscous one.

Viscosity inversely affects the diffusivity D of non-reacting spherical particles of radius R in liquids at temperature T according to the Stokes-Einstein equation:

$$D = \frac{\kappa_B T}{6\pi R\eta}. \quad (3.8)$$

Diffusion-controlled reactions which occur at the slag interface (either slag-metal or slag-refractory) will do so faster when the viscosity is lower. To maintain a higher refractory lifetime, it would be beneficial to have a higher viscosity (neglecting any effects of mechanical erosion). But, to increase the reaction rates at the slag-metal interface, a lower viscosity is desired.

Viscosity is known to change with temperature, although no one single equation governs the behavior for all fluids. Sridhar has presented a review of several common models. [18] An Arrhenius-type model is commonly used to model viscosity as a function of temperature. In that method, a pre-exponential term A and an activation energy E_a are employed. The activation energy describes the energy required to break the bonds between the silica units and allow them to move along one another. Viscosity measurement data is often used to empirically determine values for A and E_a for use with specific systems:

$$\eta = Ae^{E_a/RT}. \quad (3.9)$$

Iida developed a model for the viscosity of a mixture made up of components with mole fractions X_i based on their melting temperature $T_{m,i}$, molar volume $V_{m,i}$, and molar weight MW_i :

$$\eta_0 = \sum_{i=1}^n \eta_{0i} X_i \quad (3.10)$$

$$\eta_{0i} = 1.8 \times 10^7 \times \frac{(MW_i \times T_{m,i})^{1/2} e^{\frac{H_i}{RT}}}{V_{m,i}^{2/3} e^{\frac{H_i}{RT_{m,i}}}} \quad (3.11)$$

$$H_i = 5.1 \times T_{m,i}^{1.2} \quad (3.12)$$

Weymann took a statistical approach to modelling viscosity. [19] According to that method, a geometric criterion (that a hole must be present) as well as an energetic criterion (that a species has enough energy to move into the hole) had to be met. [20] Simplifying the terms from the original work, the equation becomes:

$$\eta = A_W T e^{E_W/RT}. \quad (3.13)$$

Riboud *et al.* created equations for A_W and E_W which are functions of slag compositions. [21] They relied on establishing five groups of similar-behaving components: “SiO₂” (which also contains P₂O₅, TiO₂, and ZrO₂), “CaO” (MgO, FeO, and BO_{1.5}), “Al₂O₃”, “CaF₂”, and “Na₂O” (K₂O).

Mills, Chapman, Fox, and Sridhar conducted a ‘round robin’ study to evaluate published viscosity models. [22] Their study collected viscosity measurement data on several types of slag materials and evaluated models’ performance at predicting slag viscosity. Iida’s model generally fit well when used for mold fluxes, coal slags, and blast furnace slags. Riboud *et al.*’s model, which fit mold flux viscosity data the best, did not perform well for CaO-Fe₂O₃-SiO₂ slags.

3.2.1 Theory and Fundamentals of Viscosity Measurement

To measure viscosity, a viscometer is used; the most common type of which consists of a cylindrical spindle connected through a spring to a motor. The derivation below follows those given by Mills and Van Wezer. [23], [24] When the surface of the spindle is used as the plane referenced by Newton's law, the shear stress on it is a function of the applied torque M and a characteristic shape factor f ,

$$\tau = f \times M, \quad (3.14)$$

where f is found using the radius R_s and effective length L of the spindle:

$$f = \frac{1}{2\pi LR_s^2}. \quad (3.15)$$

When using a viscometer, the applied torque M can be written as a function of the displayed percentage $\%T$ of the viscometer's maximum torque M_{max} ,

$$M = \%T \times M_{max}. \quad (3.16)$$

The shear rate $\dot{\gamma}$ is related to the speed in RPM using a proportionality factor C ,

$$\dot{\gamma} = C \times RPM, \quad (3.17)$$

which is determined using the radius of the spindle and crucible R_c .

$$C = \frac{\pi R_c^2}{15(R_c^2 - R_s^2)}. \quad (3.18)$$

By substituting equations 3.15 and 3.16 into 3.14, equation 3.18 into 3.17, equations for shear stress and shear rate are found:

$$\tau = \frac{\%T \times M_{max}}{2\pi R_s^2 \times L} \text{ and} \quad (3.19)$$

$$\dot{\gamma} = \frac{RPM \times \pi R_c^2}{15 \times (R_c^2 - R_s^2)}. \quad (3.20)$$

The viscosity can then be found two ways. It can either be found by determining the slope through a series of shear stress and shear rate pairs, or by dividing the shear stress by the shear rate at which it was recorded. The second method is expressed first in terms of physical constants in equation 3.21 and, after regrouping those constants into a Torque Constant TK and a Spindle Code SMC – as Brookfield does when using their viscometers – in equation 3.22. The physical constants that make up the SMC are shown in equation 3.23.

$$\eta = \frac{\%T \times M_{max}}{RPM} \times \frac{7.5}{\pi^2} \times \frac{(R_c^2 - R_s^2)}{R_c^2 R_s^2} \times \frac{1}{L} \text{ and} \quad (3.21)$$

$$\eta = \frac{\%T \times TK \times SMC \times 10,000}{RPM}. \quad (3.22)$$

$$SMC = \frac{f \times M_{max}}{C \times (TK \times 10,000)} \times 100 \quad (3.23)$$

Wright reviewed previous viscosity measurements at the international conference of molten slags, fluxes, and salts and discussed their benefits, shortcomings, and salient points. [25] While no single method can span the full range of viscosities (see Figure 3.5), the rotating cylinder technique is far and away the most-common technique for measuring high-temperature viscosity. Yet, these measurements are not undertaken without difficulty. Reactions between the container and measurement material can limit available setups, and many melts have viscosities that are still too low to be accurately measured by these systems.

As modeling becomes more and more widespread as an investigative approach, its uncertainty will continue to shrink as the reliability of databases continues to grow. These uncertainties are, at present, in the $\pm 20\%$ range, which is close to the same range given for many experimental results. Wu's 2012 study investigated the causes and results of various types of spindle, shaft, and crucible misalignment.

Ken Mills has been given much credit for his collaborative approach and efforts to standardize these types of measurements. He sought to identify best practices and a standard reference material (SRM) for determining slag viscosity. [23], [26] The previous SRMs for high temperature viscosity measurement (NBS 710, 711, and 717) have viscosities which are approximately an order of magnitude higher than most metallurgical slags. He determined that contact materials were an important factor that affected the results (graphite had a particularly pronounced effect). Other recommendations that he made included drying the sample overnight, using molybdenum components, using a neutral or reducing atmosphere, centering the melt in the isothermal region of the furnace and determining the temperature difference between the furnace thermocouple and the melt, using a maximum temperature of 1400 °C, calibrating thermocouples (against previously calibrated ones) and viscometers (with oils in the 0.1-1.0 Pas range and NBS 710 at high temperature), testing in repetitions of threes, and conducting post-mortem chemical analysis. Measurements using molybdenum components had the least scatter at ± 10 K.

Mackenzie investigated the viscosity of binary alkaline-earth silicates. [29] In melts up to 60 mol% metal oxide, the activation energies were calculated (using the Arrhenius form) and found to be slightly higher than those of the binary alkali silicates, as shown in Figure 3.7. Urbain and Gupta (separately) characterized the viscosity of the PbO-SiO₂ binary system and found the viscosity to decrease with increasing lead content. [30], [31]

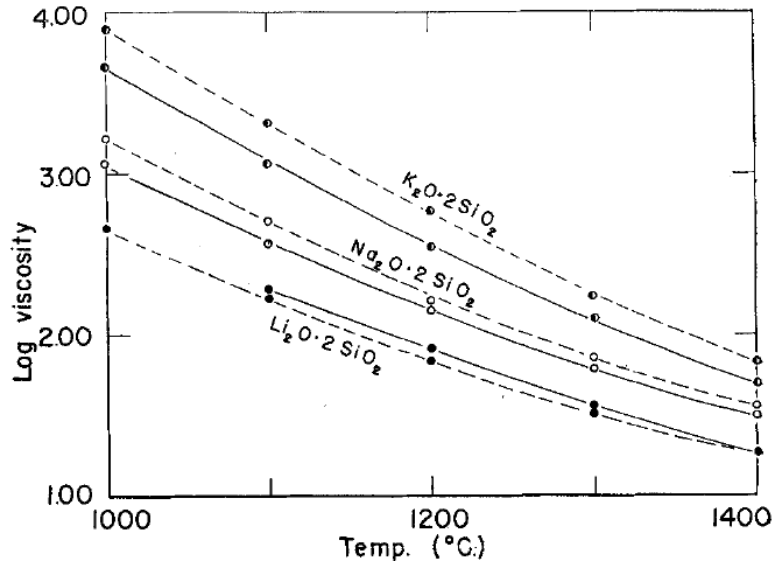


Figure 3.6 Viscosity of Alkali Silicates. From [28]

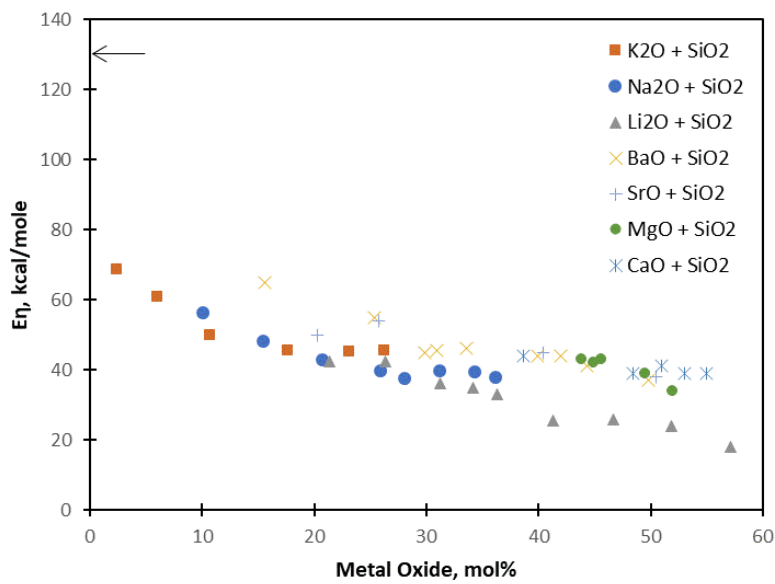


Figure 3.7 Activation Energy for Viscous Flow in Alkali and Alkaline-Earth Silicates. From [29].

Another realm containing similar molten oxide components is volcanology, where silicate melts representing magmatic systems closely resemble slag systems. While there has been little note made of sodium oxide as a component, either minor or major, in lead smelting slags it has seen attention in association with magma-like silicate liquids. Dingwell and Virgo analyzed viscosities of sodium-iron-silicate melts with varying compositions equilibrated under air in the temperature range of 800-1450°C. [32] Their melts were along the $\text{Na}_2\text{Si}_4\text{O}_9 - \text{Na}_6\text{Fe}_4\text{O}_9$ join containing 5, 10, 20, 30, 40, or 50 wt% of the latter; or along the $\text{SiO}_2 - \text{NaFeO}_2$ join containing 12.5 (SFN6), 25 (fe-albite), or 50% (acmite) of the latter (see Figure 3.8).

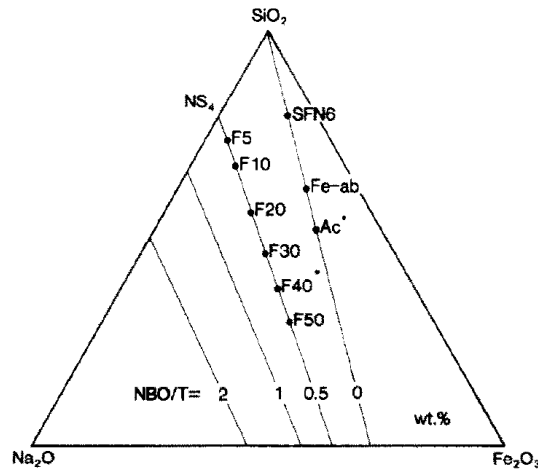


Figure 3.8 Graphic representation of experimental points used by Dingwell and Virgo. [32]

Their data showed that viscosity decreases with decreasing silicate content of the melt and, within error, obeyed an Arrhenius relationship. They used an equation similar to Equation 3.9 to model the viscosity-temperature relationship of their melts, with A in 3.9 being comparable to $-\log_{10} \eta_0$. The activation energies and pre-exponential constants from that model are given in Table 3.2. As the silicate content decreased, the activation energies and pre-exponentials decreased.

Additionally, they investigated the effect of the ferrous ion on viscosity. [17] Two melts from their previous study - acmite and NS4F40 – were chosen because they represent a fully polymerized (acmite) and de-polymerized (NS4F40) melt. To change the $\text{Fe}^{3+}/\Sigma\text{Fe}$ ratio, a CO/CO_2 atmosphere was controlled above the melt without changing the sample, temperature, spindle immersion depth; three items which can lead to considerable imprecision. The acmite melt at 1430°C showed a decrease in viscosity with decreasing $\text{Fe}^{3+}/\Sigma\text{Fe}$: 23 poises at the most oxidized to 9.5 at the most reduced (a factor of 2.4). The NS4F40 sample's viscosity decreased by a factor of 6.5 at 1200°C. This decrease in viscosity

was the result of depolymerization caused by reduction of ferric iron to ferrous iron and the accompanying change in coordination structure from tetrahedral to non-tetrahedral.

Table 3.2 Arrhenius constants for sodium-iron-silicate melts. From [32]

Sample	E_a (kcal/mole)	$-\log_{10} \eta_0$
NS4F5	40.8	3.41
NS4F10	39.8	3.53
NS4F20	36.3	3.58
NS4F30	35.9	3.98
NS4F40	35.2	4.27
NS4F50	33.7	4.39
SFN6	61.9	4.41
Fe-albite	52.7	4.61
Acmite	42.6	4.14

Sukenaga *et al.* also concluded that the viscosity of a $30\text{Na}_2\text{O} - 10\text{Fe}_2\text{O}_3 - 60\text{SiO}_2$ (mol%) melt decreased with decreasing $\text{Fe}^{3+}/\Sigma\text{Fe}$ ratio. Their data is shown in Figure 3.10. Again, the decrease in viscosity with decreasing ferric content was attributed to the change in coordination structure of the melts. [33]

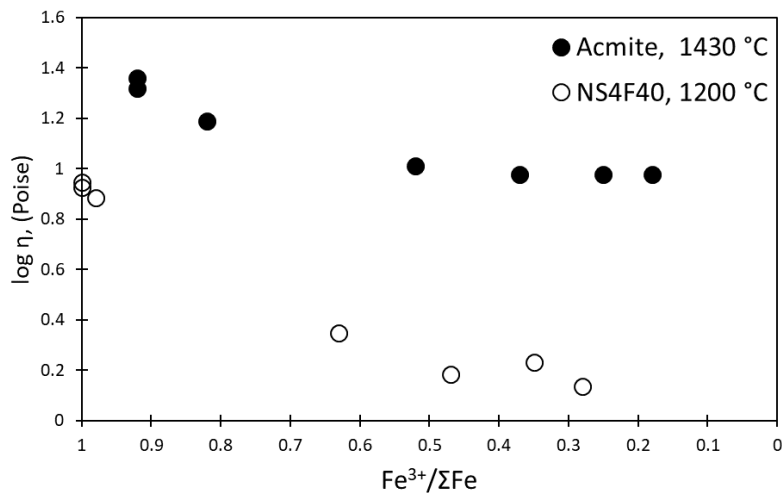


Figure 3.9 Viscosity as a function of ferric iron to total iron in Acmite and NS4F40 melts. Adapted From [17]

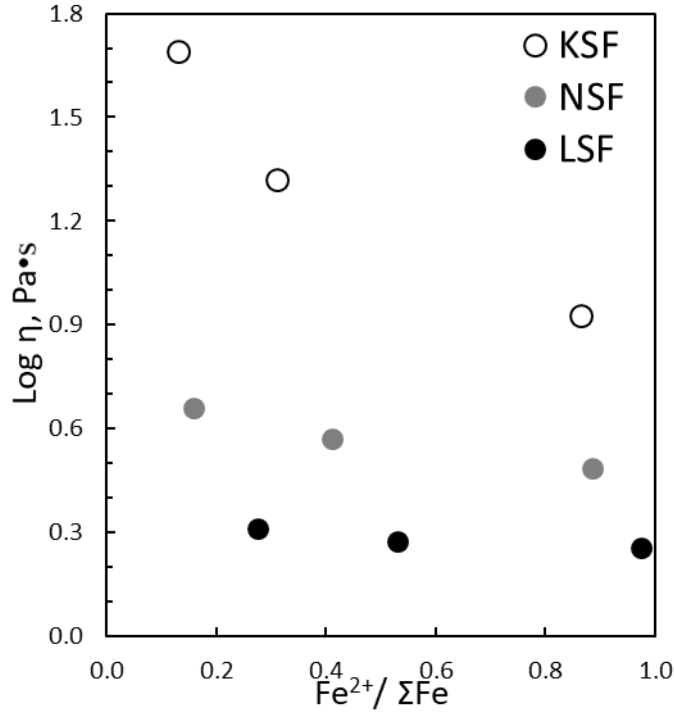


Figure 3.10 Viscosity as a function of ferrous to total iron. From [33]

Altman *et al.* conducted one of the earliest investigations on industrial lead smelting slags containing predominantly CaO, FeO, and SiO₂. [34] The other constituents were ZnO, MgO, Al₂O₃, Pb, and S, and temperatures for all tests ranged from 1126 to 1298 °C. They fit their data to an Arrhenius-type equation using a concentration ratio *CR* of SiO₂, Al₂O₃, and MgO to CaO, FeO, ZnO, and S.

$$\log \eta = 1.0600 \log(CR) + \frac{6801.2}{T} - 3.9881, \quad (3.24)$$

$$CR = \frac{SiO_2 + Al_2O_3 + MgO}{CaO + FeO + ZnO + S}. \quad (3.25)$$

Battle and Hager determined viscosities of a variety of lead smelting slags in calcium-iron-silicate systems from 1150-1350 °C. [35] Slag viscosities were found to be independent of spindle RPM (which validated the assumption that they were Newtonian fluids) and immersion depth beyond 2 cm. At shallower depths, the surface tension and end effects increased the error in the measurements. Results for several of their experiments can be seen in Figure 3.11. Viscosity was dependent on composition and temperature: it rose as the weight parameter (described below) or temperature decreased. The value of 5 poise was discussed, albeit briefly, as being “ideal” for lead smelting slags.

$$\text{Weight Parameter} = \frac{\text{CaO} + \text{MgO} + \text{ZnO} + \text{PbO} + \text{CuO} + \text{FeO} + \text{Fe}_2\text{O}_3 + \text{CaS}}{\text{SiO}_2 + \text{Al}_2\text{O}_3} \quad (3.26)$$

The rise in viscosity as the weight parameter decreased was attributed to the chain-forming behavior of silica and alumina. An increase in the temperature at which viscosity rose sharply was attributed to the basic oxide components, and corresponded to a rise in liquidus temperature. After comparing available data sets, they proposed the following general expression (equation 3.27) for viscosity at a given temperature. Coefficients (A_0 , A_1 , etc.) were then fit for several temperatures. It was noted that the correlations reported in this study (Table 3.3) are limited in applicability to systems within the examined composition ranges – a cautionary statement which can be made of any similar study.

$$\eta = A_0 + A_1 \times WP + A_2 \times WP^2 + \dots + A_N \times WP^N. \quad (3.27)$$

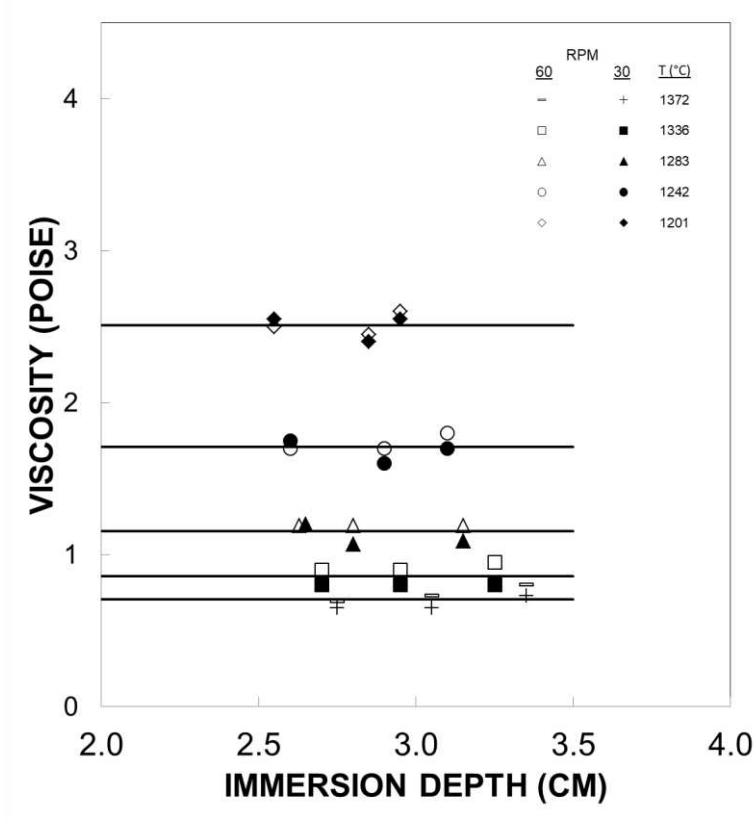


Figure 3.11 Viscosity as a function of temperature, immersion depth, and spindle RPM. Adapted from [35]

Table 3.3 Results of curve-fitting procedure for viscosity correlations. From [35]

Temperature, °C	WP _{cr}	η _{cr} (Poise)	A ₀	A ₁	A ₂	A ₃	A ₄	A ₅
1150	2.46	1.8	745.55	-1858.69	1864.35	-933.95	233.03	-23.13
1200	2.77	1.1	242.97	-516.54	447.28	-195.31	42.86	-3.77
1250	2.19	1.0	437.78	1253.29	1459.92	-856.70	252.03	-29.64
1300	2.21	0.7	614.65	-1783.74	2069.13	-1192.85	341.15	-38.70
1350*	2.42	0.4	70.53	-67.80	0	0	0	0
			116.13	-258.73	219.74	-82.68	11.53	0

*The first parameters are valid for $WP < 0.92$ and the second for $0.92 < WP < 2.42$

Reddy and Zhang studied calcium-iron-silicate industrial lead smelting slags over a similar temperature range. [36], [37] The authors commented that while previous correlations (such as Altman's or Battle's and Hager's) served as a good approximation, they failed to differentiate between individual basic or acidic components, as they generally took the sum of the former divided by that of the latter. Reddy and Zhang's contribution, therefore, was to bring these two components together into an equation that accounted for both composition and temperature:

$$\ln \eta = \left(A_0 + \sum A_i X_{A(i)} \right) + \left(B_0 + \sum B_i X_{B(i)} \right) \times \frac{10^3}{T}. \quad (3.28)$$

where $X_{A(i)}$ is the weight percentage of network-forming oxides, $X_{B(i)}$ is the weight percentage of metallic oxides or other non-network forming components in the slag, and the units for η and T are Pa·s and K, respectively. Combining data from several previous studies (Urbain, Gupta, Altman *et al.*, Battle and Hager) with their own, their regression produced the values in Table 3.4.

3.3 Density

A substance's density is the amount of mass contained in a unit volume. The SI unit for density is kilograms per cubic meter, kg/m³. At room temperature, water has a density of approximately 1,000 kg/m³ (1 g/cm³). A substance's density divided by the density of water is termed its specific gravity (s.g.). For comparison, Liquid lead has an s.g. of ten at its melting point, and slags have an s.g. between two and five. This difference makes for a relatively easy separation of the two phases. The inverse quantity (volume per mass) is a fluid's specific volume or, when dividing per mole, molar volume. When considering a mixture of components, the contribution from each component is termed its partial molar volume. Because multicomponent slags can contain more than one phase in the form of immiscible liquids or solid precipitates, an accurate calculation of density is not always straightforward.

Table 3.4 Regression results for Reddy and Zhang's viscosity equation. From [37]

Constant	Value	Input Data Range	
A_0	$-575715.3740 \times 10^{-5}$	Temperature	719°C to 1433°C
A_{SiO_2}	$-389437.4952 \times 10^{-6}$	SiO ₂	8.24 to 36.8 wt%
$A_{Al_2O_3}$	$-390404.5030 \times 10^{-6}$	Al ₂ O ₃	2.11 to 11.5 wt%
B_0	$786518.4490 \times 10^{-4}$	MgO	0.2 to 9.5 wt%
B_{MgO}	$-771212.5136 \times 10^{-6}$	CaO	3.3 to 21.7 wt%
B_{CaO}	$-800472.4918 \times 10^{-6}$	ZnO	0.54 to 24 wt%
B_{ZnO}	$-784229.3480 \times 10^{-6}$	FeO	9.37 to 34.7 wt%
B_{FeO}	$-791899.5395 \times 10^{-6}$	PbO	0.13 to 91.76 wt%
B_{PbO}	$-788793.4502 \times 10^{-6}$	CuO	0 to 23.18 wt%
B_{CuO}	$-610832.3709 \times 10^{-6}$	NiO	0 to 7.47 wt%
B_{NiO}	$-431765.0764 \times 10^{-6}$	S	0 to 6.8 wt%
B_S	$-902650.2835 \times 10^{-6}$	Viscosity	0.027 to 19.20 Pa.s
B_{Others}	$-688434.7979 \times 10^{-6}$		

3.3.1 Theory and Fundamentals of Density Measurement

Many empirical investigations of a fluid's density rely on its contribution to buoyancy – the upward force exerted on a body by a fluid – as a measuring principle. This approach is called Archimedes' Method. For any object, its weight W_o is equal to its mass m_o times gravitational acceleration g .

$$W_o = m_o \times g. \quad (3.29)$$

Archimedes stated that the buoyant force F_b on an object is equal to the weight of the fluid displaced by that object. In a separate finding, he determined that the displaced volume of fluid is equal to the immersed volume of the object (Eureka!).

$$F_b = m_f \times g = V_{displaced} \times \rho_f \times g. \quad (3.30)$$

Once the object is immersed in a fluid, the buoyant force acts against its weight to produce an apparent weight W_l . This is illustrated in Figure 3.12, where the object seen is the cross-section of a cylinder with radius r and immersed depth h . An error term ϵ is included in the equations to capture the effect of surface tension; assuming the object is not fully immersed or that it is connected to a wire extending out of the fluid.

$$W_1 = W_0 - F_b + \varepsilon = m_o \times g - (\rho_f \times \pi r^2 \times h_1) \times g + \varepsilon \quad (3.31)$$

If that immersion depth is changed, a second apparent weight W_2 is created:

$$W_2 = m_o \times g - (\rho_f \times \pi r^2 \times h_2) \times g + \varepsilon \quad (3.32)$$

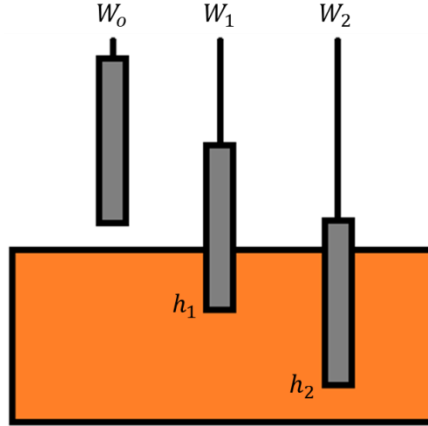


Figure 3.12 Illustration of an object's apparent weight as it is lowered into a fluid.

After the second apparent weight is subtracted from the first,

$$W_1 - W_2 = \rho_f \times \pi r^2 \times (h_1 - h_2) \times g, \quad (3.33)$$

the terms can be rearranged to yield the density of the fluid in which the object is immersed

$$\rho_f = \frac{(m_1 - m_2)}{\pi r^2 \times (h_2 - h_1)}. \quad (3.34)$$

By taking the difference of the two apparent weights in this manner (and not the weight and an apparent weight), the error from surface tension is cancelled out.

Early density studies used a platinum bob that was spherical in shape suspended by a thin platinum wire. [27], [28] The sphere was hung from a balance and immersed in a fluid. Weights were added to or removed from the opposite side of the balance, and the velocity of the ball was recorded. That equilibrium velocity of the ball was then used with a manipulation of Stokes' Law to yield its immersed mass. That mass was divided by the volume of the sphere (corrected for thermal expansion) to yield the density of the fluid. Measurements in this manner are only reliable up to viscosities of about 500,000 centipoises.

Bockris *et al.* used a similar balance apparatus, but used bobs that were cylinders with conical ends instead of spheres. In an effort to negate the effect of surface tension, the two cylinders had the same stem diameter, but different volumes. The density calculation was made by subtracting the two buoyancy results. [38] Later studies also used this two-bob technique, but measured the mass of the bob at a steady depth. [39], [40]

By studying the density of a variety of fluids and using a regression function on the data set, the partial molar volume (PMV) \bar{V} of the fluid's components can be determined. Once a reliable data set has been created through careful experimentation, the density of liquids within that set's composition range can be calculated as a function of the mole fraction X_i , molar weight MW_i , and PMV,

$$\rho_{liq} = \frac{\sum(X_i \times MW_i)}{\sum(X_i \times \bar{V}_i)}. \quad (3.35)$$

3.3.2 Empirical Investigations of Density

Shartsis and Spinner first characterized a variety of optical glasses produced by NIST in terms of their viscosity, density, and expansivity; the latter two of which had not been studied in much depth before. [27] Capps joined them for further work on binary alkali silicate mixtures. [28] Neither work presented an attempt to model the densities of the systems, but the latter showed that density decreased and thermal expansivity increased with increasing alkali content. Bockris, Tomlinson, and White also studied molten binary alkali silicates, including a pair of ternary compositions.

Bottinga and Weill collected and evaluated existing silicate partial molar volume data (including that of Bockris, *et al.*). [41] They fitted partial molar volumes as a function of silicate mole fraction, then compared their calculation to measured data; finding good agreement. They concluded that density of complex silicate systems could be calculated from their composition with an error comparable to that of experimental determination.

That data set and model has been expanded upon. First, Nelson and Carmichael experimentally validated it through experiments which included more complex melts as well as TiO₂-containing melts. [39] Their regression approach yielded slightly different results than Bottinga and Weill, which they attributed to the modeling techniques employed: their model was regressed from data containing larger number of ternary melts, instead of the previous technique of using two previously calculated partial molar volumes (from binary melts) to calculate the third in a ternary melt of known volume. Mo *et al.* again added to the data set by determining partial molar volume values of Fe₂O₃. [42] Ferric iron had been

neglected from previous models due to its appearance in only low concentrations. They fit the partial molar volumes to a linear function of temperature,

Lange and Carmichael critically reviewed the accuracy of the generally-accepted density data set, and determined that several studies' accuracy was inadequate. [43] They eliminated those studies' data to include only measurements which had been taken with the Archimedean double-bob technique. This allowed them to present a new, more accurate regression of partial molar volumes as a function of temperature; the parameters of which are in Table 3.5:

$$\bar{V}_i(T) = \bar{V}_{i,1773\text{ K}} + \frac{d\bar{V}_i}{dT}(T - 1773\text{ K}). \quad (3.36)$$

Dingwell *et al.* determined several densities within the Na₂O-FeO-Fe₂O₃-SiO₂ system and found their own values for the partial molar volume of ferric iron in silicate melts. [40] Their values suggested that the partial molar volume of ferric iron had a compositional dependence. However, upon review of analytical techniques used for sodium-iron-silicate melts, Lange and Carmichael highlighted that Mössbauer spectroscopy overestimates the Fe³⁺ component in high-iron (>14%) silicate systems. [44] They pointed out that while the density measurements of Dingwell *et al.* are consistent with their own previous investigation, the discrepancy in their calculated volumes could be attributed to the bias from this compositional error.

**Table 3.5 Fitted oxide PMV parameters; one standard error in parentheses.
Units are cm³/mole and cm³/mole-K. From [43]**

	$V_{i,1573\text{ K}}$	$V_{i,1673\text{ K}}$	$V_{i,1773\text{ K}}$	$V_{i,1873\text{ K}}$	$dV_i/dT \times 10^3$
SiO₂	26.92 (0.07)	26.90 (0.06)	26.91 (0.06)	26.90 (0.06)	0.00 (0.50)
TiO₂	22.43 (0.32)	23.16 (0.26)	23.89 (0.25)	24.60 (0.27)	7.24 (0.46)
Al₂O₃	36.80 (0.21)	37.11 (0.18)	37.37 (0.17)	37.63 (0.18)	2.62 (0.17)
Fe₂O₃	41.44 (0.31)	42.13 (0.28)	42.97 (0.29)	43.94 (0.36)	9.09 (3.49)
FeO	13.35 (0.18)	13.65 (0.15)	13.97 (0.14)	14.23 (0.16)	2.92 (0.16)
MgO	11.24 (0.15)	11.45 (0.13)	11.73 (0.12)	11.98 (0.13)	2.62 (0.61)
CaO	16.27 (0.11)	16.57 (0.09)	16.85 (0.09)	17.15 (0.10)	2.92 (0.58)
Na₂O	28.02 (0.12)	28.78 (0.10)	29.51 (0.10)	30.26 (0.10)	7.41 (0.58)
K₂O	44.61 (0.20)	45.84 (0.17)	47.01 (0.16)	48.22 (0.17)	11.91 (0.89)
Li₂O	16.19 (0.18)	16.85 (0.15)	17.36 (0.14)	17.90 (0.15)	5.25 (0.81)
Na₂O-TiO₂	20.33 (2.71)	20.28 (2.25)	20.21 (2.14)	19.99 (2.32)	

3.4 Solid Slag Structure

Jak and Hayes compiled common experimental methods for phase determination, the object of such studies, and examples of the method in use. [45] In doing so, they highlighted that these experiments should only be performed after extremely careful consideration of the properties of the system, the reactivity of the system with potential containment and measurement methods, and the limitations of the proposed experimental techniques. Otherwise, they cautioned, the data from these experiments may lead to incorrect conclusions. They stated that electron probe X-ray microprobe analysis (EPMA) is the preferred technique for phase identification and measurement, with X-Ray Diffraction (XRD) as a complimentary method. Although Energy-Dispersive Spectrometry (EDS) can provide rapid, semi-quantitative phase information, they regarded it as unsuitable for accurate phase diagram determination. Instead, Wavelength-Dispersive detectors were recommended for accurate chemical analysis of those phases.

With increases in experimental understanding has come an expansion in the power of thermodynamic modeling. Modeling advances make it possible to accurately and reliably investigate ever more complex systems that have been difficult (or impossible) to do so previously. Software packages for analysis of multiphase equilibrium systems with databases include Thermo-Calc, FACT, ChemSage, MTDATA, and GEMINI2. [46] Data assessment has been performed and solution models have been developed by SGTE (Scientific Group Thermodata Europe). FACTSage and ChemApp present a user-friendly experience for exploring thermodynamic databases, while Thermo-Calc and DICTRA combine thermodynamic databases with kinetic models.

3.4.1 Phase Separation

The foremost relationship describing phases at equilibrium is the Gibbs Phase Rule, which states that the maximum number of phases P plus the number of degrees of freedom F is equal to the number of non-reacting components in the system C plus two.

$$P + F = C + 2. \tag{3.37}$$

The *phases* in a system are the distinct “parts” (solids, liquids, and gases) of the system which can be physically separated. The *degrees of freedom* refer to the conditions of equilibrium (temperature, pressure, and composition). A system’s *components* are the substances used to create the phases (elements). By definition, phases at equilibrium with one another must have the same temperature, pressure, and chemical potential of their components.

If it is assumed that each phase contains every component, $C-1$ equations are needed to specify a phase's composition (any more than that become redundant). Adding to the composition the system's temperature and pressure means that $P(C+1)$ variables are required to specify equilibrium. These variables fit into $P-1$ equalities (again, more would be redundant), which when summed yield $(P-1)(C+2)$ equations. Collecting the numerical difference between the number of variables and the number of equations as the degrees of freedom and rearranging the terms yields Equation 3.37 above. This derivation was a simplification of that given in Denbigh's *Chemical Equilibrium*. [47]

When two- and three- component systems are under consideration, their phase distributions can be displayed graphically using *phase diagrams*. In either case, pressure is customarily set at one atmosphere. Two-component systems lead to two-dimensional binary diagrams, which display composition versus temperature. While three-component systems can be created using three-dimensional diagrams (as two dimensions are required to establish composition, leaving temperature to a third axis), it is simpler to extract information from them when they are plotted at a fixed temperature as diagrams of composition. An excellent reference for constructing and reading these plots is Rhines' *Phase Diagrams in Metallurgy*. [48] Presentation of quaternary, quinary, and higher systems can be done in two or three dimensions by simplifying the system into pseudo-ternary systems or by overlaying temperature information on plots in compositional space.

Phase development in slags is dependent on the rate at which they are cooled. When they are cooled slowly enough for equilibrium reactions to proceed to completion, slags will form several solid phases due to differences in their components' crystal structures, atomic sizes, valences, and electronegativities. [49] When they are rapidly cooled, slags can retain nonequilibrium, metastable phases. These phases are not the most stable according to thermodynamics, yet unfavorable kinetics prevents them from transforming.

The nucleation rate of a phase transformation can be broken down into three components: the frequency of the solid atoms' vibrations, the rate at which a liquid atom will cross an interface to join the solid, and the rate at which a stable nucleus is formed. [50] The first component, the frequency of the solid atoms' vibrations, provides a rate (opportunities per second) for there to be an available site for an incoming atom. This is a result of the thermal energy of the solid. The rate of an atomic crossing – the second component – comes from the existence of an activation energy barrier between the solid and liquid phases. The third term, referring to a “stable” nucleus, comes from the free energy change produced when a solid of one phase appears in another. A competition exists between contributions of the (negative) volumetric free energy term and the (positive) surface energy term, which is illustrated in Figure 3.13. If

the solid phase is assumed to be spherical, there exist small radii at which the total free energy change increases when more atoms join the sphere. This is thermodynamically less favorable, so the sphere tends to shrink. If enough atoms form a sphere with a radius larger than that critical value (marked by the arrow in the figure), the sphere will continue to grow.

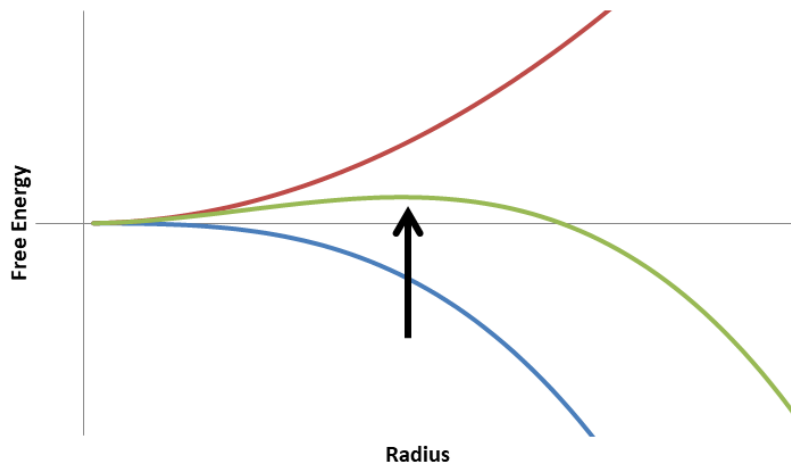


Figure 3.13 Illustration of Free Energy Changes Associated with Growth of a Spherical Particle. From top to bottom, the lines represent the surface energy contribution, the total free energy, and the volumetric energy contribution.

The latter two components are plotted for a generic system in Figure 3.14. The rate of an atomic jump decreases with decreasing temperature, because it becomes less likely that the atoms will have the energy required to cross the interface. Higher temperatures will result in jumps at higher frequencies and jumps to higher energy levels. The rate of stable nucleus formation decreases with increasing temperature because it is a function of the degree of undercooling (the difference between freezing temperature and the actual temperature of the melt). This is because the critical radius and energy required decrease with temperature. The overall rate of nucleation is the sum of these components, and has a maximum that lies somewhere in between these low- and high-temperature extremes.

If Figure 3.14 is rotated, Figure 3.15 can be created, which is a generalization of a Time-Temperature-Transformation (TTT) diagram. It can be used to predict which phases would be formed under different cooling rates. If the temperature is brought down slowly, many nuclei will form; but if it is done extremely quickly, none will form, and the result will be a glass. This is because although it may be thermodynamically more favorable for crystallization to occur, kinetically it cannot. While considering diffusion, it is also noteworthy that composition can have an effect on crystallization. Acidic slags are less

prone to crystallization than their basic counterparts because it is easier for the shorter silica polymer chains to rearrange.

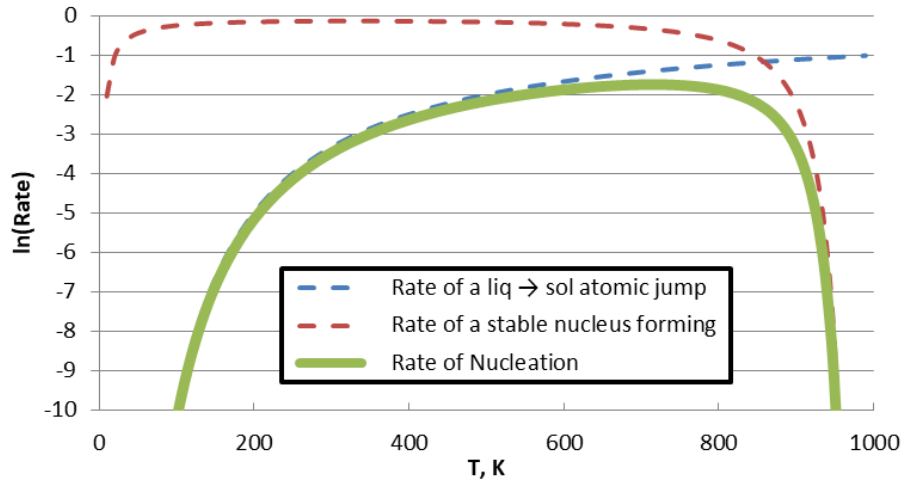


Figure 3.14 Rate Components' Contributions to Nucleation. From [50]

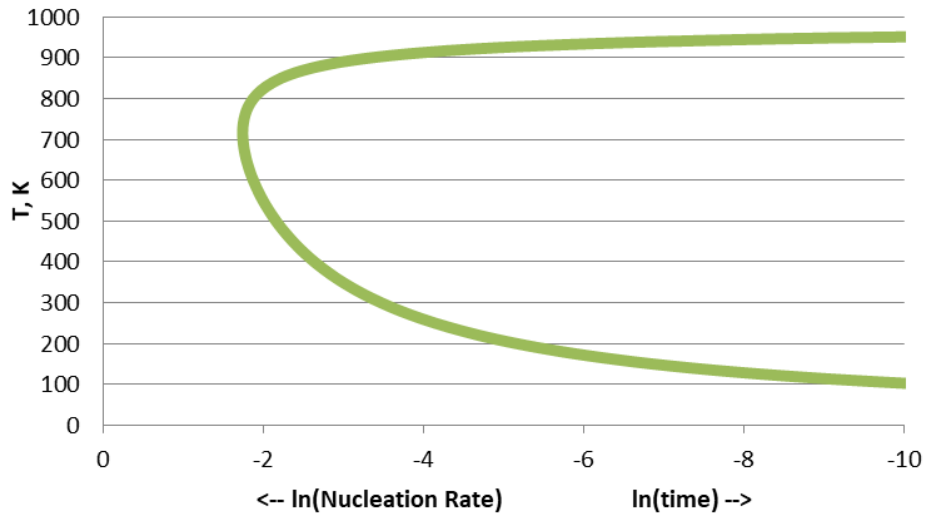


Figure 3.15 Generalized TTT-Diagram for a phase transformation. From [50]

3.4.2 Phase Diagrams of Relevant Oxide Systems

Many of the oxides used in this study (Na_2O , FeO , SiO_2 , BaO , PbO , As_2O_3) form binary and ternary compounds with at least one of the other oxides involved. Binary and ternary phase diagrams for

those systems – whether thermodynamic optimizations, results of experimental investigations, or both – are presented in this section. Since there are three compounds in the base system and three impurity oxides, there should exist twelve binary systems and ten ternary systems.

3.4.2.1 Na₂O-FeO

Four compounds were calculated to form between FeO and Na₂O: NaFe₂O₃ (at 17 mole percent Na₂O), NaFeO₂ (25 mol%), Na₃FeO₃ (50 mol%), and Na₄FeO₃ (66 mol%). [51] They can be seen in Figure 3.16. The lowest eutectic reaction is at 898 K and 75 mol% Na₂O, at which the liquid solidifies into Na₄FeO₃ and α-Na₂O. Some high-temperature solubility of Na₂O in the wüstite solid solution exists, up to a maximum of around 15 mol% at 1230 K.

3.4.2.2 Na₂O-SiO₂

By calculation of thermodynamic data and comparison to previous data, the Na₂O-SiO₂ phase diagram (Figure 3.17) has been obtained. [52] It contains two low eutectic regions; one at 19 mol% SiO₂ and one at 76 mol% SiO₂. A variety of sodium silicate intermetallics form with no solubility: Na₄SiO₄, Na₆Si₂O₇, Na₂SiO₃, Na₂Si₂O₅, and Na₆Si₈O₁₉.

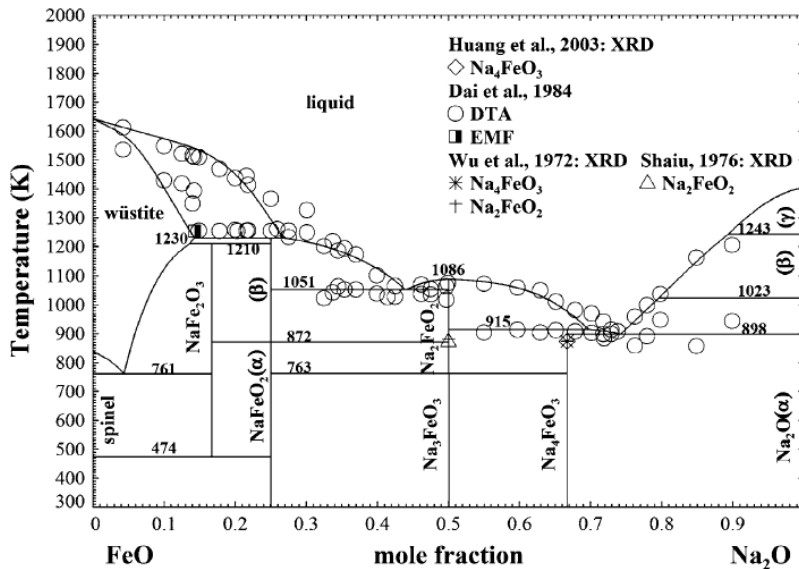


Figure 3.16 Calculated optimized FeO-Na₂O phase diagram. From [51].

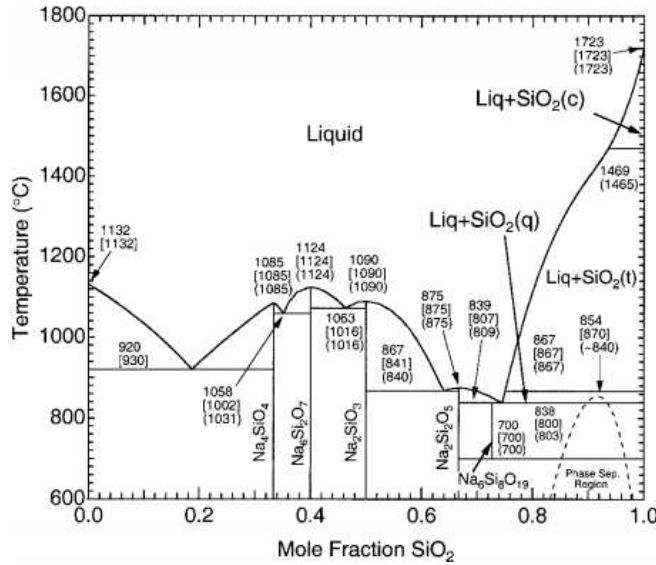


Figure 3.17 Calculated $\text{Na}_2\text{O-SiO}_2$ phase diagram showing presently calculated and previously reported (in parentheses and brackets) temperatures. From [52].

3.4.2.3 FeO-SiO_2

The FeO-SiO_2 system has been studied extensively as it forms the backbone of a variety of industrial slag systems. Below in Figure 3.18, the system has been thermodynamically calculated. [53] The only stable compound formed by these two oxides is Fe_2SiO_4 . Often referred to by its mineral name – fayalite – it is the iron-rich endmember of the olivine solid solution, with forsterite (Mg_2SiO_4) being the magnesium-rich endmember. The two eutectic reactions occur at 1173 °C and 1189 °C, forming FeO and fayalite at 24.5 mol% SiO_2 and fayalite and SiO_2 at 41.0 mol% SiO_2 .

3.4.2.4 BaO-SiO_2

One of the rare systems containing a higher-melting oxide than silica, the BaO-SiO_2 diagram has been calculated and is given in Figure 3.19. [54] At 72.6 mol% SiO_2 it reaches its lowest eutectic, forming BaSi_2O_5 and tridymite. The system contains several other intermetallics, with those containing more barium having progressively higher melting points, but no solubility.

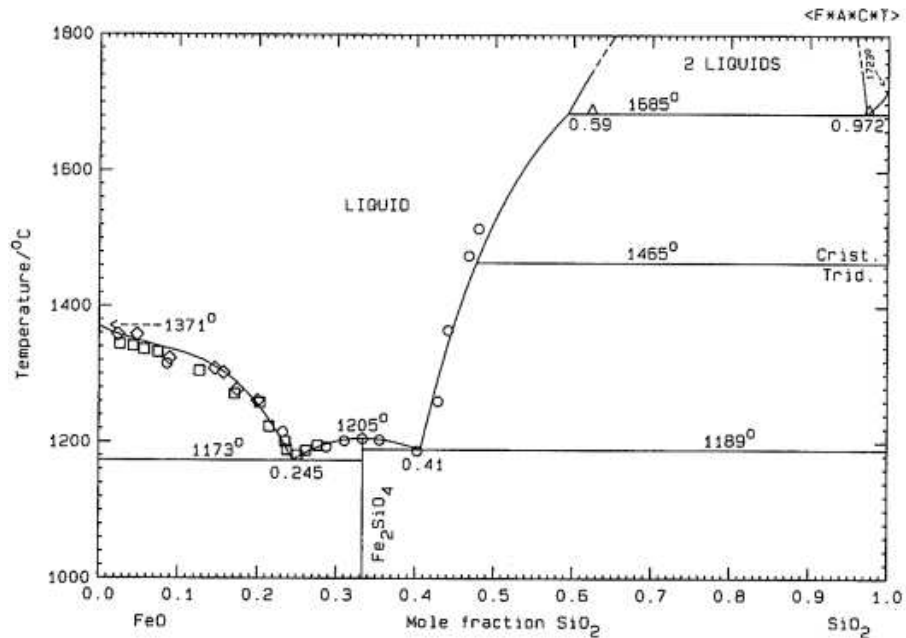


Figure 3.18 Calculated FeO-SiO₂ phase diagram. From [53].

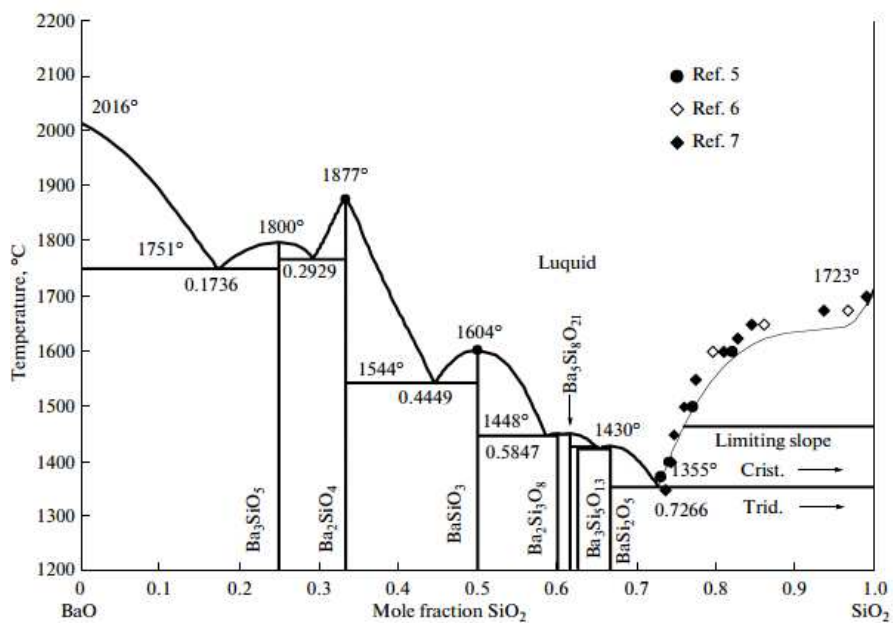


Figure 3.19 Calculated BaO-SiO₂ phase diagram. From [54].

3.4.2.5 PbO-SiO₂

Figure 3.20 displays the PbO-SiO₂ diagram, from the ACerS-NIST Phase Diagram Database. [55] Three intermetallic compounds form with no solubility: Pb₄SiO₆, Pb₂SiO₄, and PbSiO₃. The eutectic reactions between any of these and the pure compounds occur between 714 °C and 732 °C.

3.4.2.6 As₂O₃-SiO₂

The As₂O₃-SiO₂ diagram, shown in Figure 3.21, contains no intermetallics and no solubility of the phases, although the tridymite-to-quartz transition is still seen. [55] There is a region of liquid immiscibility from 1000 °C to 1187 °C, between 30 and 80 mol% As₂O₃. The liquidus comes down to 309 °C at almost 99 mol% As₂O₃.

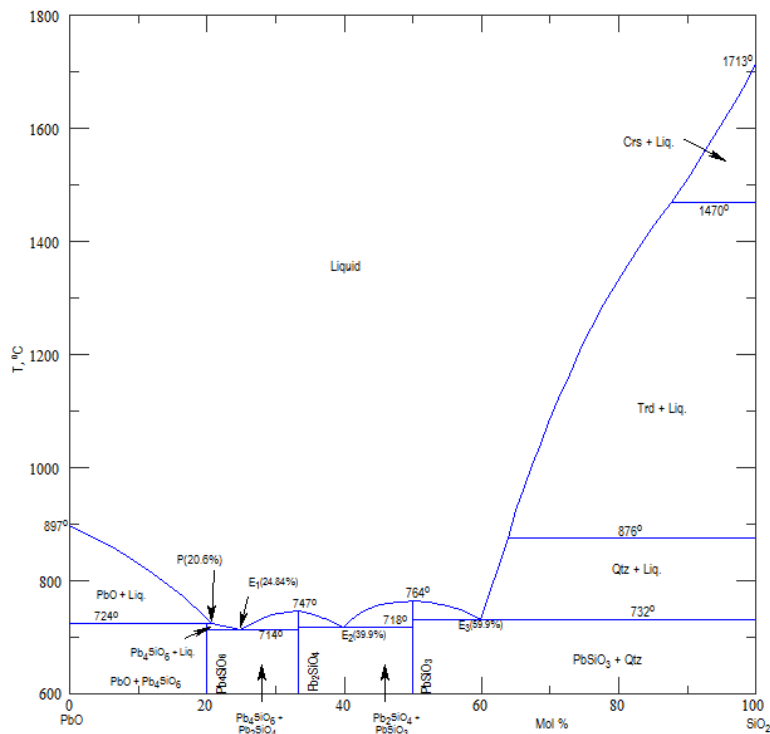


Figure 3.20 The PbO-SiO₂ phase diagram. From [55].

3.4.2.7 Na₂O-FeO-SiO₂

The work of Carter and Ibrahim was one of the first to determine phases in the Na₂O-FeO-SiO₂ system. [56] Their experimental procedure involved melting slags samples from reagent powders, cooling

and crushing them, and remelting under nitrogen. In some cases, days-long heat treatment was used in order to encourage formation of equilibrium phases. Using a combination of optical and x-ray techniques, they characterized several regions of the ternary diagram (Figure 3.22) and established the existence of one ternary compound – $\text{Na}_2\text{O}\text{-FeO}\text{-SiO}_2$.

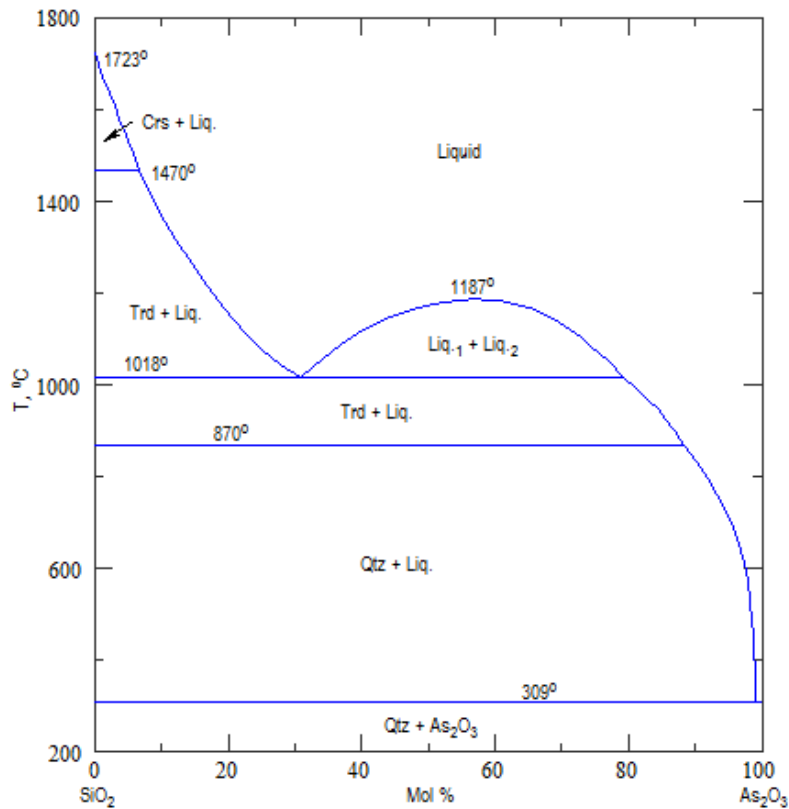


Figure 3.21 The $\text{As}_2\text{O}_3\text{-SiO}_2$ phase diagram. From [55]

They found that addition of soda (richer in soda than $\text{Na}_2\text{O}\text{-}2\text{SiO}_2$) to fayalite formed sodium silicates and wüstite at the expense of fayalite. They proposed that this was caused by the larger, less-positively-charged character of the sodium ions compared to the iron ions, which allowed them to more easily fit in the interstices of the silica network.

Schairer, Yoder, and Keene investigated the $\text{Na}_2\text{O}\text{-FeO}\text{-SiO}_2$ system, but little information about their experimental program was found. Their work is summarized by the $\text{Na}_2\text{O}\text{-FeO}\text{-SiO}_2$ entry in the Slag Atlas, reproduced in Figure 3.23.

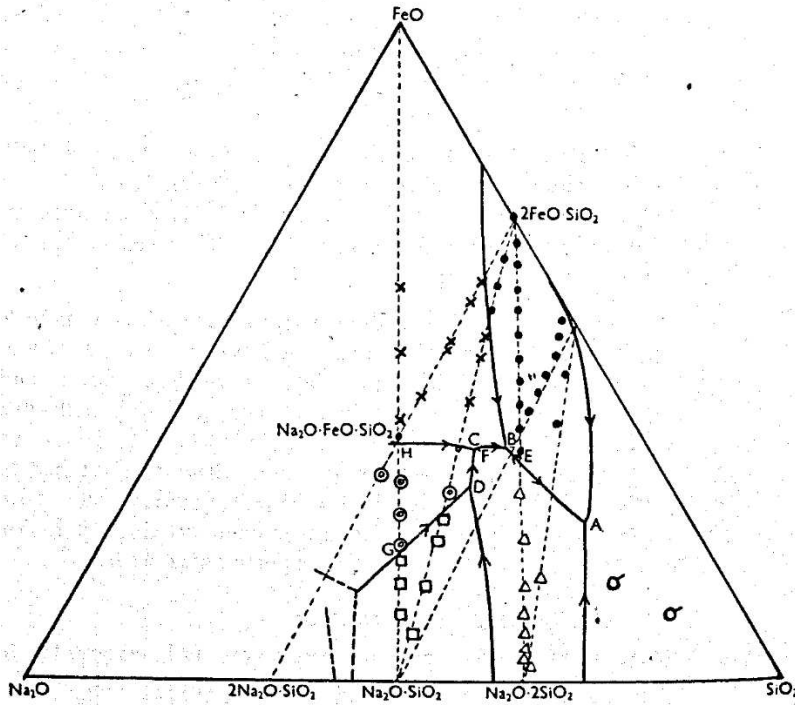


Figure 3.22 Primary Phase Regions with Experimental Points in the $\text{Na}_2\text{O-FeO-SiO}_2$ System. From [56]

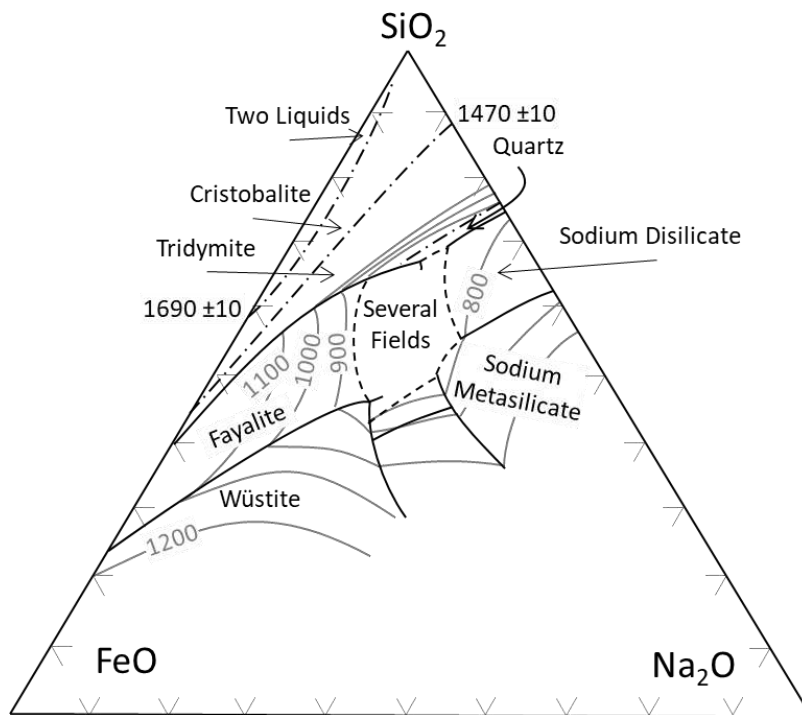


Figure 3.23 $\text{FeO-Na}_2\text{O-SiO}_2$ Phase Diagram, based on Schairer, Yoder, and Keene. From [57]

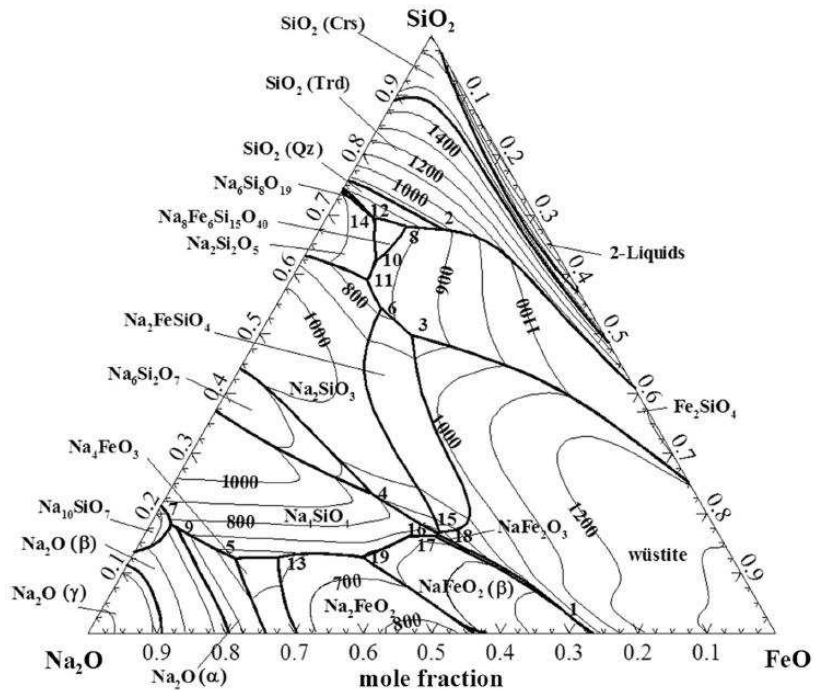


Figure 3.25 Calculated Liquidus Contours (in °C) and Primary Phase Regions for the Na₂O-FeO-SiO₂ System. From [51]

The system was also modeled as if in contact with air. Figure 3.26 compares the work of Bowen and Schairer with the thermodynamic calculation, while Figure 3.27 displays the calculated liquidus contours. In this oxidized system only the ternary NaFeSi₂O₆ and Na₅FeSi₄O₁₂ phases had compositions and melting behaviors which were accurately determined.

3.4.2.8 Na₂O-BaO-SiO₂

The Na₂O-BaO-SiO₂ system has been studied, and the primary phase diagram with liquidus contours (Figure 3.28) has been determined for silica contents greater than 40 mol%. [58] There exist three certain ternary phases: Na₂Ba₄Si₁₀O₂₅, Na₂BaSi₂O₆, and Na₂Ba₂Si₂O₇; as well as two probable ternary phases: Na₂Ba₁₈Si₂₈O₇₅ and Na₂Ba₄₅Si₇₃O₁₉₂. None of these phases exhibited solid solubility, yet almost all phases were accompanied by crystallization of metastable products.

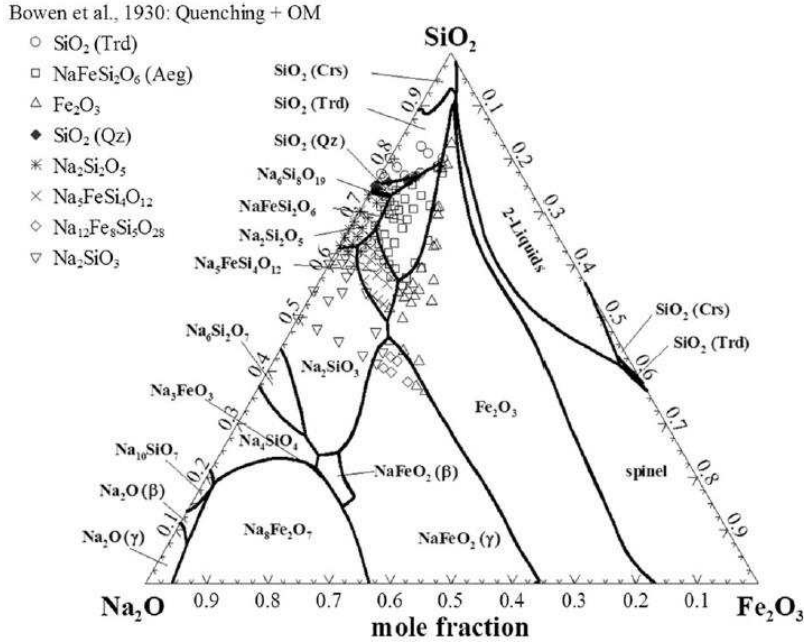


Figure 3.26 Calculated Primary Phase Regions and Previous Experimental Points in the Na₂O-Fe₂O₃-SiO₂ System. From [51]

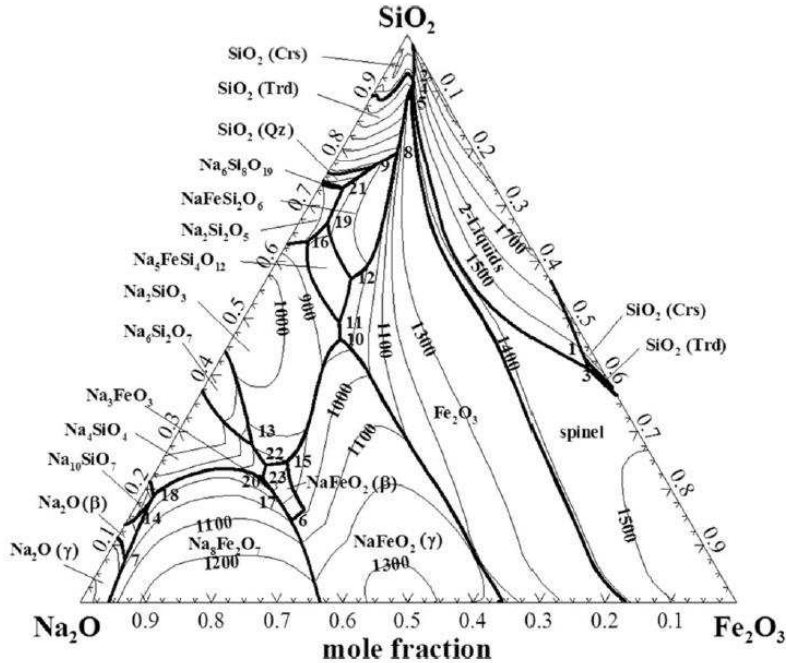


Figure 3.27 Calculated Liquidus Contours (in °C) and Primary Phase Regions for the Na₂O-Fe₂O₃-SiO₂ System. From [51]

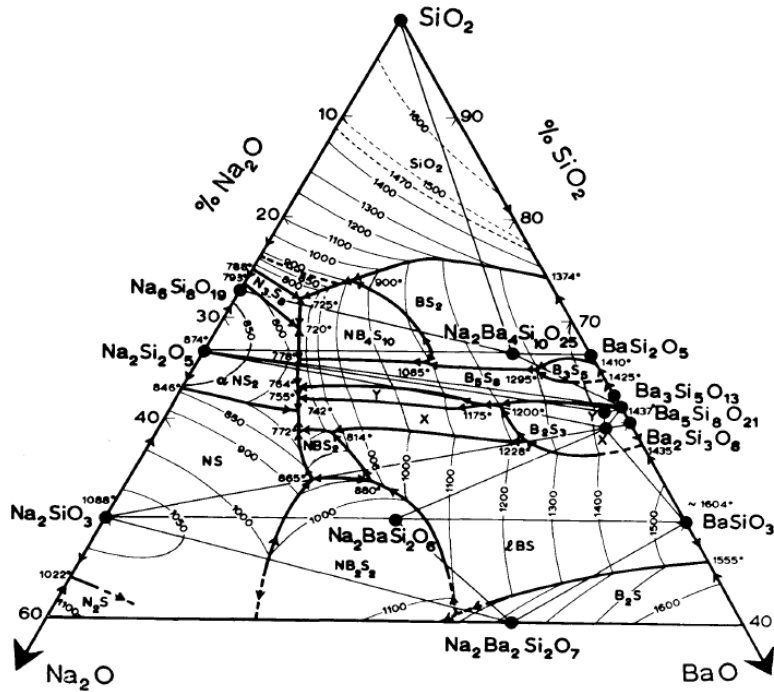


Figure 3.28 Primary Phase Regions with Liquidus Contours for the Na₂O-BaO-SiO₂ System. From [58]

3.4.2.9 Na₂O-PbO-SiO₂

The ACerS-NIST Phase Diagram Database contains the partial Na₂O-PbO-SiO₂ diagram (from pure SiO₂ to the PbO-Na₂SiO₃ join) shown in Figure 3.29. [55] On the diagram, the following phases are indicated by roman numerals: I = Na₂Pb₂Si₄O₁₁, II = Na₂Pb₃Si₁₆O₁₆, IV = Na₂Pb₂Si₃O₉, V = Na₂Pb₃Si₇O₁₈, VI = Na₆Pb₃Si₁₁O₂₈.

3.4.2.10 Other Oxide Systems

Phase diagrams could not be found for Na₂O-BaO, Na₂O-PbO*, Na₂O-As₂O₃*, BaO-FeO*, PbO-FeO*, As₂O₃-FeO*, Na₂O-BaO-FeO*, Na₂O-PbO-FeO, or Na₂O-As₂O₃-FeO, BaO-FeO-SiO₂*, PbO-FeO-SiO₂*, As₂O₃-FeO-SiO₂, or Na₂O-As₂O₃-SiO₂. Systems similar to those indicated with an asterisk (*) have been previously characterized or calculated, but these diagrams are excluded from current consideration because they include Fe₂O₃ or As₂O₅, lack completeness, or lack descriptions for the diagram. [55], [59]–[62]

Arsenic oxide forms compounds with sodium and iron oxides. [63] When all are present, the sodium arsenate Na₃AsO₄ will predominate until a stoichiometric excess of arsenic is reached and iron(II)

diarsenate $\text{Fe}_3\text{As}_2\text{O}_8$ will form. Adding silicon dioxide to this system will promote the formation of the iron(II) diarsenate by bonding with the sodium oxide to form the sodium silicate Na_2SiO_3 .

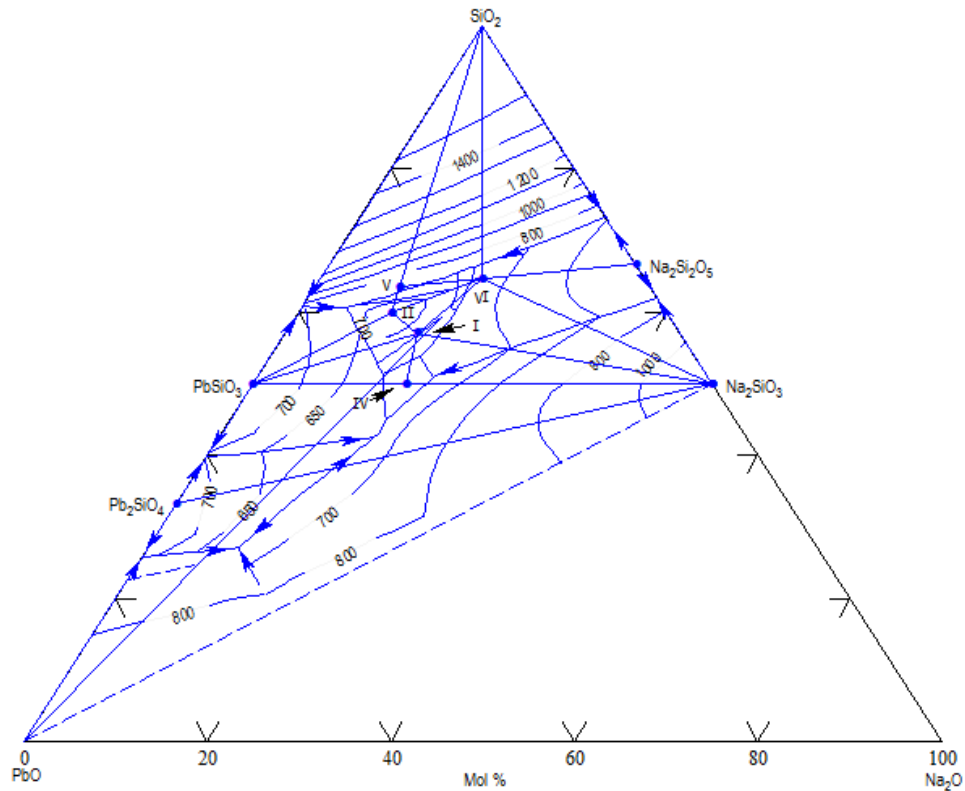


Figure 3.29 Approximation of the liquidus projection of the $\text{Na}_2\text{O-PbO-SiO}_2$ system. From [55]

3.4.3 Empirical Investigations of Solidified Slags

Identification and characterization of the distribution of lead-bearing phases in industrial slags and mattes were the goals of Beyke's 1995 study. [64] Three slags were detailed: one from a reverb-BF process, one from only a blast furnace, and one from a (sodium carbonate) desulfurization-reverb-BF process. As the third slag would be most relevant to the current study, it has been highlighted. Due to the desulfurization step, the glassy slag did not have an associated matte phase. It was composed of iron-sodium-calcium silicates, iron oxides and sulfides, and iron sulfates (with a total sulfur content of approximately 3 wt%). Metallic lead – occasionally containing impurities like iron, antimony, and arsenic – was found entrained in the latter phases. Tentatively-identified phases were $\text{Na}_2\text{Fe}_2\text{Si}_3\text{O}_{10}$ and

$\text{Na}_2\text{FeSiO}_2$. The silicate phases in the SEM images of Figure 3.30 appear dark, iron phases are gray and lead phases are white.

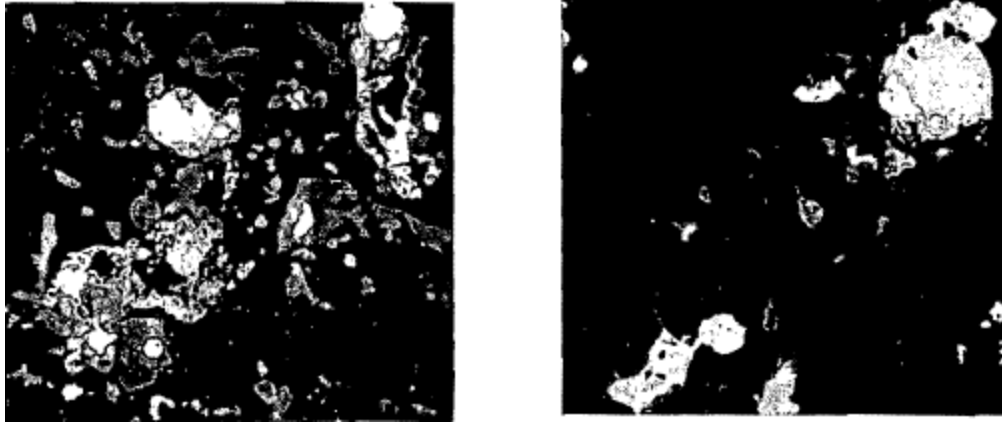


Figure 3.30 SEM backscattered images of desulfurized reverb-blast slag. Left: 200X magnification silicate matrix. Right: 620X, enlargement of upper-right corner of right image.

Lewis and Hugo also characterized a secondary lead slag. [65] A Scanning Electron Microscope (SEM) was used at a magnification between 1000X and 5000X in Energy Dispersive Spectroscopy (EDS) mode to qualitatively determine phases present in the unpolished slag samples. As Table 3.6 shows, the samples were predominantly a sodium-iron-silicate:

The white particles in SEM 1, 4, and 6 are $<2\text{-}\mu\text{m}$ prills of metallic lead or lead sulfide. Sodium sulfide and iron sulfide were expected (as seen in the amorphous, dark gray regions and columnar blocks, respectively, of SEM 2 and 3). The light gray area in SEM 1 is identified as an iron oxide matrix containing sodium and oxygen. Octahedral crystals of iron oxide spinels are shown in SEM 2 and 3.

If it meets certain particle size specifications (which vary by geographic region), blast furnace slag can be used as aggregate in concrete. Todo et al. investigated whether it was possible to produce high-density, coarse-grained slags through granulation. [66] As Figure 3.31 shows, the two are mutually exclusive when compared alone. However, when other material properties are considered (slag and water temperature, water velocity, etc.) and other processing steps are used (such as further grinding of a slag), production of a granulated slag with desired physical properties is shown to be possible.

Table 3.6 Average Composition of Lewis and Hugo's slag samples. [65]

Element	Average Concentration (Mass %)	Standard Deviation
Sn	0.7	0.3
Sb	.04	0.5
Pb	9.2	11.0
Fe	22.2	6.7
S	7.6	2.2
Zn	1.6	1.3
As	0.15	0.2
Al	1.2	5.3
Ca	1.3	0.3
Na	16.1	5.4
Si	(9.42)	

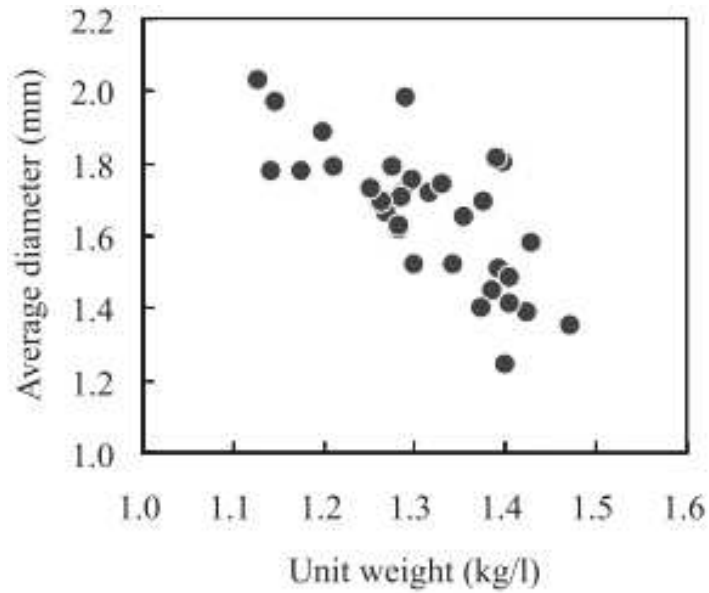
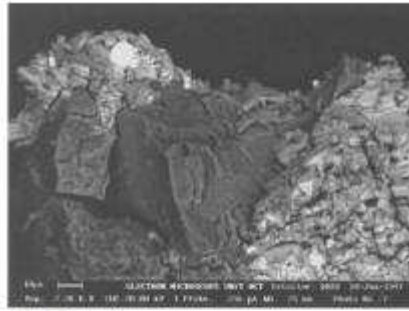
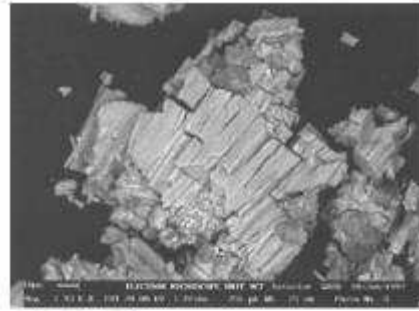


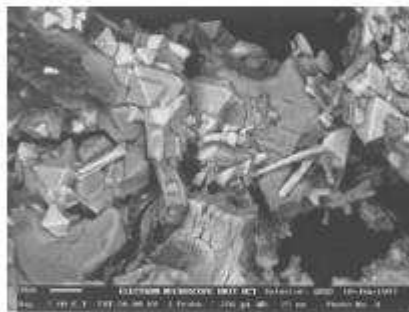
Figure 3.31 Relationship between Grain Diameter and Particle Density. From [66]



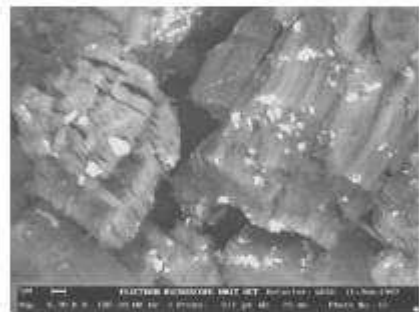
SEM 1



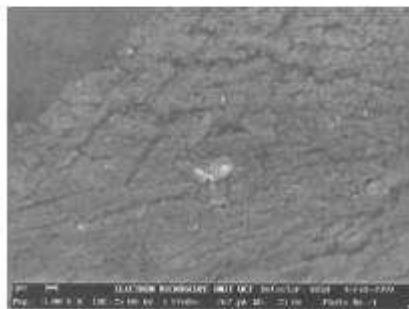
SEM 2



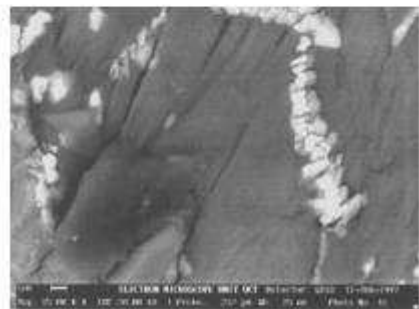
SEM 3



SEM 4



SEM 5



SEM 6

Figure 3.32 SEM images of a secondary lead slag. From [65]

3.5 Environmental Behavior

Metallurgical slags are most often treated as waste material. Exceptions do exist, as slags which have an appropriate composition and required physical properties (morphology, strength, etc.) can be used as construction aggregate, filler for new land, cement, or other materials. Whether disposed of as waste or used in other applications, slags must remain stable. Although it is unlikely for the silica to be removed from the matrix, given favorable Eh and pH of an environment other metals can become mobile (such as

zinc, cadmium, and nickel in an acidic or oxidizing environment). Table 3.7 below summarizes elements' mobility in various weathering conditions. [67] Queneau's 1991 paper sheds light on many formulations and applications of metallurgical slags. [68] Considering the potential effects of elements' mobility when a slag is disposed of as waste in a landfill (or elsewhere), the importance of regulatory testing becomes apparent.

Table 3.7 Relative mobilities of elements in soils and sediments exposed to weathering (From [67], [68])

Relative Mobility	System pH		Eh	
	Neutral-alkaline	Acid	Oxidizing	Reducing
Very High	Cl, S, Se	Cl, S	Cl, S	Cl
High	Na, Ca, Mg	Na, Ca, Mg, Zn, Cd, Ni	Na, Ca, Mg, Se	Na, Ca, Mg
Medium	Mn	Al, Cr, Pb, Cu	Cu, Ni, Zn, Cd	Mn
Low	K, Si, P, Fe, Pb, Zn, Cd	K, Fe ⁺³	K, Si, P, Pb	K, Si, P, Fe, Ni, Zn
Very Low	Al, Cr, Cu, Ni	Si	Al, Cr, Fe, Mn	Al, Cr, Cu, Pb, Cd, Se

3.5.1 Toxicity Characteristic Leaching Procedure (TCLP)

The United States Resource Conservation and Recovery Act of 1976 (RCRA) outlines the authority given to the Environmental Protection Agency (EPA) to manage solid and hazardous wastes. The EPA Code of Federal Regulations Part 261 defines the characteristics of regulated waste types and the limits for compounds that could classify a waste as toxic. [69] In the United States, it is the only regulatory test used for the disposal of hazardous materials. Producers of such material are therefore obligated to adhere to the test. The contaminant metals of interest to this investigation are listed in Table 3.8. EPA Method 1311 – The Toxicity Characteristic Leaching Procedure – states the procedure for determining a waste's toxicity characteristic. [70]

Due to the potentially harmful health and safety effects that these contaminants pose, their disposal must be carefully controlled. As it can be nearly ten times as expensive to dispose of a hazardous waste as to dispose of a non-hazardous waste, considerable effort is undertaken to ensure that waste meets regulatory compliance.

The TCLP has come under criticism for not accurately representing slag disposal conditions. Shortcomings which have been noted include: acetic acid not being representative of runoff drainage, such as from a mine; while a maximum particle size is given, no minimum size or distribution is given; and the test only involves a 24-hour leach, while conditions of a landfill may change (which affects the stability). Whatever its criticisms and shortcomings may be, it is the only suitable test used to meet regulatory requirements in the United States.

Table 3.8 Regulatory Limits for EPA contaminants relevant to metallurgical slags

Contaminant	Regulatory Level (mg/l)
Arsenic	5.0
Barium	100.0
Cadmium	1.0
Chromium	5.0
Lead	5.0
Mercury	0.2
Selenium	1.0
Silver	5.0

3.5.2 Empirical Investigations of Slag Environmental Behavior

In addition to SEM characterization, Lewis and Hugo tested a South African secondary lead smelter slag – the composition for which is given in Table 3.6 – under various regulatory tests, including the TCLP. [65] The results of several agencies’ tests are given below. The average concentration of lead in the extract, analyzed by ICP-MS, was found to be 96 ppm ($\sigma = 23.38$), while arsenic and zinc showed averages of 26 ppm ($\sigma = 3.28$) and 5.39 ppm ($\sigma = 1.63$) by the same means. Comment was made on both the impracticality of applying the TCLP (an acetic acid leach) to mineral processing wastes and the difficulty in meeting the TCLP filtering requirements, due to the fine particulate nature of the waste. The TCLP does not define a minimum particle size, but does dictate that samples be sieved to 100% passing 3/8”.

Jahanshahi *et al.* constructed and doped calcium-iron-silicate slags with arsenic, antimony, cadmium, zinc, and chromium and leached them according to the TCLP. [71] Oxidation states were

controlled through the ferric oxide to metallic iron ratio and kept under 10^{-7} atm to prevent magnetite formation in the iron silicate slags above 1300°C.

Arsenic and antimony were found to exist as As^{3+} and Sb^{3+} with some As^{5+} and Sb^{5+} . The latter species became more prevalent at higher oxygen potentials. When slow-cooled slags were analyzed, they were found to be crystalline with toxic elements distributed among the lower melting point phases. Samples with a larger particle size distribution were found to have lower levels of toxic elements in solution. Quenching the samples also led to lower levels in solution.

Table 3.9 Target composition of slag samples from [71]

Slag	Al ₂ O ₃	CaO	FeO	Fe ₂ O ₃	MgO	SiO ₂
CaFe2	0	20	30	48	2	0
CaFeSi1	0	20	31.5	41.5	2	5
CaFeSi2	0	20	32	29	4	15
FeSi1	1	1	50	13	5	30
BF1	15	30	0	0	10	45
BF2	15	30	0	0	10	45

Table 3.10 TCLP results for slag samples from [71]

Slag	Cooling	Particle Size	Liquor	Final pH	Arsenic mg/l	Antimony mg/l	Cadmium mg/l	Chromium mg/l	Zinc mg/l
CaFe1	slow	coarse	1	5.13	153.00	17.90	0.31	0.00	1.33
	slow	fine	1	5.48	276.00	31.10	0.21	0.00	1.77
	quench	coarse	1	4.98	65.10	13.20	2.40	0.00	1.24
CaFeSi1	slow	coarse	2	5.09	157.00	10.60	0.24	0.00	1.11
	slow	fine	2	7.00	164.00	13.00	0.01	0.00	0.90
	quench	coarse	2	4.30	63.20	7.65	1.42	0.02	2.15
CaFeSi2	slow	coarse	2	7.05	20.90	8.66	0.17	0.00	0.14
	slow	fine	2	8.54	48.20	8.03	0.01	0.00	0.12
	quench	coarse	2	6.90	36.90	5.82	2.39	0.00	1.39
FeSi1	slow	coarse	1	4.96	4.71	3.99	0.46	0.02	1.23
	slow	fine	1	4.99	8.43	7.19	0.72	0.15	2.01
	quench	coarse	1	4.91	1.30	0.75	0.57	0.02	0.80
BF1	slow	coarse	1	5.00	3.12	3.27	0.55	0.00	4.51
	slow	fine	1	5.00	4.48	5.68	0.69	0.06	6.28
	quench	coarse	1	4.90	5.00	2.24	24.10	0.03	1.25
BF2	slow	coarse	2	4.47	45.60	18.90	32.40	0.06	43.10
	slow	fine	2	4.84	59.10	10.80	47.50	0.05	69.00
	quench	coarse	1	4.93	0.84	0.58	0.60	0.03	0.63

CHAPTER FOUR EXPERIMENTAL METHODS AND MATERIALS

Experiments were carried out in two realms: determining viscosity and density of molten slags and evaluating the TCLP response of impurities within those slags. Before experiments were carried out, thermodynamic modeling was used to predict which phases would develop. Slags were produced synthetically from reagent-grade powders. The crucibles used to contain the slags were made from alumina, and the spindles which were immersed in them were molybdenum. Ultra-High Purity Grade argon was used to prevent oxidation of iron in the slags, and a variety of analyses were employed post-mortem to determine phase distributions and compositions.

4.1 Selection of Slag Recipes

A suite of compositions to be tested were determined using Stat Ease's Design Expert 9 software. After normalizing an industrial smelter's slag composition to the three major components, a region of the ternary phase diagram which contained that point was bounded and thirteen compositions were generated. The resulting points are displayed graphically on the Na₂O-FeO-SiO₂ ternary diagram in Figure 4.1 and tabulated in Table 4.1. Of those thirteen recipes, six produced reliable viscosity results (thin border in the figure; *italicized* in the table) and four were chosen for the TCLP response investigation (thick border in the figure, **bold** in the table). Two compositions were tested for both investigations (double-bordered in the figure, ***bold italicized*** in the table).

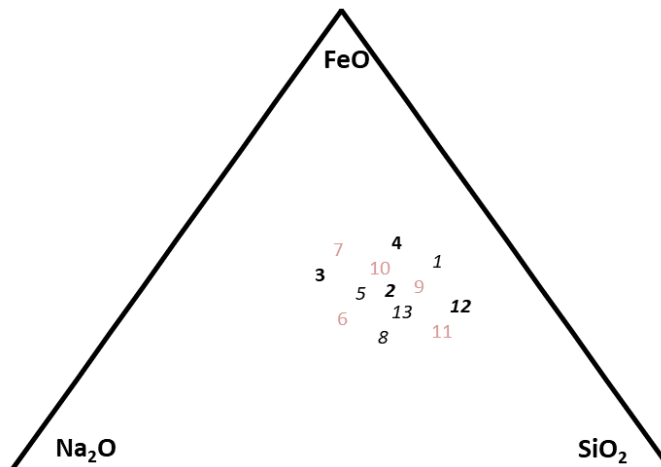


Figure 4.1 Experimental Points presented in the Na₂O-FeO-SiO₂ ternary space. TCLP tests' labels are **bold**, successful viscosity tests' labels are *italicized*, and unsuccessful viscosity tests' labels are red.

Table 4.1 Experimental Compositions (in weight percent). Bold entries signify TCLP tests, *italicized entries* signify successful viscosity tests, and red entries signify unsuccessful viscosity tests.

Recipe	Na ₂ O	FeO	SiO ₂
4	16.667	49.667	33.667
<i>7</i>	<i>26.250</i>	<i>48.250</i>	<i>25.500</i>
<i>1</i>	<i>12.583</i>	<i>45.583</i>	<i>41.833</i>
<i>10</i>	<i>22.167</i>	<i>44.167</i>	<i>33.667</i>
3	31.750	42.750	25.500
<i>9</i>	<i>18.083</i>	<i>40.083</i>	<i>41.833</i>
<i>2</i>	<i>22.875</i>	<i>39.375</i>	<i>37.750</i>
<i>5</i>	<i>27.667</i>	<i>38.667</i>	<i>33.667</i>
12	14.000	36.000	50.000
<i>13</i>	<i>23.583</i>	<i>34.583</i>	<i>41.833</i>
<i>6</i>	<i>33.167</i>	<i>33.167</i>	<i>33.667</i>
<i>11</i>	<i>19.500</i>	<i>30.500</i>	<i>50.000</i>
<i>8</i>	<i>29.083</i>	<i>29.083</i>	<i>41.833</i>

4.2 Thermodynamic Modeling

Outotec's HSC software package was used to model the relevant sodium-iron-silicate-barium, -lead, and -arsenic systems. By inputting the amounts of sodium, iron, silicon, oxygen, barium, lead, and arsenic called for by the recipes (and ultimately the Fe³⁺/ΣFe from the Satmagan), the equilibrium phase compositions at two relevant temperatures were determined. Those chosen were 1200 °C and 700 °C, to represent the phases which may have frozen in place while the slag was still molten and those which developed under slow cooling as the slag crystallized.

4.3 Measurement of Viscosity and Density

For the viscosity and density determinations, a Brookfield LVDVE viscometer with a custom spindle attachment and an Ohaus Pioneer digital balance were used to record data. These instruments were placed on a movable platform, under which a vertical tube furnace was mounted. The reaction vessel was constructed from mullite with a steel cap which contained an opening large enough for the spindle to pass through and rotate freely. Argon was introduced at 500 ml/minute to maintain a protective atmosphere and positive pressure in the reactor.

To meet the depth requirement for the viscosity measurements, half of the total sample mass was initially melted and cooled in a Deltech box furnace. The second half of the mass was added when the sample was placed in the tube furnace. Heating took between 11 and 17 hours, depending on the rate

employed. Some samples' crucibles cracked on heating, so the initial 2.5 °C/minute heating rate was reduced to 1.5 °C/minute.

Once the slags were heated to 1300 °C, they were held at the temperature to equilibrate for one hour. At that point, the spindle was lowered until the viscosity reading rose to ~2% or the mass on the balance changed substantially – either phenomena indicated that the top of the melt had been contacted. To measure the density, the spindle was lowered one centimeter into the melt and the depth and mass were recorded. Then it was lowered approximately another centimeter and the measurements were repeated. After that, the spindle was withdrawn from the melt and attached to the viscometer. The platform was lowered until the spindle was three centimeters immersed in the melt and the percent torque at each RPM was recorded from high to low. The range of usable RPM varied: if the motion at higher RPM (100 or 60) was deemed too erratic, the value was not recorded. The low end of usable RPM was determined by the torque value. When the viscometer displayed a torque percent less than 10%, no lower-RPM readings were taken, as that one and those for lower RPM were considered unreliable.

4.4 Determination of Leaching Characteristics

The second body of work in this study was to determine the leaching characteristics of arsenic, barium, and lead from four slag compositions cooled either quickly or slowly. The four base recipes were doped with zero, one, or five percent of an impurity –barium hydroxide, lead oxide, or arsenic oxide. As the decomposition of barium hydroxide to barium oxide has been noted before, it was used as a substitute. [72] The reagent powders were weighed, mixed, and poured into 750-mL alumina crucibles from AdValue Technology.



Figure 4.2 A Batch of Powder-Filled Crucibles Ready to be Heated.

To heat the slags, a 5.3 ft³ box furnace from Deltech Furnaces Inc. with molybdenum disilicide elements was used. The controller was programmed to dwell for three hours to allow the furnace to fill with argon, heat to 1,200 °C at 2 °C per minute, hold for 90 minutes, then cool to room temperature at 2 °C per minute. After 60 of the 90 minutes passed at 1,200 °C, the furnace was opened and four of the slags were removed one at a time and poured into a room-temperature cast iron mold. The argon flow was stopped, and the four remaining slags were allowed to cool as programmed. All eight slags were then massed, crushed, split, and sent to an external lab for assaying and TCLP extraction.

Once the TCLP leach results were obtained, the samples that leached the most and least were mounted and imaged with a scanning electron microscope. These samples were then leached in 0.1M acetic acid for 22 hours, and imaged again.

4.5 Analytical Techniques

The analytical methods employed by this study were thermodynamic modeling (Gibbs Energy Minimization) with Outotec's HSC software package, inductively-coupled plasma optical emission spectrometry (ICP-OES), X-Ray Diffraction (XRD), X-Ray Fluorescence (XRF), imaging using a Scanning Electron Microscope (SEM), Energy-Dispersive X-ray Spectroscopy (EDS), and Satmagan analysis.

4.5.1 ICP-OES

Gopher Resource performed the chemical analysis of the slags (via digestion) and of the TCLP extracts using ICP-OES. Samples provided to Gopher were crushed to minus 3/8" using a jaw crusher. Oversize material was crushed with a roll crusher set to a 1/4" gap so that all material was 100% passing 3/8". These samples were then split according to the sample mass on hand (between 150 and 400g) and mass desired (150g for all tests) using a Jones Riffle. The samples were screened at 16 mesh to provide material (the undersize from that screening) for the Extraction Fluid Determination. The oversize was split into subsamples assaying and TCLP extraction.

The subsamples were leached according to EPA Method 1311, which is an 18 ±2 -hour agitated leach in an acetic acid solution. After leaching, the solution was filtered from the sample, separated into aliquots, and analyzed for eight metals (arsenic, barium, cadmium, chromium, lead, mercury, selenium, and silver) by ICP-OES. For the assay, subsamples were digested using a microwave-assisted four-acid digestion, and those digestions were analyzed with ICP-OES.

4.5.2 Microscopy and Spectroscopy

Several types of x-ray spectroscopy were employed in analyzing the slags. Crystallinity was estimated using x-ray diffraction (XRD), elemental compositions were estimated using standardless x-ray fluorescence (XRF), and observed phases were imaged with a scanning electron microscope (SEM) and estimated using energy-dispersive x-ray spectroscopy (EDS).

A compound's XRD spectrum shows unique relative intensities at specific 2θ peaks. The spectrum from an unknown crystalline sample can then be compared to a catalog of known samples to determine its crystalline composition. If a compound has amorphous content, however, this will show up on its spectrum as a broad hump in the low-angle region.

X-Ray fluorescence (XRF) and EDS both rely on atomic structure to determine composition. When atoms are hit with x-rays released from a high-voltage source, electrons from inner shells are ejected. In order to minimize the potential energy of the atom, electrons from outer shells fall to the now-vacant spot, and release a characteristic x-ray. Because the shells of different atoms are spaced at unique specific radii from the nucleus, the energy or wavelength of the characteristic x-ray can be detected and, when compared to the intensities of other energies or wavelengths detected, used to determine the composition of the specimen.

Whereas an optical microscope uses light to record an image, an SEM uses electrons. A high electrical potential is created between the source and the instrument, which causes it to eject a beam of electrons. A series of electromagnetic lenses control the size and shape of the beam, which is focused on a spot on the sample. As that spot rasters across the sample, a detector is used to create an image of the sample. An SEM can be used in one of two modes to determine the topography (secondary electron mode) or the composition (backscattered electron mode) of a sample. Secondary electrons are low-energy electrons produced from the shells of the atoms following interaction with the incident electron beam, while backscattered electrons are high-energy electrons detected after rebounding off the atoms. Heavier atoms rebound more electrons than lighter ones, so bright spots appear in the images where heavier elements are present.

4.5.3 Satmagan Analysis

In order to determine the magnetic content of the slag samples, a Satmagan was employed. Standards were made up using pure silica and magnetite (reagent-grade Fe_3O_4). Once a linear calibration curve was obtained with the standards (Section 0), pulverized slag samples of the same mass were tested

to determine their magnetite content. The magnetite content (from the Satmagan) was used to determine the experimentally-achieved $\text{Fe}^{3+}/\Sigma\text{Fe}$ ratio used in the final thermodynamic modeling.

CHAPTER FIVE

EXPERIMENTAL QUALITY CONTROL

Defined by Montgomery, quality means “fitness for use” and is “inversely proportional to variability.” [73] In order to demonstrate the fitness for use and limit the variability in the data acquired as part of this work, numerous checks were performed to validate assumptions and illustrate the repeatability of the measurements.

5.1 Slag Composition

Slags were designed to meet composition targets in the Na_2O - FeO - SiO_2 ternary space, with the impurities making up 1.00%, 1.83%, 5.00%, or 8.84% of the total sample weight. Confidence in these compositions stems from four areas: high purity of the reagents, properly calculated compositions, and accurately massed recipe ingredients

5.1.1 Reagent Purity

Specifications for the reagents used in this study are given in Table 5.1. It should be noted that the sodium oxide was only 80% pure, with the remaining 20% being sodium peroxide. As compensation for the extra oxygen, recipes that used sodium oxide were adjusted to use more iron and less iron oxide to reach the FeO target. Barium hydroxide was used instead of pure barium oxide, as it has been shown that it decomposes to barium oxide at temperatures lower than that at which the slags were equilibrated. [72] The mass of barium hydroxide to be added was calculated assuming use of a nonahydrate, but in practice, anhydrous barium hydroxide was used. This miscalculation was not corrected until after completion of the experiments, so the actual amount of barium oxide included was higher than the 1% and 5% targets.

5.1.2 Crucible Interactions

A variety of materials were tested to determine which might be sufficient to contain the slags. These included graphite, silicon carbide (with and without a boron nitride coating), castable refractories, and alumina. Graphite crucibles were seen (Figure 5.2) to react with the slag by reducing the iron. In the figure, two regions of reduced iron can be seen at the edges of the crucible’s bottom face. Whether this reaction occurred at an appreciable extent while the slag was molten was not determined, but its effect on the phase distribution after cooling was seen as detrimental.

Table 5.1 Reagent Specifications

Reagent	Grade	Vendor
Na ₂ SiO ₃	Anhydrous, technical	Alfa Aesar
Na ₂ O	80% (20% Na ₂ O ₂)	Sigma Aldrich
SiO ₂	99.5%	Alfa Aesar
Fe	Approximately 40-mesh filings	Fisher
Fe ₃ O ₄	97%	Alfa Aesar
PbO	99.9%	Alfa Aesar
Ba(OH) ₂	Anhydrous, 95%	BeanTown Chemical
As ₂ O ₃	99.5%	Alfa Aesar

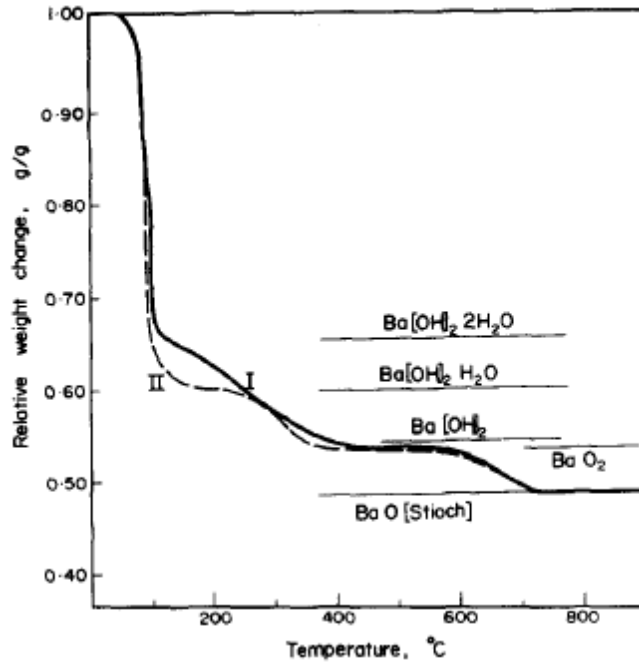


Figure 5.1 TGA curves for (I) recrystallized barium hydroxide octahydrate and (II) barium hydroxide octahydrate prepared by the rehydration of the monohydrate. From [72]

Silicon carbide crucibles were also investigated. Initially, they showed promise for re-use as several slags either cleanly poured out of them or left little enough residue that it could be scraped from the walls. However, the compositions of successive slags were seen to be changing from their (common) target. Applying a boron nitride coating (to prevent reaction with the crucible wall) proved to be of little

value. Either due to misapplication leading to cracks or to chemical reaction with the coating, the slag formed a spongy mass and did not pour from the crucible. Silicon carbide was deemed unsuitable.



Figure 5.2 Bottom Face of Slag Contained in a Graphite Crucible. Regions of reduced iron are circled in red.



Figure 5.3 Silicon Carbide Crucible Coated with Boron Nitride. From left to right: before heating slag, immediately after heating slag to 1200 °C, and after cooling to room temperature.

Castable refractories were applied to the silicon carbide crucibles to determine the effect of using materials similar to those in industrial practice. Specimens containing slags after heating are shown in Figure 5.4. Both refractories experienced slag infiltration; the slag pictured on the right displayed an excessive amount. Impurities were also seen in the slags.

The container material which displayed the least drift in composition was alumina. Figure 5.5 demonstrates the pros and cons of the alumina crucibles. On the left and bottom-left edge of the crucible, the minimal amount of slag attack on the crucible wall can be seen. However, the crucible interface which was exposed is the result of a small crack – the slag wetting through the crucible can be seen in the

discolored bottom edge. It was thus determined that alumina should be used for its good-quality slag compositions, but the heating and cooling rates would have to be carefully controlled to avoid cracking the crucibles.



Figure 5.4 Two Crucibles Coated with Different Castable Refractory Compounds Containing a Slag, after heating.



Figure 5.5 Alumina Crucible Containing a Slag After Heating. Discoloration due to slag wetting a crack is indicated with red arrows.

5.1.3 Before-and-after Comparison

The data in APPENDIX C show that in general, there was good agreement between the targeted and actual compositions. One potential concern with using alumina crucibles was that alumina might

leach into the melts. This proved to be an unfounded concern, as no sample had more than 2.5 wt% Al_2O_3 . Actual sodium oxide contents were around one percent lower than their targets, with slightly less in the high-sodium melts. This was expected given the tendency for sodium oxide to volatilize during the heating cycle. Iron and silica compositions were around five percent (on average) lower than their targets. Barium, lead, and arsenic oxides were almost all within one weight percent of their targeted values. The exceptions were 1.28% and 1.11% for two arsenic tests, and several percent for the composition-outlier tests.

For the composition outlier tests, the argon flow was incidentally stopped earlier than the other tests. This likely exposed the samples to oxygen during the equilibration time. Their high mass recoveries point to this, as oxidation of the iron would increase the mass. This extra mass would also decrease the actual percentages of every (non-oxygen) constituent, which was also observed.

5.2 Furnace Environments

Two furnaces were used in this study: a custom-built 5.32 ft³ box furnace from Deltech Furnaces Inc. and a vertical tube furnace from Micropyretics Heaters International Inc., both heated using molybdenum-disilicide elements. Ultra-High Purity argon (99.999% Ar) was used to establish a protective atmosphere to limit the oxidation of the slag.

5.2.1 Temperature Verification and Profiles

An external Pt/Pt-Rh 13% thermocouple was used to monitor the temperature inside the reaction tube during operation. An illustration of the temperature profile while the furnace held temperature at 1,014 °C is provided in Figure 5.6. The height from the bottom is marked, and outlines of the crucible and crucible holder are given. It can be seen that at the base of the crucible, the temperatures are almost identical, and that the temperature as recorded from the sheath hanging above the crucible is approximately 60 °C lower than the temperature read in the hottest zone.

The box furnace was used to slowly cool the slags at a nominal rate of 2 °C per minute (0.5 °C/min for the extra-slow cooling rate). Figure 5.7 shows that this was true for the upper half of the cooling regime; up until approximately 500 °C. Around that point, the actual furnace temperature fell at a rate slower than that which was programmed.

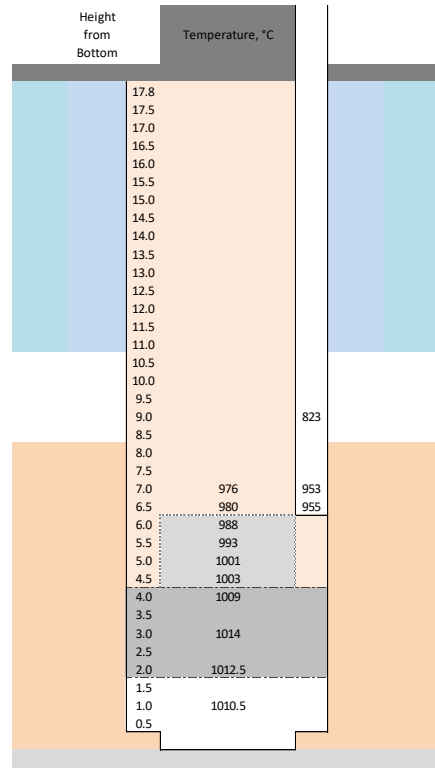


Figure 5.6 Tube furnace temperature versus height profile.

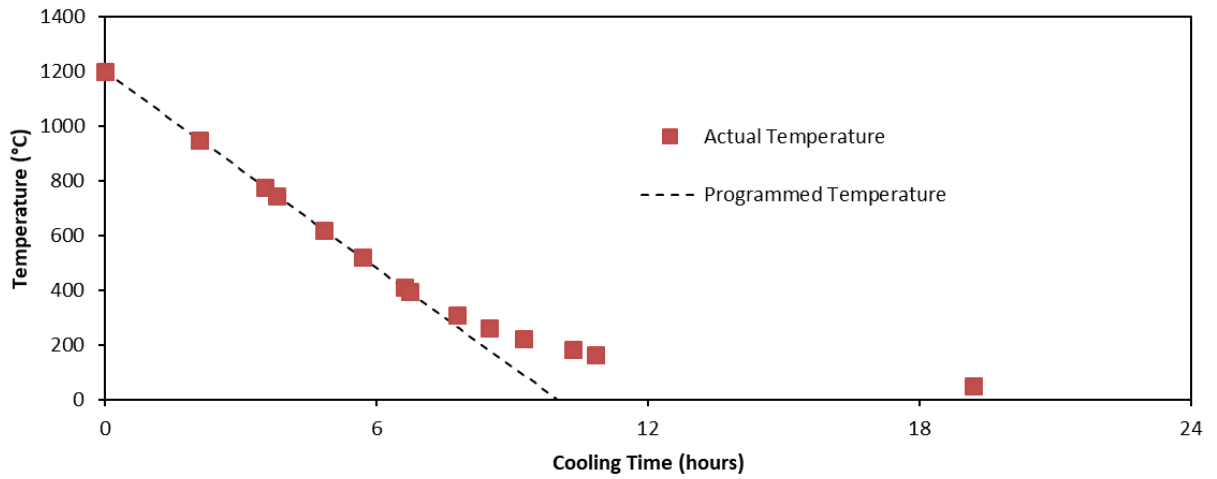


Figure 5.7 Box furnace temperature versus time profile.

5.2.2 Establishment of Protective Atmosphere

For the tube furnace, a flow rate of 500 mL/minute was used to retain a protective atmosphere above the slag. In the box furnace, this rate was increased to 1.9 L/minute. To fill each reaction space, a dwell of 60 minutes and 180 minutes was used in the tube and box furnaces, respectively.

5.3 TCLP Slag Preparation

When samples were sent away for TCLP analysis, they were given a simple source, batch, and number designation (DJS-A-1, DJS-E-15, etc.). A list was kept of which sample had been given which designation. The actual sample descriptions (recipe, cooling rate, impurity, amount, etc.) were not given to the laboratory. Once data was returned, the leach and digestion results were assigned back to their corresponding samples.

5.4 Calibration of Instruments

Several steps were taken to ensure the data recorded from the equipment used in this study were reliable. These included calibration, comparison to reference fluids, and periodic checks to standards.

5.4.1 Viscometer Calibration

Before experiments began, the viscometer was factory-calibrated by Ametek-Brookfield. A silicone oil from Brookfield with a certified viscosity of $4,965 \pm 50$ cP ($\pm 1\%$) was tested with a standard spindle to ensure the viscometer was indeed functioning properly. Figure 5.8 shows the viscosity as a function of RPM. As expected, the Brookfield Spindle points are almost exactly where they should be. The gray dotted lines in the figure represent the acceptable error window, consisting of the fluid error (1% of the certified value), and the viscometer error. The viscometer error is based on the Full-Scale Viscosity Range (FSVR):

$$FSVR = \frac{SMC \times TK \times 10,000}{RPM}. \quad (5.1)$$

The FSVR represents the maximum viscosity that can be calculated using a given spindle and RPM combination. The viscometer error is one percent of this value.

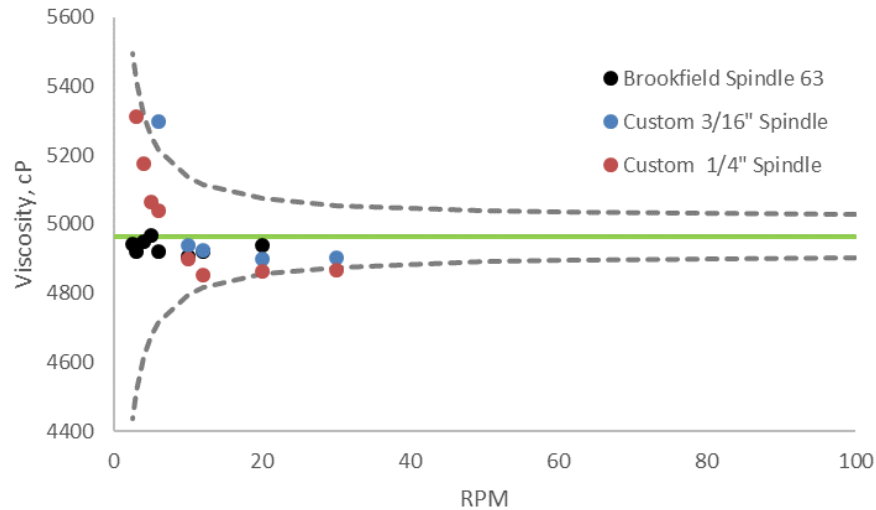


Figure 5.8 Viscosity of Brookfield 5,000-cP standard oil.

Raw data was recorded from the viscometer as a percent torque at a given RPM. Equations 3.19 and 3.20 were used to transform the spindle RPM and percent torque into shear rate and shear stress values. The spindle code *SMC* for the custom spindle was computed using equation 3.23. In that equation, the length *L* used in the calculation was the effective length, which is slightly larger than the immersion depth. The factor used to determine the effective length was approximated by finding the ratio of the effective length to spindle length for similarly-sized Brookfield custom spindles. Final values chosen were those that raised the viscosity into the acceptable error window. In this case, the empirical correction matched up well with the physically-defined constant.

The tails toward a higher viscosity at low RPM are obvious for both custom spindles. Because this tail is not observed in the curve for the Brookfield spindle, it is assumed to be a result of the custom spindles wobbling as they rotate. Since the viscosity values still fell within the acceptable error window for the standard spindle (which is tighter than that of the custom spindles because the *SMC* is lower), no further correction was made.

Using a 3/16"-diameter spindle at 60 RPM, the lowest viscosity that would be measurable is 44 ± 44 cP, taken from a reading of 1% torque. Brookfield cautions against using values under 10% torque, as a reading of that level carries a relative error of 10%, and that error rises quickly below that point. The 44-cP viscosity has a relative error of 100%. To ensure that the viscometer calibration extended to these extremely low values, a 94.6 ± 9.5 cP fluid was also tested, and the data and errors are

given in Table 5.2. That data shows that although the relative error is quite large (up to 71 %), the certified viscosity value was still within the error window for the measurement.

Table 5.2 Calibration Values for 94.6 ± 10 cP Standard Fluid

RPM	% Torque	Viscosity, cP	Relative Error
60	3.7	97 ± 26	27 %
50	1.6	70 ± 44	63 %
30	1.4	73 ± 52	71 %

After the spindle factors were determined, the spindles were used to test the viscosity of boron oxide. The values recorded were compared with those reported previously by Napolitano *et al.* and are displayed in Figure 5.9. [74]

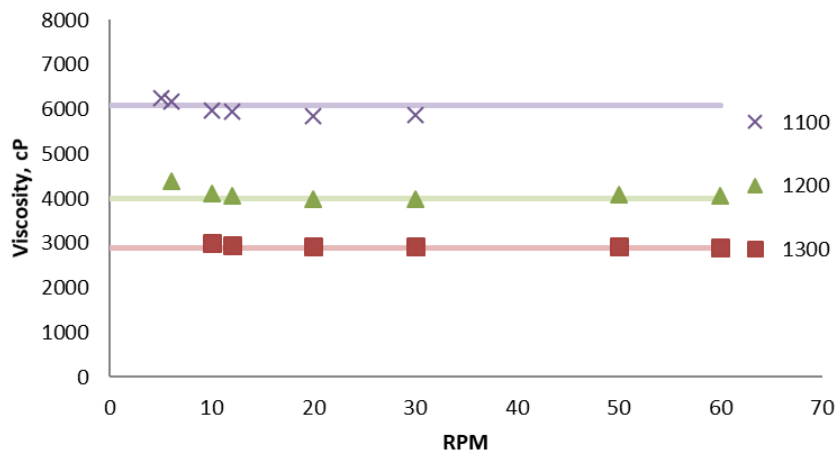


Figure 5.9 Viscosity of B_2O_3 . Lines represent data taken from Napolitano *et al.* (from [74]), while points represent experimental observations from this study.

5.4.2 Balance Calibration

Accuracy of the balance during measurement was limited to one hundredth of a gram due to noise caused by convective currents rising from the spindle port. Its precision was periodically calibrated against an assay-ton standard weight.

The densities of water and a saturated sodium polytungstate solution were measured as standards. Fluid was measured into a 10-mL volumetric flask and massed. Then, the fluid was placed into a 50-mL centrifuge vial and the spindle was used to measure the mass change. From this value, the density was recorded. The results of this validation are shown in Table 5.3.

Table 5.3 Density Setup Room-Temperature Validation Data

Fluid	Reported Density, g/mL	Experimental Density, g/mL	Percent Error
Water	0.999	1.06	6.11%
Sodium Polytungstate	3.10	3.14	1.29%

5.4.3 Satmagan Calibration

The Satmagan was calibrated using four mixtures of reagent-grade magnetite and silica. The samples were 0 wt% magnetite (pure silica), 10 wt% magnetite, 50 wt% magnetite, and 100 wt% magnetite. The curve is displayed in Figure 5.10 along with the equation of the line and the R^2 value (of 0.9962).

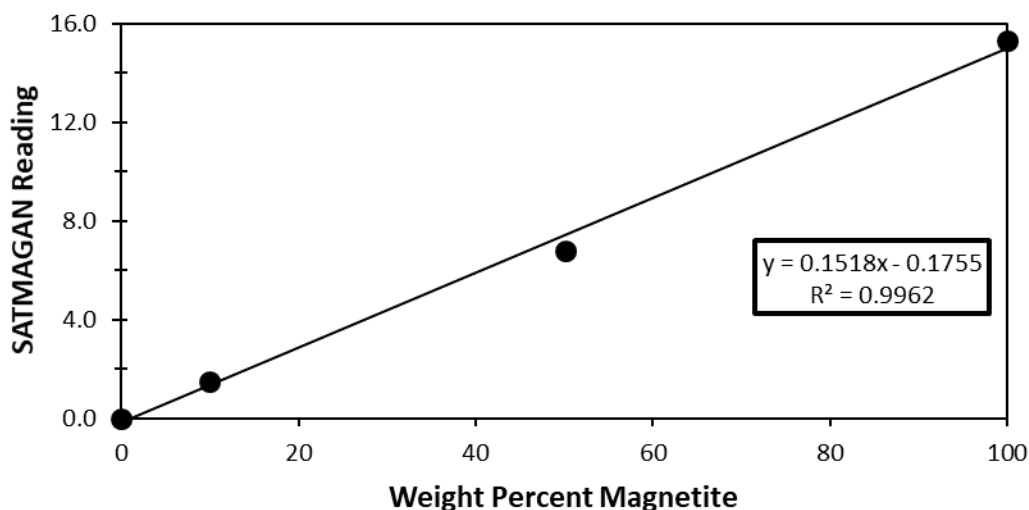


Figure 5.10 Satmagan Calibration Curve.

5.5 Discussion of Errors

The data collected in this study was not without error. Three areas for which error will be discussed are the assumption of Newtonian behavior of the slag viscosities, the spindle geometry assumptions for the viscosity and density, and the repeatability of leaching tests on the slags.

5.5.1 Viscosity

As the viscometer displayed a percent torque which was then converted into a viscosity value, the assumptions and errors of that calculation method must be addressed. The fundamental principle behind using the viscometer is that slags are Newtonian, and that shear stress varies linearly with the shear rate (Equation 3.3). The constant which relates the two terms is the viscosity.

Once the data for a sample is recorded, it must be decided if it is Newtonian. In a true Newtonian fluid, the intercept of the shear stress - shear rate trendline should be zero. A non-zero intercept would represent Bingham plastic behavior – meaning that there is some minimum shear rate that must be exceeded for flow to occur – and contradict the assumption that the fluid is Newtonian. The statistics given in Table 5.4 are exemplary of the data recorded in these tests. After a linear least-squares regression was performed, the slope, intercept, and R^2 value for each temperature's shear stress–shear rate series were calculated (and are given in blue). That some intercepts are positive and some are negative is indicative of this intercept being the result of errors and that the fluid is likely not a Bingham plastic. Because of this phenomenon, the slopes used in later calculations were those generated by forcing the intercept to be zero (the purple columns).

If the intercept is assumed to be zero, then a viscosity can be calculated by dividing each shear stress by the shear rate at which it was recorded. Plotting the data from this method yields Figure 5.11. For a true Newtonian fluid, all the viscosities (for one temperature series) calculated in this manner would be the same and they would equal the slope found above when setting the intercept to zero. To compare this method to the previous one, this data is placed in Table 5.4 in tan. If the fluids were perfectly Newtonian and there was no error in the data, the tan intercept would be the same as the tan average viscosity (η_{AVG}), and it would also be equal to the purple and blue slopes.

Table 5.4 Regression Statistics for Sample 1.

TEMP	SLOPE	RSQ	INT	SLOPE(0)	RSQ(0)
1299	639	0.9918	-753	569	0.9982
1199	1090	0.9940	-25	1087	0.9987
1100	3376	0.9993	392	3477	0.9992
1000	11226	0.9999	1140	11964	0.9974
900	75197	0.9977	-214	78005	0.9991
INT	η_{AVG}	RSQ	$\log \eta$	$\log \eta$	$\log \eta$
473	556	0.8082	2.75	2.81	2.75
1057	1077	0.0334	3.03	3.04	3.04
3934	3681	0.4367	3.57	3.53	3.54
15781	13766	0.5003	4.14	4.05	4.08
86109	77057	0.4896	4.89	4.88	4.89
		RSQ (T)	0.9951	0.9866	0.9917

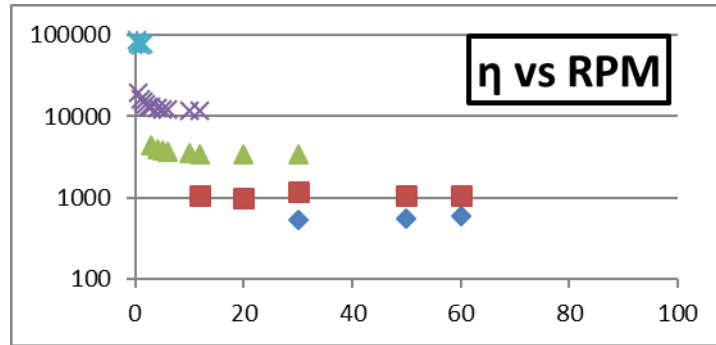


Figure 5.11 Viscosity as a function of RPM for Sample 1.

There are several indications that error exists in this calculation, or that the assumption of Newtonian behavior is incorrect. The tan intercept value is higher than the average value, indicating a rise in viscosity at lower RPM. This increase is shown clearly in Figure 5.11. However, it has been demonstrated that the error in viscosity measurement increases as RPM decreases. In the calibration plot using the Brookfield standard oil (Figure 5.8), this rise can be seen, but the values are still within the acceptable error limits. The error in a viscosity measurement is stated by Brookfield as 1% of FSVR. Thus, error bars in the log viscosity versus reciprocal temperature plot are equal to 1% of the FSVR for the lowest RPM used in the series.

Another explanation for the rise in viscosity in the experimental samples could be the influence of precipitated solid particles. Tests were knowingly performed at temperatures close to and below the liquidus boundaries for primary phases. It would not take a large volume fraction of solids to have an

influence on the viscosity. [75] Precipitation (phase segregation) would also change the composition of the liquid, which would in turn affect the viscosity. This phenomenon could not be avoided, so only those melt viscosities believed to contain minimal influence of solids are reported. Complete data sets are presented in APPENDIX A, as they still have relevance for industrial melts in the composition and temperature ranges studied.

Table 5.5 Viscosity data as a function of RPM.

RPM \ °C	Viscosity, cP				
	1299	1199	1100	1000	900
100					
60	590	1,080			
50	547	1,073			
30	531	1,175	3,461		
20		987	3,414		
12		1,072	3,424	11,698	
10			3,480	11,639	
6.0			3,680	12,039	
5.0			3,743	12,165	
4.0			3,911	12,538	
3.0			4,338	13,013	
2.5				13,335	
2.0				14,110	
1.5				14,914	77,886
1.0				16,230	75,303
0.6				19,740	77,983
0.5					82,175
0.3					88,219

5.5.2 Density

To assess slag adhesion to the spindle, it was imaged after being fully withdrawn from the melt and allowed to cool. Qualitatively, these images (Figure 5.13) show that the slag adhered to the spindle, at least at the lowest temperature tested. Combined with the mass readings taken when the spindle was suspended above the melt (between immersions), it can be assumed that *some* slag stuck to and eventually solidified onto the spindle after every immersion. This extra slag would make the effective radius of the spindle higher, which would increase the mass difference. By using the initial radius and not the actual radius of the slagged spindle, the reported densities would be higher than their true values.

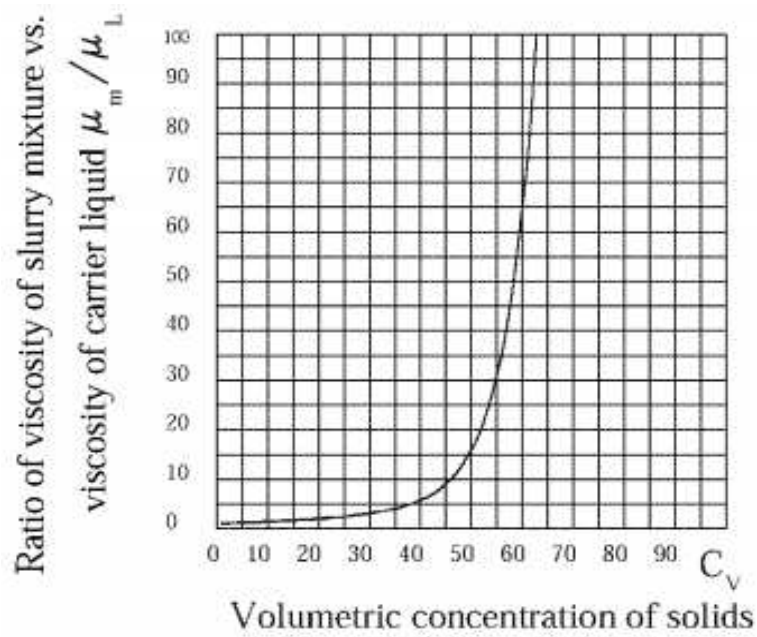


Figure 5.12 Ratio of Slurry Viscosity to Carrier Fluid Viscosity as a function of Solids Content. From [75]

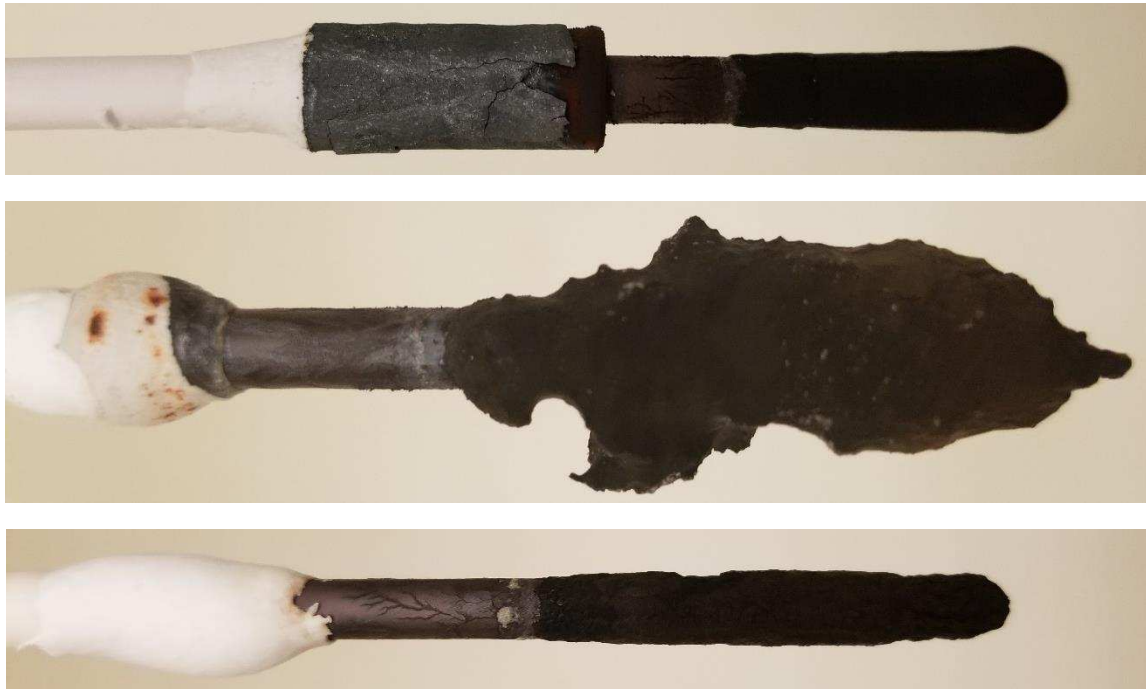


Figure 5.13 Slag Adhesion to Spindle After (from top to bottom) Tests 1, 8, and 13.

5.5.3 Leaching Results

Several compositions were prepared a second time to assess the reproducibility of the impurity extract concentrations. These data are shown in Table C.4. From there, it can be seen that almost every sample had a leach value within one part per million of its partner. The high-sodium, high-barium sample had a difference of about four parts per million.

The high arsenic concentrations leached from fast-cooled recipes 2 and 13 (22.2 and 8.7 ppm) were peculiarly high, and a plausible explanation for these outliers could not be determined. Upon repeating samples of the same composition and cooling method, the lower values (0.24 and 0.28 ppm) were produced.

CHAPTER SIX RESULTS AND DISCUSSION

Results of the investigations conducted for this study are presented in this chapter. First, representative data and calculation procedures for selected viscosity samples is given along with a discussion of observed trends with composition and temperature. Each viscosity test's recorded data can be found in APPENDIX A. After discussion of the experimental results, a temperature and composition model is presented which incorporates previous lead-smelting slag and relevant mixed-oxide melt data. Results of the density investigation are then given. Following that, a discussion of the phases that developed in the solid samples under different cooling rates is presented, culminating with a discussion of the samples' leaching behavior.

6.1 Viscosity Tests

The shear stress-shear rate (SS-SR) series plotted in Figure 6.1 is representative of the data collected for each sample. That each temperature series is a straight line is evidence that the fluid is Newtonian. As the temperature decreases, the slopes can be seen increasing. The viscosity calculated at each temperature is the regressed slope (through the origin) of that temperature's SS-SR series.

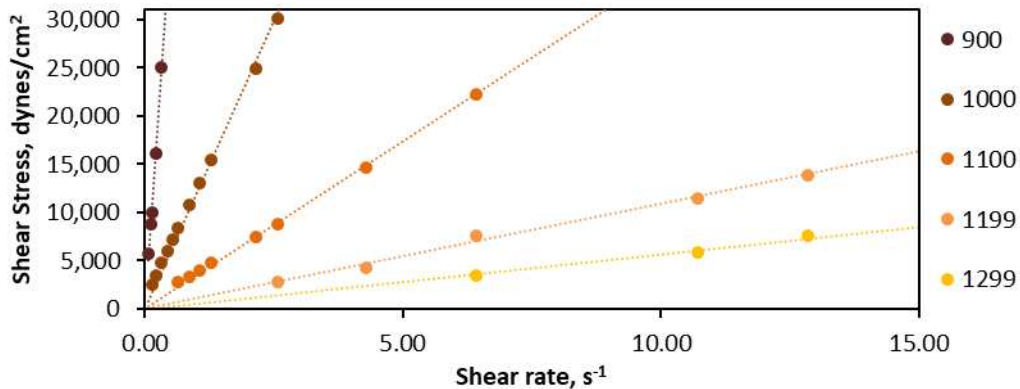


Figure 6.1 Shear Stress versus Shear Rate for Sample 1.

The logarithm of the viscosity can be plotted as a function of the inverse absolute temperature, like in Figure 6.2 for Sample 1. Doing so shows that the viscosity obeys an Arrhenius relationship; that is, it has a constant slope when $\log(\eta)$ is plotted against $1/T$.

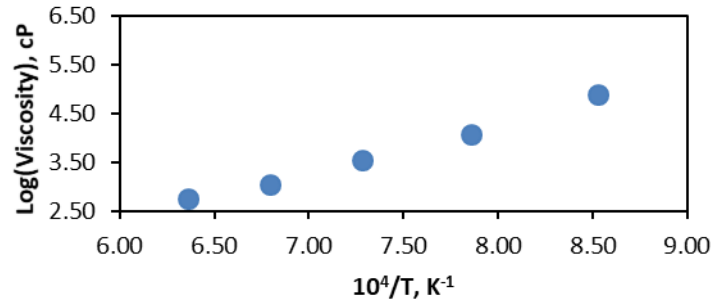


Figure 6.2 Logarithm of Viscosity as a function of inverse absolute temperature for Sample 1.

The data for every sample is plotted as $\log(\eta)$ vs $1/T$ in Figure 6.3. From this plot, three main trends are observed. One, the viscosity rises with decreasing temperature. It also rises with increasing silica content, as the weight percent silica increases in the order $5 < 2 < 13, 8, 1 < 12$. As they contain equal percentages of silica but an increasing percentage of FeO (and therefore decreasing Na_2O), samples 13, 8, and 1 also show the increase in viscosity with increasing FeO/ Na_2O content.

The trends for composition were expected. The structural backbone of the slags is their silica network. With a higher proportion of silica, the average polymer chain length is longer and thus they have a more difficult time sliding by one another. When the basic oxides (FeO and Na_2O) are incorporated into the melt, they dissociate. The oxygen anions bind with silicon, terminating the O-Si-O chain. The cations remain nearby to balance the charge. Sodium is more effective than ferrous iron at breaking the chains (and thus lowering the viscosity) because the iron remains near two oxygen atoms, while each sodium ion needs only one nearby oxygen to stabilize the charge. Sodium, therefore, does not have as strong of a cross-linking effect between the polymer chains.

After applying a least-squares fit to this data, the activation energy for viscous flow E_a can be extracted. As the Arrhenius equation can be written in a linear form (Equation 6.1), it can be seen that multiplying the slope by the constant R will produce the activation energy. Doing so for Sample 1 produced a value of 190 kJ/mol. A table of activation energy is given in Table 6.1.

$$\ln(\eta) = \left(\frac{E_a}{R}\right) \times \frac{1}{T} + A. \quad (6.1)$$

Calculating the activation energies in this manner provides an estimation of their temperature dependence, but does not account for the pre-exponential term A . For instance, the viscosities for Sample 12 were higher than those for Sample 1 even though Sample 1 has a higher temperature dependence. That is because the pre-exponential factor A for Sample 12 is considerably higher than for Sample 1.

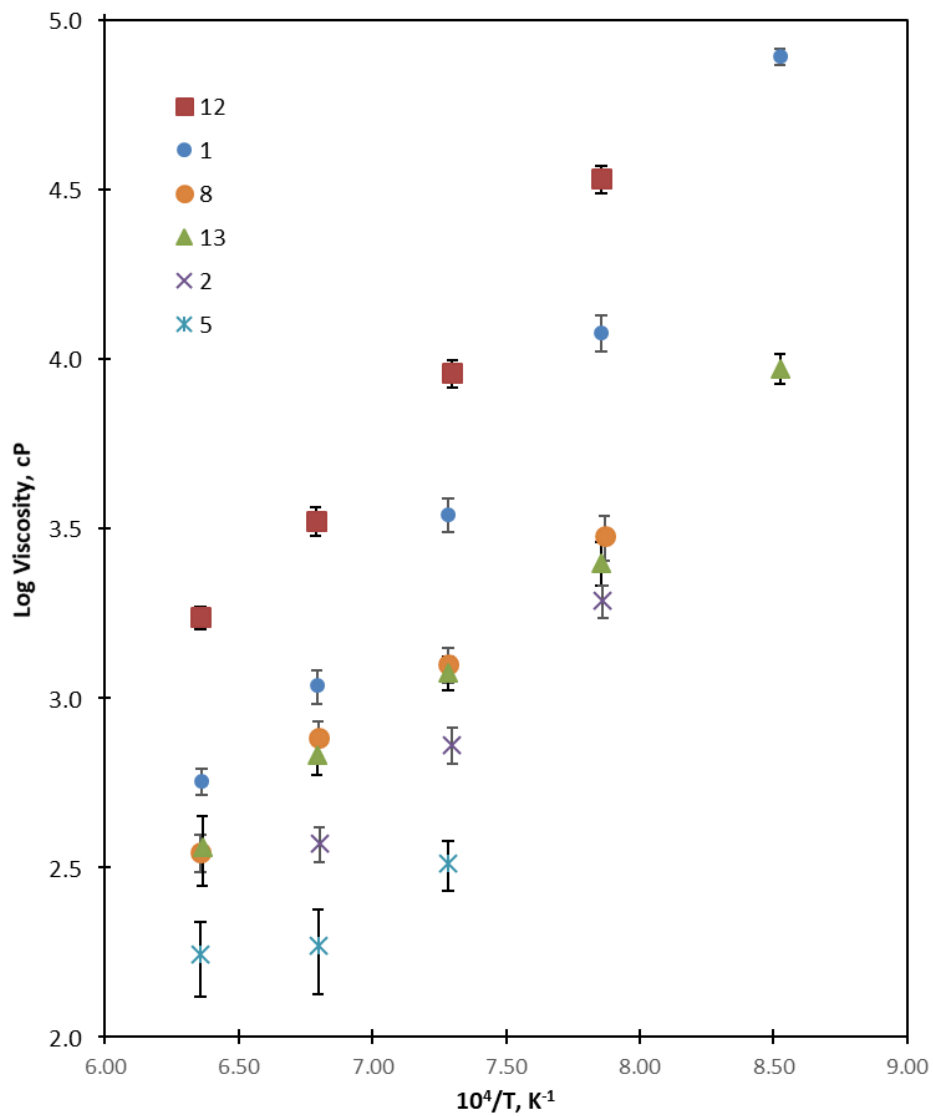


Figure 6.3 Logarithm of Viscosity as a function of inverse absolute temperature for all tests.

Table 6.1 Experimentally-Calculated Activation Energies.

Sample	Ea, kJ/mol
1	190
12	166
2	130
13	122
8	115
5	95

To comply with Zhang and Reddy’s interpretation that the pre-exponential contribution is a function of the chain formers and the temperature dependence comes from the chain breakers, the higher-silica Sample 12 should have a larger pre-exponential, while the lower-silica Sample 1 should have a higher temperature dependence. After referring to the above plot and figure, this is seen to be true.

The samples used in this investigation were simple ternary melts whose compositions were generated from normalizing the composition of a sodium-iron-silicate-based industrial slag to three components. In order to apply the viscosity data from this study to industrially-relevant systems, data sets from previous lead-smelting or sodium oxide-containing melts were gathered. Those data sources were the works of Altman *et al.*, Battle and Hager, and Zhang and Reddy on industrial lead slags; Urbain and Gupta on lead-silica melts; Dingwell and Virgo on sodium-iron(III)-silicate melts; and Shartsis and Spinner on optical glasses. These data were combined and regressed using an equation derived in a similar fashion to Zhang and Reddy’s. [36] The chain formers used in the pre-exponential are SiO₂ and Al₂O₃ and the chain modifiers in the temperature term are FeO, Fe₂O₃, Na₂O, PbO, CaO, MgO, ZnO, CuO, S, and “all other components”. These make up the A_i and B_i terms in Equation 6.2, respectively:

$$\log \eta = \left(A_0 + \sum A_i X_i \right) + \left(B_T + \sum B_i X_i \right) \times \frac{10^3}{T}. \quad (6.2)$$

The regression coefficients in Table 6.2 describe well the predicted behavior of the slags. Firstly, the inverse temperature has a strong positive effect on the viscosity (that is, the viscosity increases with decreasing temperature and vice versa). At a given temperature, as the percentage of chain-formers (SiO₂ and Al₂O₃) increases relative to the chain breakers, the viscosity will increase. An increase in chain-breaking components (FeO, Fe₂O₃, Na₂O, PbO, CaO, MgO, ZnO, CuO, and S) will decrease the dependence on temperature; or at a given temperature decrease the viscosity. Differences in the effect of the individual chain are seen with their constants being dissimilar. Particularly, different values are found for FeO and Fe₂O₃, representing their differing contributions to viscosity.

Several noteworthy trends appear in Figure 6.4. Perhaps the most obvious is that the industrial lead-smelting slags’ viscosities are 3-5 orders of magnitude lower than the optical glasses’. The sodium-iron(III)-silicate melts lie between these extremes. The calculated viscosities agree well with the measured ones over the whole range; rarely is there more than an order of magnitude difference between them. The current study’s data are highlighted in Figure 6.5. Five points stick out as having measured viscosities that are higher than their calculated values. Upon investigation, it was found that all five of these points are from Sample 1 as it decreased in temperature from 1300-900 °C. (from bottom-left to top-right).

Two observations are noted: the highest-temperature point lies about one log-unit to the right of the 1:1 line and that the distance increases as test temperature was decreased. The difference in the first point suggests some experimental error – whether it was unaccounted-for oxidation in the sample or sampling error. The second observation can be explained by referring to the relative positions of the experiments and liquidus lines – Figure 6.6. In that figure, it can be seen that the point for Sample 1 (the top-right-most in the figure) lies very close to the 1100 °C liquidus contour. Given its position, it is plausible that fayalite or wüstite began to precipitate, which would raise the apparent viscosity. This phase transformation is not considered by the regression equation, and would worsen as more solid precipitated with lower temperatures.

Table 6.2 Regression Coefficients for Equation 6.2.

Coefficient	Value
A_0	-3.847137
A_{SiO_2}	-0.035825
$A_{Al_2O_3}$	-0.063438
B_T	16.568073
B_{FeO}	-0.134941
$B_{Fe_2O_3}$	-0.11284
B_{Na_2O}	-0.180731
B_{PbO}	-0.142819
B_{CaO}	-0.151655
B_{MgO}	-0.214371
B_{ZnO}	-0.131592
B_{CuO}	-0.038266
B_S	-0.292295
B_{Others}	-0.111480
Adjusted R^2	0.9344

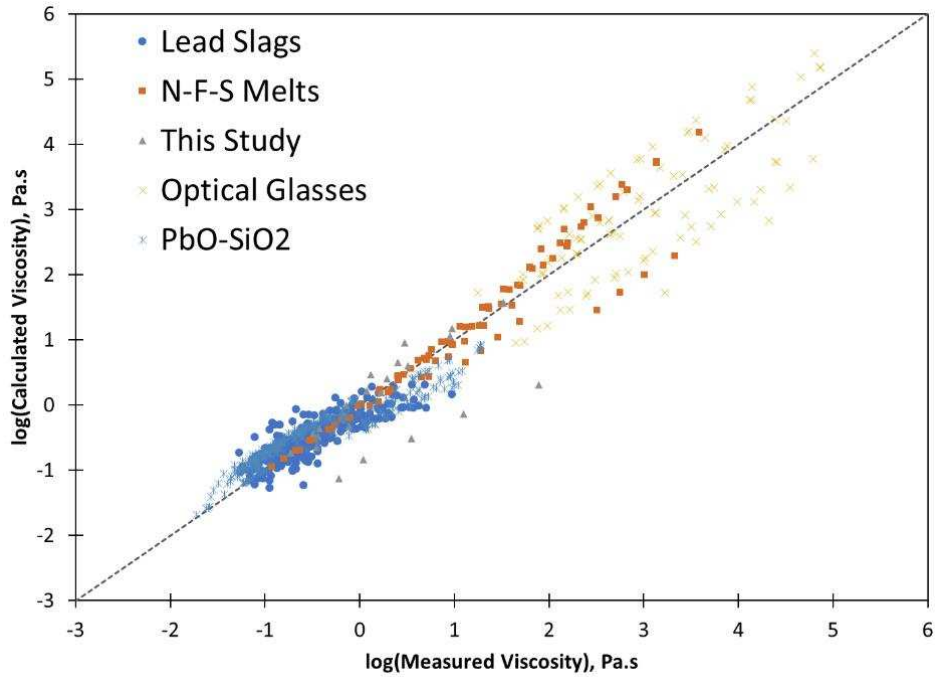


Figure 6.4 Calculated Versus Measured Viscosity.

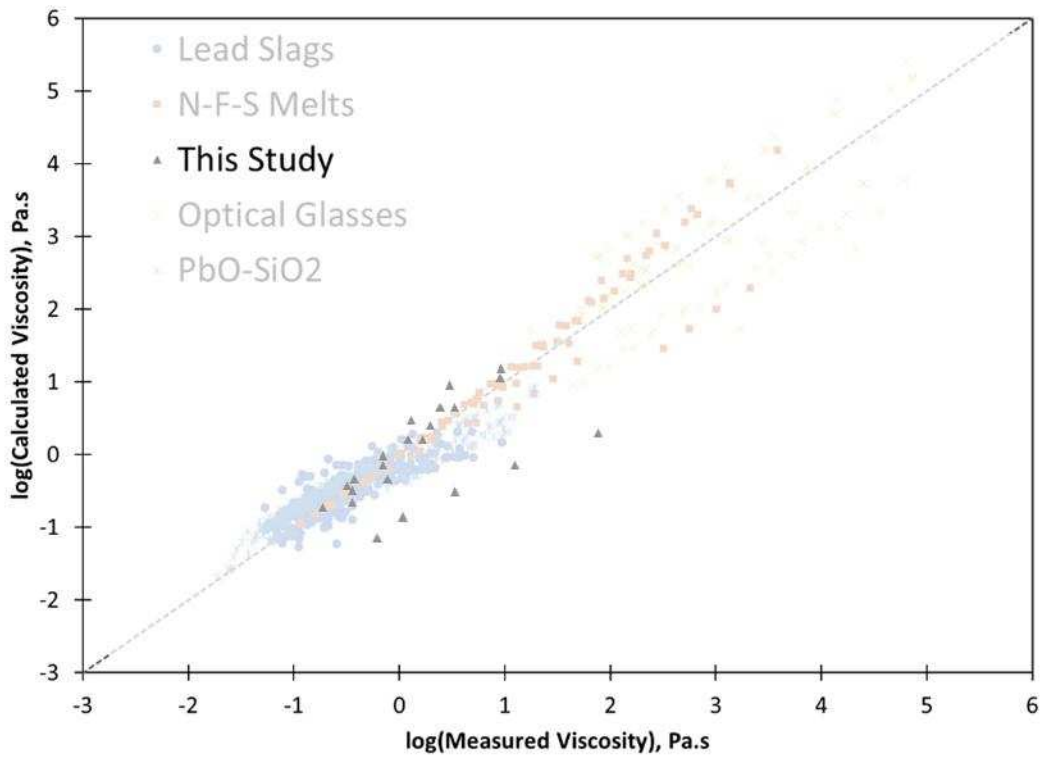


Figure 6.5 Calculated versus Measured Viscosity with Emphasis on Current Study Data.

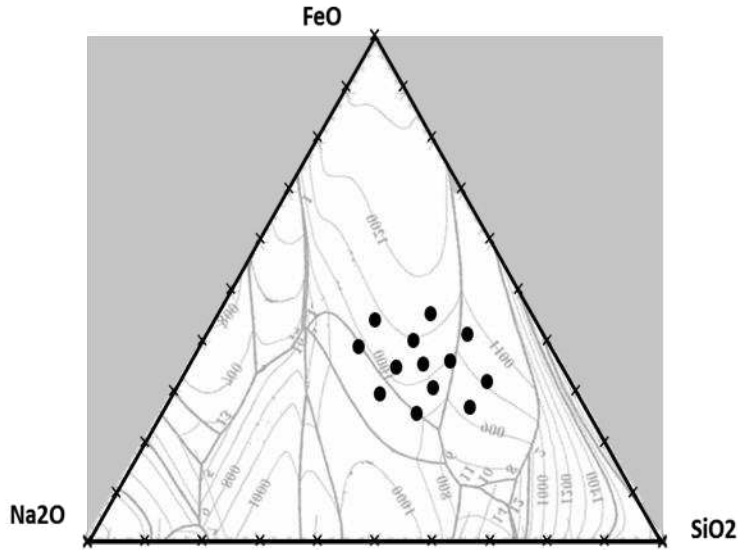


Figure 6.6 Overlay of Experimental Points and Projected Liquidus Contours.

In industrial practice, the viscosity of a melt can affect recovery by determining the amount of material entrained in the slag. Because the slag floats on the molten lead, particles of lead must travel through the slag to reach the bath below. This settling must be completed before the slag is tapped or the metal still in the slag will exit the furnace as entrained lead. Assuming a regular volume of tapped slag and hearth cross sectional area, the maximum height over which the particles must settle can be found:

$$\frac{\text{Volume of Tapped Slag}}{\text{Hearth Cross Sectional Area}} = \text{Maximum Slag Height.} \quad .3$$

The equation for the settling velocity of a solid particle was given as Equation 3.5. In this case the lead particles are liquids and as such their terminal velocities likely will be faster than those predicted below. However, their relative behavior in low- and high-viscosity slags will remain unchanged. Dividing the maximum height of the slag by the terminal velocity of the particle (Equation 6.4) results in the slag residence time for that particle:

$$\frac{\text{Slag Height (m)}}{\text{Terminal Velocity (m/s)}} = \frac{H_s}{V_t} = \text{Slag Residence Time (s)} \quad .4$$

Inserting Equation 3.5 into Equation 6.4 yields Equation 6.5:

$$\frac{H_s \times 9 \times \eta_{fluid}}{2 \times R_{particle}^2 \times (\rho_{particle} - \rho_{fluid}) \times g} = t_r. \quad .5$$

The direct influence of viscosity on the residence time can now be seen: an increase in viscosity will proportionately increase the residence time. Viscosities in this study ranged from $\approx 100\sim 50,000$ cP depending on composition and temperature. The residence times for a 50- μm lead particle settling through 0.1-meter slags of those extreme viscosities would vary from four minutes to one **day**. If the slag tapping interval is fifteen minutes, any 50- μm lead particles which enter a 100-cP slag in the last 3.79 minutes before tapping would remain entrained. The lead recovery for particles this size would be 75%. None of these lead particles would settle completely through a 50,000-cP slag. Table 6.3 shows the expected recovery after fifteen minutes for various particle size and viscosity combinations. Thus, the preference for a low slag viscosity (either through adjusting the composition or maintaining a high temperature) is demonstrated.

Table 6.3 Recovery of Lead Particles Through Slag After Fifteen Minutes.

R, μm	η, cP	10	30	100	300	1,000	3,000	10,000	30,000	100,000
	t_r, min	0.38	1.14	3.79	11	37	113	379	1,137	3,791
37		95.38	86.15	53.84	0.00	0.00	0.00	0.00	0.00	0.00
52		97.68	93.03	76.78	30.34	0.00	0.00	0.00	0.00	0.00
74		98.83	96.50	88.32	64.96	0.00	0.00	0.00	0.00	0.00
104		99.41	98.24	94.13	82.38	41.26	0.00	0.00	0.00	0.00
146		99.70	99.11	97.05	91.14	70.45	11.36	0.00	0.00	0.00
206		99.85	99.55	98.51	95.54	85.14	55.41	0.00	0.00	0.00
291		99.93	99.78	99.25	97.76	92.52	77.57	25.24	0.00	0.00
410		99.96	99.89	99.62	98.87	96.24	88.72	62.40	0.00	0.00
578		99.98	99.94	99.81	99.43	98.11	94.33	81.09	43.26	0.00
815		99.99	99.97	99.90	99.71	99.05	97.15	90.49	71.46	4.87
1149		100.00	99.99	99.95	99.86	99.52	98.56	95.21	85.64	52.15

6.2 Density Tests

Lange and Carmichael's partial molar volumes were used to predict the density of the slag systems at 1300°C (which is within their reported temperature range), and extrapolated 900 °C. Figure 6.7 shows the predicted densities of the melts over the temperature range. Within the grouping around the second line from the top, the densities increase (below about 1250 °C) with increasing sodium oxide content.

Density measurements were performed over the temperature range 900-1300 °C, but the precision of the data, and to a lesser extent the accuracy, suffered. The temperature trends predicted in Figure 6.7

are not discernable in the experimental data. As an example of the variation in the experimental data, every sample decreased in density from 1200 °C to 1100 °C, when they all should have continuously increased over the temperature range. However, the predicted trend assumes the melts remain liquid over the temperature range, which is believed to not be valid. As a theoretical verification, liquidus lines in Figure 3.25 are above 900 °C in the experimental composition range.

Not only would floating solid phases interfere with the immersion of the spindle, their presence would change the composition of the liquid phase. These solid phases could also nucleate or freeze on the spindle, respectively, when it was submerged in the melt or suspended above it. Images taken after an experimental campaign (presented in Section 0) suggest this to be an issue.

Figure 6.8 compares the predicted densities with the measured ones, with all measurements over the temperature range averaged and given a standard deviation. It can be seen that the averages for samples 1, 2, and 3 are slightly under their predicted values, but those of 5 and 6 are much lower than predicted. The predicted value for sample 4 is above the measured average, but it is still within the standard deviation.

A possible explanation for the error in the higher-density measurements is the viscous behavior of the fluids. As noted above, the higher-density samples have more silica, which would make them more viscous. As such, the spindle in these melts would take longer to reach its equilibrium position. It is possible that insufficient time was given for this position to be reached.

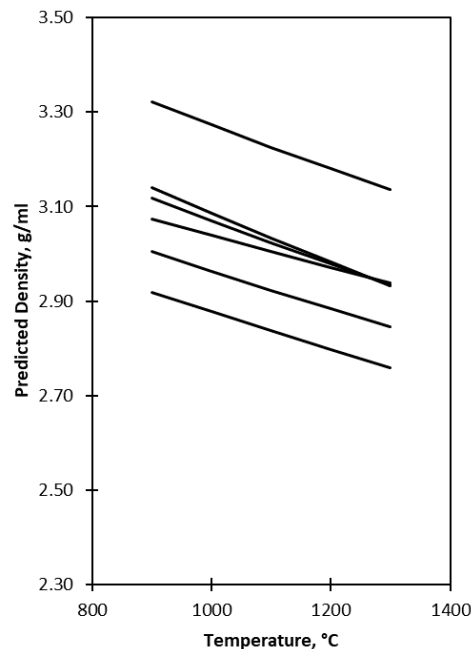


Figure 6.7 Calculated Densities using Parameters from Lange and Carmichael. [43]

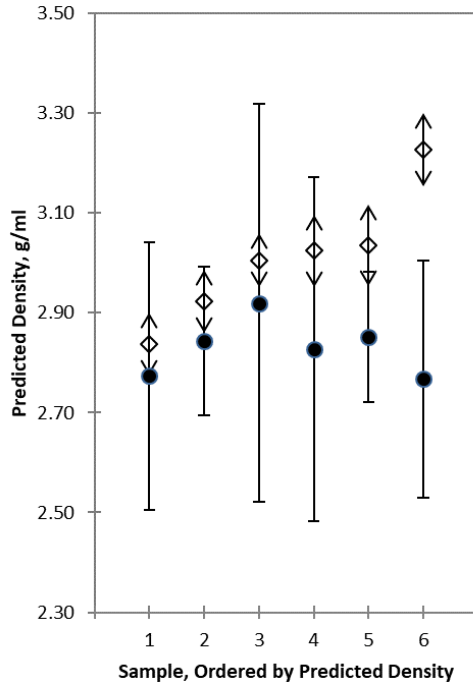


Figure 6.8 Predicted and Experimental Densities Ordered by Predicted Density.

6.3 TCLP Slag Preparation

After the TCLP slag samples had cooled, their masses and recoveries were noted. Then they were split and analyzed by ICP-MS to determine their composition. The data for the samples is given in APPENDIX C. Figure 6.9 shows the prepared slags. In the middle of the image are four fast-cooled slags. Above them are the crucibles from which they were poured. Below them are their four counterparts which had been cooled in the furnace. The four TCLP slags are described relative to their position in the experimental design space. They are referred to as “high sodium” (Slag N), “high iron” (Slag F), “high silicon” (Slag S), and “middle” (Slag M).

Mass Recoveries from samples varied from 45% to 103%. When ordered by recovery from lowest to highest, it can be seen that the sample recoveries tended to increase in the order high silica < high iron < middle < high sodium, although that does not mean that the recovery of every middle-composition slag was worse than every high sodium slag. The fast-cooled slags showed worse recoveries than their slow-cooled counterparts, because when slags poured slowly, the material which was left in the crucible was not recovered. A close-up of the pan containing each of the four recipes after having been fast-cooled is presented as Figure 6.10. There it is shown that slags S and M had generally lower recoveries.



Figure 6.9 Prepared Slags.



Figure 6.10 Poured Slags. From Left, Slags N, F, S, and M.

6.4 Phase Analysis

Several techniques were used to predict and identify major phases present in the samples, as well as determine whether the impurities (barium, lead, and arsenic) segregated into their own phases or remained distributed among the major phases.

6.4.1 Satmagan Analysis

Pulverized samples from eight TCLP slags were used to determine the magnetic content (assumed to be only magnetite) of those TCLP samples. The magnetite content according to the Satmagan was then used as a basis to estimate the $\text{Fe}^{3+}/\Sigma\text{Fe}$ ratio for the samples. The assumption in making the recipes was that all iron would react to form FeO and stay as Fe^{2+} , but partial oxidation was known to be possible, although argon was introduced to limit its extent.

Table 6.4 Magnetite Content from Satmagan Analysis.

Sample	Magnetite, wt %		
	<i>Cooling Rate</i>	<i>Fast</i>	<i>Slow</i>
S		1.99	7.31
F		20.59	23.18
N		2.65	0.66
M		0.00	0.00

The only sample with significant magnetite content was the high-iron sample (F, above), which returned 21% for the fast-cooled sample and 23% for the slow-cooled sample. A magnetite content of approximately 20% in the high iron was produced by HSC when the input $\text{Fe}^{3+}/\Sigma\text{Fe}$ ratio was set to 0.167, which would be akin to one ferric ion for every five ferrous ions.

6.4.2 Predicted Equilibrium Phases

Outotec's HSC software was used to predict the solid phases that would develop under equilibrium conditions. The results for 1200 °C are given in Table 6.5 and for 700 °C in

Table 6.6. The phases were mostly composed of sodium silicates (Na_2SiO_3 and $\text{Na}_2\text{Si}_2\text{O}_5$) and iron oxides (FeO and Fe_3O_4) – these phases comprised 50 – 70% of all samples.

When barium was added, it was predicted to form BaSi₂O₅, BaSiO₃, Ba₂SiO₄, and Ba₂Si₃O₈. Lead was predicted to form PbSiO₃ in the high-silica sample, but remain as elemental lead in the other samples (or gaseous lead at 1200 °C). Adding arsenic to the samples was predicted to form Na₃AsO₄ and various arsenic gases.

Table 6.5 Phase Distribution (wt%) According to HSC at 1200 °C.

	No Impurity				Barium				Lead				Arsenic			
	S	F	N	M	S	F	N	M	S	F	N	M	S	F	N	M
Na ₂ SiO ₃	8.19	18.04	47.52	27.56	8.51	18.98	41.93	28.71	7.56	16.75	45.02	25.78	7.23	15.83	46.63	24.02
FeO	19.38	29.90	26.29	25.28	18.85	29.49	24.08	24.71	16.12	25.16	21.99	20.64	13.61	20.31	30.28	17.41
Na ₂ O*2SiO ₂	27.17	20.56	0.15	24.46	24.88	16.81	0.08	19.47	25.82	20.08	0.13	23.83	25.69	20.83	0.81	24.66
Fe ₃ O ₄	6.80	11.68	11.91	9.14	6.67	11.29	11.40	8.83	9.44	14.95	13.43	12.34	12.32	20.31	8.57	15.45
*2FeO*SiO ₂	11.32	9.84	0.02	5.64	10.07	7.71	0.01	4.26	8.64	7.96	0.02	4.28	6.55	5.99	0.15	3.49
SiO ₂	22.50	7.28	0.02	5.49	18.60	5.46	0.01	4.06	21.61	7.04	0.02	5.24	22.02	7.35	0.11	5.64
NaFe(SiO ₃) ₂	2.95	0.90	0.00	0.73	2.42	0.62	0.00	0.48	3.69	1.11	0.00	0.92	4.72	1.57	0.00	1.24
FeNaO ₂	0.07	0.18	5.88	0.23	0.07	0.20	6.79	0.27	0.08	0.20	6.50	0.27	0.09	0.23	1.95	0.30
Fe ₂ O ₃	1.38	1.44	1.65	1.29	1.30	1.37	1.63	1.24	2.14	2.02	2.06	1.96	3.25	3.23	1.05	2.82
*2Na ₂ O*SiO ₂	0.00	0.00	4.40	0.01	0.00	0.00	5.50	0.01	0.00	0.00	4.40	0.00	0.00	0.00	0.74	0.00
BaSi ₂ O ₅	0.00	0.00	0.00	0.00	6.72	4.46	0.01	3.91	0.00	0.00	0.00	0.00	0.00	0.00	0.00	0.00
Na ₃ AsO ₄	0.00	0.00	0.00	0.00	0.00	0.00	0.00	0.00	0.00	0.00	0.00	0.00	0.17	0.36	7.63	1.31
Pb(g)	0.00	0.00	0.00	0.00	0.00	0.00	0.00	0.00	4.18	4.48	4.50	4.47	0.00	0.00	0.00	0.00
Pb	0.00	0.00	0.00	0.00	0.00	0.00	0.00	0.00	0.00	0.00	0.00	0.00	0.00	0.00	0.00	0.00
BaSiO ₃	0.00	0.00	0.00	0.00	1.28	2.80	1.49	3.20	0.00	0.00	0.00	0.00	0.00	0.00	0.00	0.00
As ₂ (g)	0.00	0.00	0.00	0.00	0.00	0.00	0.00	0.00	0.00	0.00	0.00	0.00	1.34	2.33	0.84	1.93
Ba ₂ SiO ₄	0.00	0.00	0.00	0.00	0.00	0.04	4.58	0.06	0.00	0.00	0.00	0.00	0.00	0.00	0.00	0.00
Na(g)	0.02	0.06	1.64	0.08	0.02	0.08	1.85	0.10	0.01	0.05	1.31	0.06	0.01	0.03	0.97	0.04
As ₄ (g)	0.00	0.00	0.00	0.00	0.00	0.00	0.00	0.00	0.00	0.00	0.00	0.00	0.00	0.00	0.00	0.00
AsO(g)	0.00	0.00	0.00	0.00	0.00	0.00	0.00	0.00	0.00	0.00	0.00	0.00	2.82	1.50	0.15	1.59
*3Na ₂ O*2SiO ₂	0.00	0.00	0.52	0.00	0.00	0.00	0.60	0.00	0.00	0.00	0.53	0.00	0.00	0.00	0.08	0.00
Ba ₂ Si ₃ O ₈	0.00	0.00	0.00	0.00	0.41	0.61	0.00	0.63	0.00	0.00	0.00	0.00	0.00	0.00	0.00	0.00
PbSiO ₃	0.00	0.00	0.00	0.00	0.00	0.00	0.00	0.00	0.33	0.04	0.00	0.04	0.00	0.00	0.00	0.00
FeO*SiO ₂	0.23	0.12	0.00	0.08	0.19	0.09	0.00	0.06	0.19	0.11	0.00	0.07	0.17	0.09	0.00	0.06
PbO	0.00	0.00	0.00	0.00	0.00	0.00	0.00	0.00	0.10	0.04	0.05	0.05	0.00	0.00	0.00	0.00
PbO(g)	0.00	0.00	0.00	0.00	0.00	0.00	0.00	0.00	0.08	0.03	0.04	0.04	0.00	0.00	0.00	0.00
Pb ₂ SiO ₄	0.00	0.00	0.00	0.00	0.00	0.00	0.00	0.00	0.00	0.00	0.00	0.00	0.00	0.00	0.00	0.00
Fe	0.00	0.00	0.00	0.00	0.00	0.00	0.00	0.00	0.00	0.00	0.00	0.00	0.00	0.00	0.00	0.00
As(g)	0.00	0.00	0.00	0.00	0.00	0.00	0.00	0.00	0.00	0.00	0.00	0.00	0.02	0.03	0.02	0.02
BaO	0.00	0.00	0.00	0.00	0.00	0.00	0.03	0.00	0.00	0.00	0.00	0.00	0.00	0.00	0.00	0.00
As ₃ (g)	0.00	0.00	0.00	0.00	0.00	0.00	0.00	0.00	0.00	0.00	0.00	0.00	0.00	0.00	0.00	0.00
*3Na ₂ O*As ₂ O ₅	0.00	0.00	0.00	0.00	0.00	0.00	0.00	0.00	0.00	0.00	0.00	0.00	0.00	0.00	0.02	0.00

Table 6.6 Phase Distribution (wt%) According to HSC at 700 °C.

	No Impurity				Barium				Lead				Arsenic			
	S	F	N	M	S	F	N	M	S	F	N	M	S	F	N	M
Na2SiO3	14.28	25.20	45.47	35.78	14.48	25.39	39.31	35.85	13.23	23.49	44.61	33.52	11.24	21.69	47.60	30.80
FeO	13.90	23.00	34.41	20.08	13.70	23.57	32.87	20.42	12.33	19.69	28.45	16.86	8.73	14.71	35.96	12.93
Na2O*2SiO2	14.78	8.94	0.00	11.41	13.16	6.84	0.00	8.56	13.57	8.76	0.00	11.10	12.16	9.29	0.00	11.68
Fe3O4	3.46	10.32	2.32	7.76	3.80	10.40	1.69	7.92	4.94	13.20	4.68	10.56	10.01	20.20	2.29	15.20
*2FeO*SiO2	20.77	20.57	0.00	14.03	18.83	16.89	0.00	11.21	17.22	17.02	0.00	11.05	9.62	11.55	0.01	7.78
SiO2	20.48	6.66	0.00	6.01	16.89	4.90	0.00	4.36	19.08	6.51	0.00	5.79	19.04	7.06	0.00	6.35
NaFe(SiO3)2	11.57	4.03	0.00	3.81	9.80	2.61	0.00	2.43	13.51	4.94	0.00	4.78	22.17	8.13	0.00	7.53
FeNaO2	0.03	0.10	9.15	0.12	0.04	0.11	9.26	0.13	0.04	0.11	11.20	0.14	0.06	0.14	3.56	0.17
Fe2O3	0.66	1.14	0.20	0.98	0.70	1.08	0.14	0.95	1.01	1.58	0.44	1.48	2.72	3.05	0.18	2.65
*2Na2O*SiO2	0.00	0.00	8.21	0.00	0.00	0.00	10.47	0.00	0.00	0.00	5.76	0.00	0.00	0.00	1.41	0.00
BaSi2O5	0.00	0.00	0.00	0.00	7.31	5.40	0.00	5.19	0.00	0.00	0.00	0.00	0.00	0.00	0.00	0.00
Na3AsO4	0.00	0.00	0.00	0.00	0.00	0.00	0.00	0.00	0.00	0.00	0.00	0.00	0.71	0.66	8.12	1.80
Pb(g)	0.00	0.00	0.00	0.00	0.00	0.00	0.00	0.00	0.20	0.20	0.19	0.20	0.00	0.00	0.00	0.00
Pb	0.00	0.00	0.00	0.00	0.00	0.00	0.00	0.00	2.89	3.96	4.36	3.88	0.00	0.00	0.00	0.00
BaSiO3	0.00	0.00	0.00	0.00	0.69	1.72	0.47	1.87	0.00	0.00	0.00	0.00	0.00	0.00	0.00	0.00
As2(g)	0.00	0.00	0.00	0.00	0.00	0.00	0.00	0.00	0.00	0.00	0.00	0.00	0.99	0.99	0.40	0.93
Ba2SiO4	0.00	0.00	0.00	0.00	0.00	0.00	5.50	0.00	0.00	0.00	0.00	0.00	0.00	0.00	0.00	0.00
Na(g)	0.00	0.00	0.00	0.00	0.00	0.00	0.00	0.00	0.00	0.00	0.00	0.00	0.00	0.00	0.00	0.00
As4(g)	0.00	0.00	0.00	0.00	0.00	0.00	0.00	0.00	0.00	0.00	0.00	0.00	2.49	2.49	0.41	2.16
AsO(g)	0.00	0.00	0.00	0.00	0.00	0.00	0.00	0.00	0.00	0.00	0.00	0.00	0.00	0.00	0.00	0.00
*3Na2O*2SiO2	0.00	0.00	0.25	0.00	0.00	0.00	0.28	0.00	0.00	0.00	0.18	0.00	0.00	0.00	0.04	0.00
Ba2Si3O8	0.00	0.00	0.00	0.00	0.55	1.04	0.00	1.08	0.00	0.00	0.00	0.00	0.00	0.00	0.00	0.00
PbSiO3	0.00	0.00	0.00	0.00	0.00	0.00	0.00	0.00	1.43	0.28	0.00	0.32	0.00	0.00	0.00	0.00
FeO*SiO2	0.05	0.03	0.00	0.02	0.05	0.02	0.00	0.02	0.05	0.03	0.00	0.02	0.04	0.02	0.00	0.02
PbO	0.00	0.00	0.00	0.00	0.00	0.00	0.00	0.00	0.41	0.22	0.04	0.28	0.00	0.00	0.00	0.00
PbO(g)	0.00	0.00	0.00	0.00	0.00	0.00	0.00	0.00	0.00	0.00	0.00	0.00	0.00	0.00	0.00	0.00
Ph2SiO4	0.00	0.00	0.00	0.00	0.00	0.00	0.00	0.00	0.10	0.01	0.00	0.02	0.00	0.00	0.00	0.00
Fe	0.00	0.00	0.00	0.00	0.00	0.00	0.00	0.00	0.00	0.01	0.09	0.01	0.00	0.00	0.00	0.00
As(g)	0.00	0.00	0.00	0.00	0.00	0.00	0.00	0.00	0.00	0.00	0.00	0.00	0.00	0.00	0.00	0.00
BaO	0.00	0.00	0.00	0.00	0.00	0.00	0.00	0.00	0.00	0.00	0.00	0.00	0.00	0.00	0.00	0.00
As3(g)	0.00	0.00	0.00	0.00	0.00	0.00	0.00	0.00	0.00	0.00	0.00	0.00	0.00	0.00	0.00	0.00
*3Na2O*As2O5	0.00	0.00	0.00	0.00	0.00	0.00	0.00	0.00	0.00	0.00	0.00	0.00	0.00	0.00	0.00	0.00

The underlying assumptions of this phase analysis deserve scrutiny. For one, the modeled conditions were not necessarily reflected in the tests. 1200 °C was chosen to represent the phases that would exist in the fast-cooled samples, but most of the samples were primarily liquid at that temperature. Also, in cooling quickly, the samples vitrified – instead of crystallized – so these phases were not present.

The phases predicted at 700 °C are likely more representative, as the cooling rate was lower – which gave diffusion the opportunity to occur and allowed the predicted phases to segregate.

6.4.3 Spectroscopic Analysis

The degree of crystallinity in the samples was investigated with XRD. Very few crystalline phases were observed, and the majority of those were iron oxides. The high silica sample (Figure 6.11) and middle composition (Figure 6.14) showed broad amorphous regions. The best-defined peaks were the iron oxide peaks in the high iron sample (Figure 6.12) and the sodium silicate peaks in the high sodium sample (Figure 6.13). The “Score” listed in the figures below is the value (out of 100) that the software’s Search Match function assigned to the reference peak being present in the unknown spectrum.

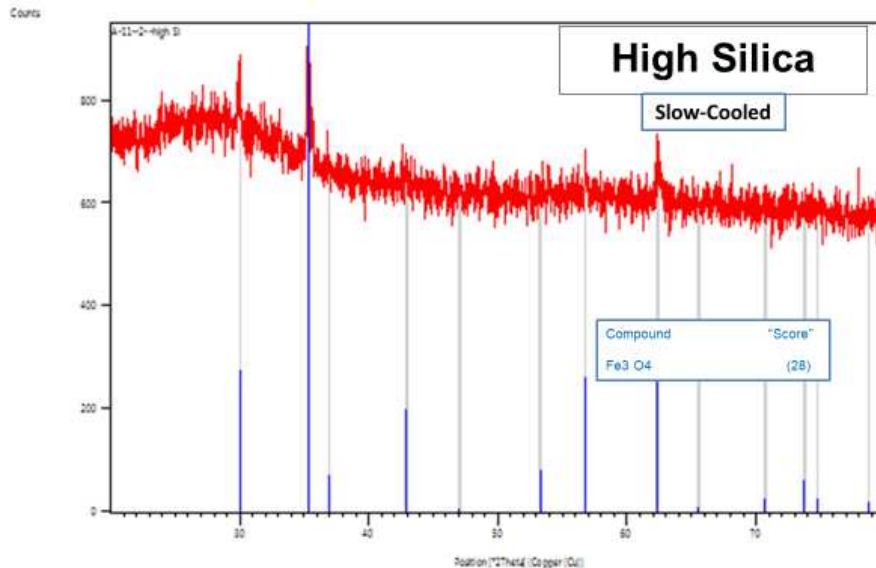


Figure 6.11 XRD Pattern for a Slow-Cooled, High-Silica Sample.

The appearance of iron oxide peaks in the slow-cooled high-iron sample was expected due to its composition lying in the iron oxide (wüstite or Fe₂O₃) primary phase region.



Figure 6.12 XRD Pattern for a Slow-Cooled, High-Iron Sample.

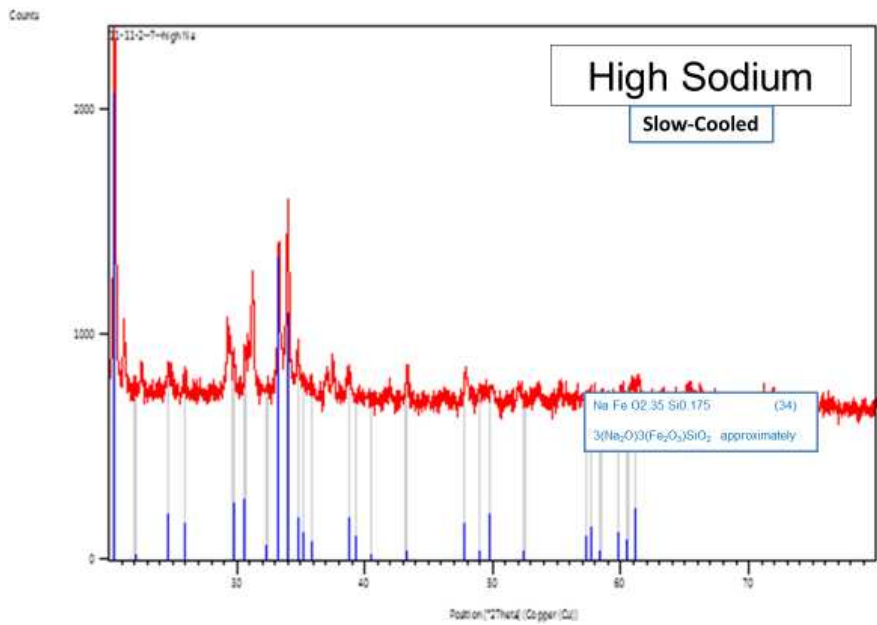


Figure 6.13 XRD Pattern for a Slow-Cooled, High-Sodium Sample.

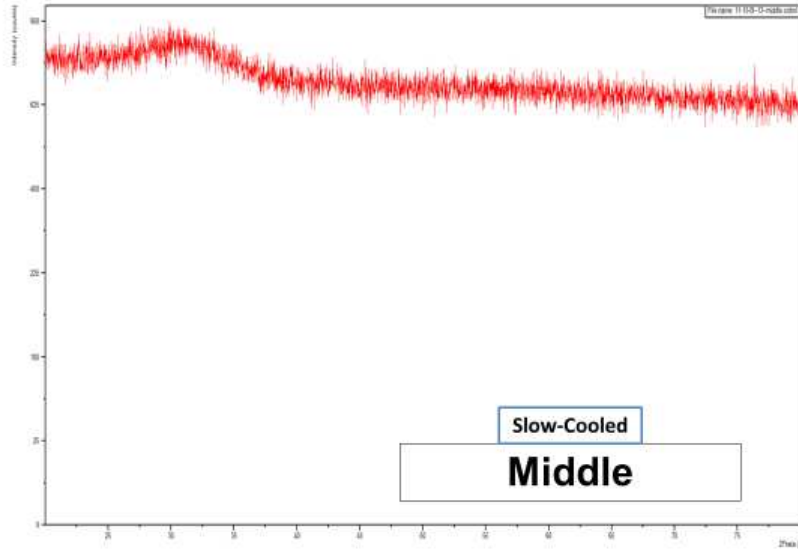


Figure 6.14 XRD Pattern for a Slow-Cooled, Middle-Composition Sample.

A similar trend occurred with the fast-cooled samples. The high-silica sample had the most-pronounced amorphous region (Figure 6.15). Again, iron oxides were detected in the high-iron sample (Figure 6.16) and sodium silicates in the high-sodium sample (Figure 6.17). The middle composition showed a large amorphous curve and a peak (Figure 6.18), but the software was unable to identify a compound from the lone peak against the background.

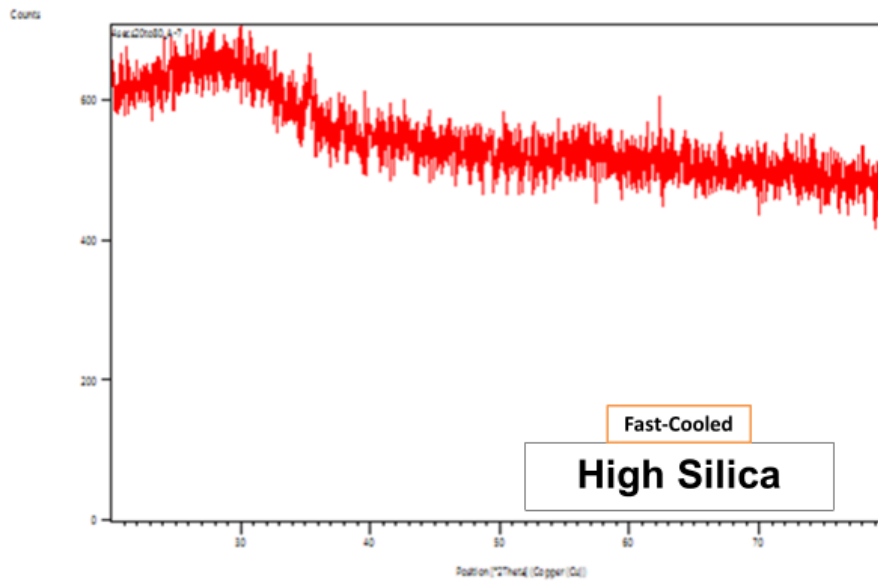


Figure 6.15 XRD Pattern for a Fast-Cooled, High-Silica Sample.

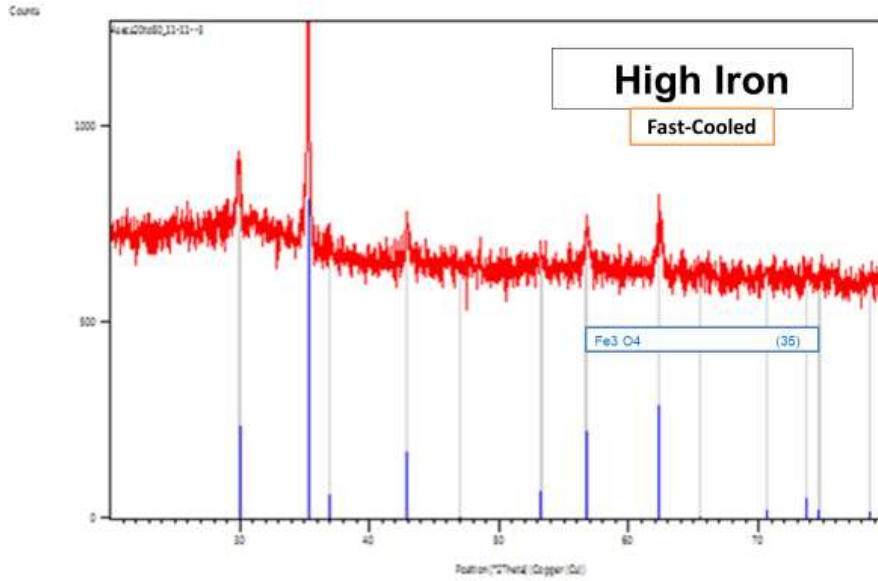


Figure 6.16 XRD Pattern for a Fast-Cooled, High-Iron Sample.

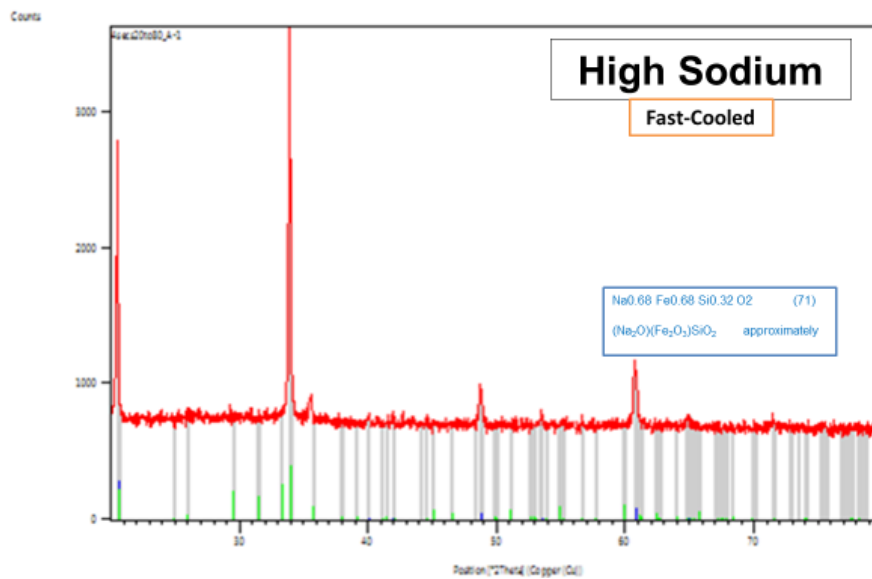


Figure 6.17 XRD Pattern for a Fast-Cooled, High-Sodium Sample.

The distinct peaks were identified as being a sodium-iron-silicate, approximately corresponding to a composition of Na₂O•Fe₂O₃•SiO₂. According to Figure 3.25, the primary phase for this composition, if fully reduced, would be Na₂FeSiO₄. Satmagan results show there is some oxidation of the sample, so the formation of a more-oxidized compound is expected – even if it was not the primary phase (Figure 3.27).

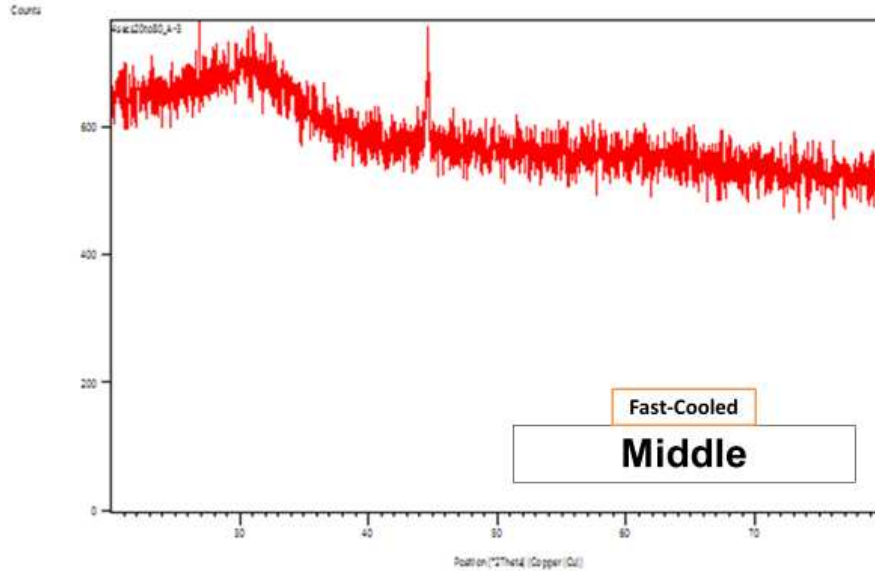


Figure 6.18 XRD Pattern for a Fast-Cooled, Middle-Composition Sample.

Based on the relatively high crystallinity of the slow-cooled high sodium sample, EDS Maps at 1000X magnification were created for the high-sodium sample containing each impurity to see into which phases the impurities congregated. In these images, colored pixels represent locations where a signal from the specified element originated from. Thus, by comparing where the colors in the images overlap (or not), it can be determined which elements are associated with which other elements. Several broad trends appeared: the sodium was not associated with iron, sodium was generally associated with silicon, and iron was not generally associated with silicon.

The behavior of each impurity was unique. Barium was seen (Figure 6.19) to form a phase with silicon, and to a lesser extent, sodium. The barium was not associated with iron. These associations lend more support to the hypothesis of barium forming a barium silicate or barium-sodium-silicate as predicted by Figure 3.28. The lead was associated with silicon, as shown in Figure 6.20. While the barium was associated with silicon and partially associated with sodium, the arsenic appears in Figure 6.21 to be associated more with sodium and significantly less with silicon or iron. This is expected from the HSC prediction of the formation of sodium arsenates.

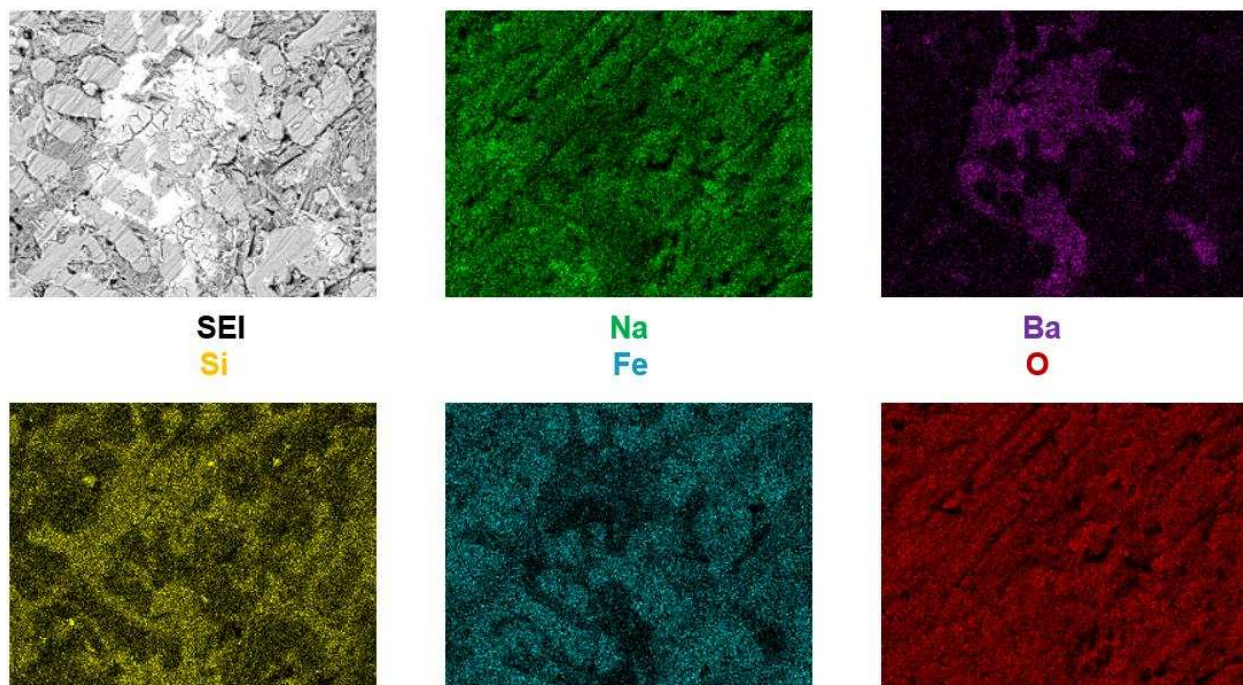


Figure 6.19 EDS Maps for Slow-Cooled High-Sodium Sample Doped with 8.84 wt% Barium Oxide.

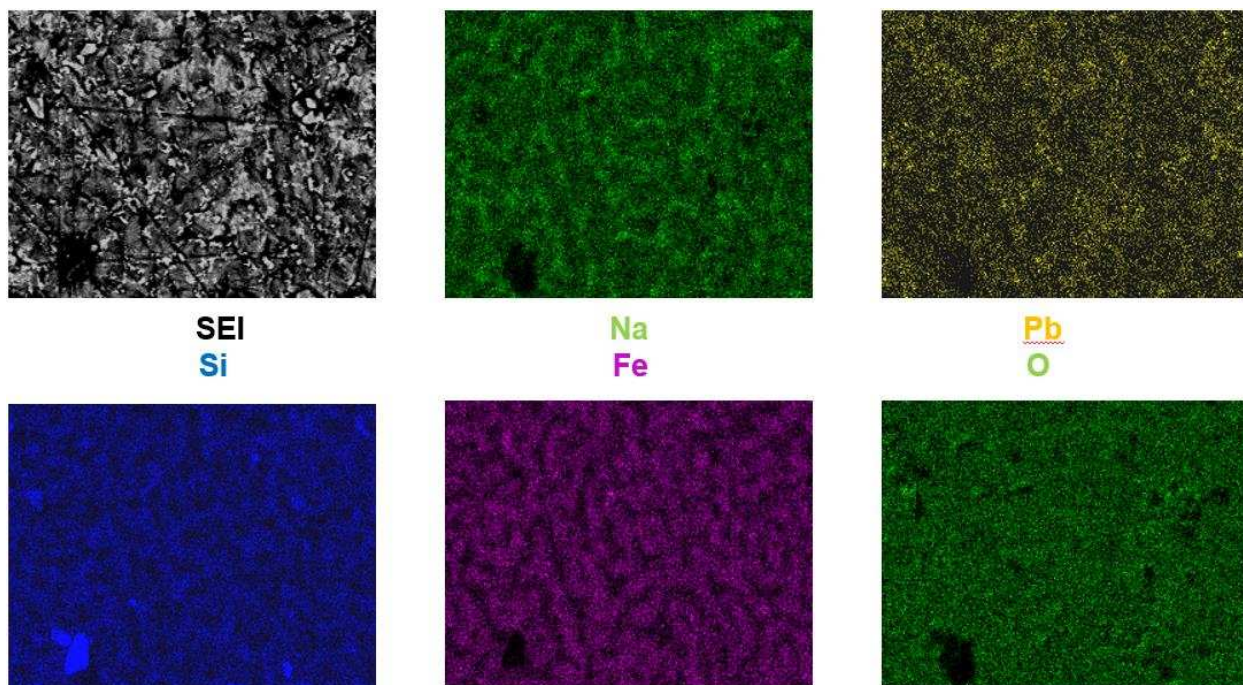


Figure 6.20 EDS Maps for Slow-Cooled High-Sodium Sample Doped with 5 wt% Lead Oxide.

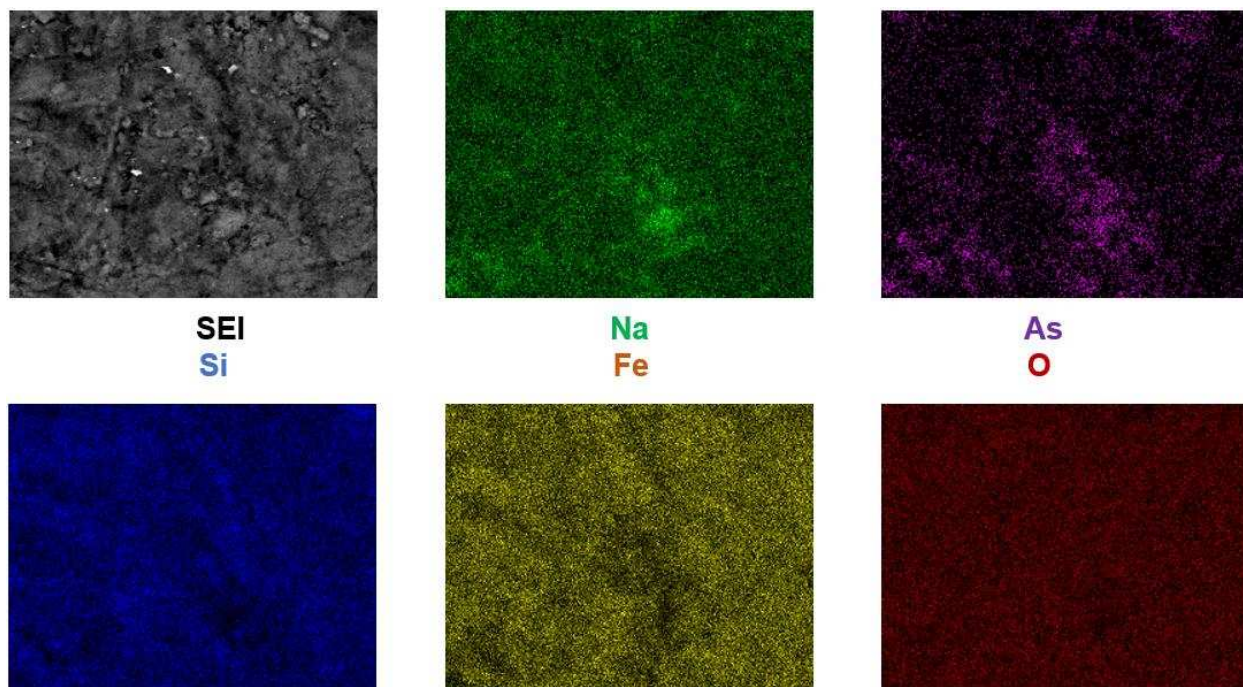


Figure 6.21 EDS Maps for Slow-Cooled High-Sodium Sample Doped with 5 wt% Arsenic Trioxide.

Samples were also imaged before and after leaching in acetic acid. Figure 6.22 shows a secondary electron image of a slow-cooled high-sodium sample doped with barium before and after leaching. In the before image, a flat surface (below some surface imperfections) can be seen. Afterwards, however, small islands appear, with the space between them recessed. Upon comparison with the EDS maps, these islands are revealed to be iron oxides.

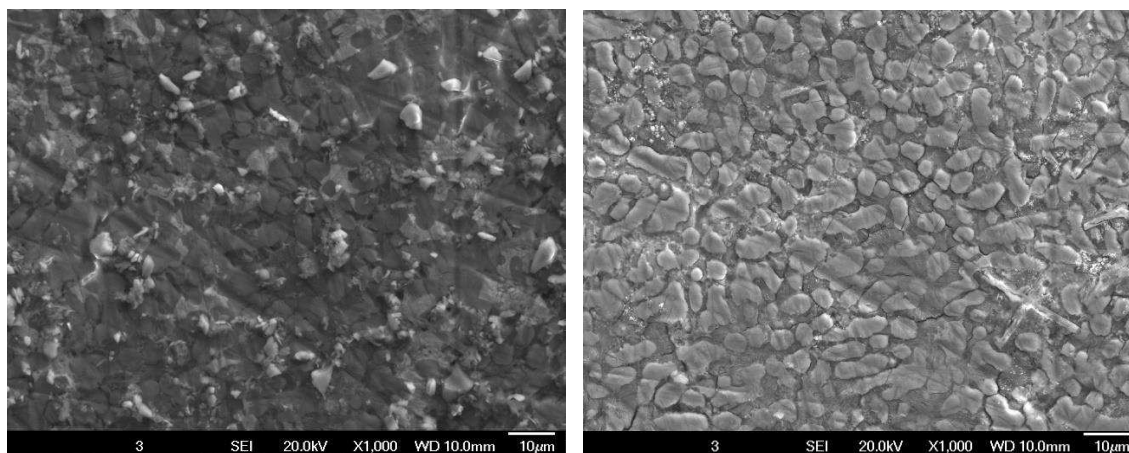


Figure 6.22 Secondary Electron Image of Barium-Doped High-Sodium Sample before (left) and after (right) Leaching.

Barium EDS maps at 1000X were taken at the same spot before and after leaching and are shown in Figure 6.23. There are several regions which are not present in the after image (upper left, across the lower third, and towards the top of the right side). Images of a fast-cooled high-silica sample did not show phase segregation or any difference on leaching: Figure 6.24 shows this for the case of barium. Thus, the difference between the two samples is apparent: given a slow cooling rate and enough sodium, barium will form a soluble silicate phase, whereas a fast cooling rate and more silicon will prevent formation of a soluble phase.

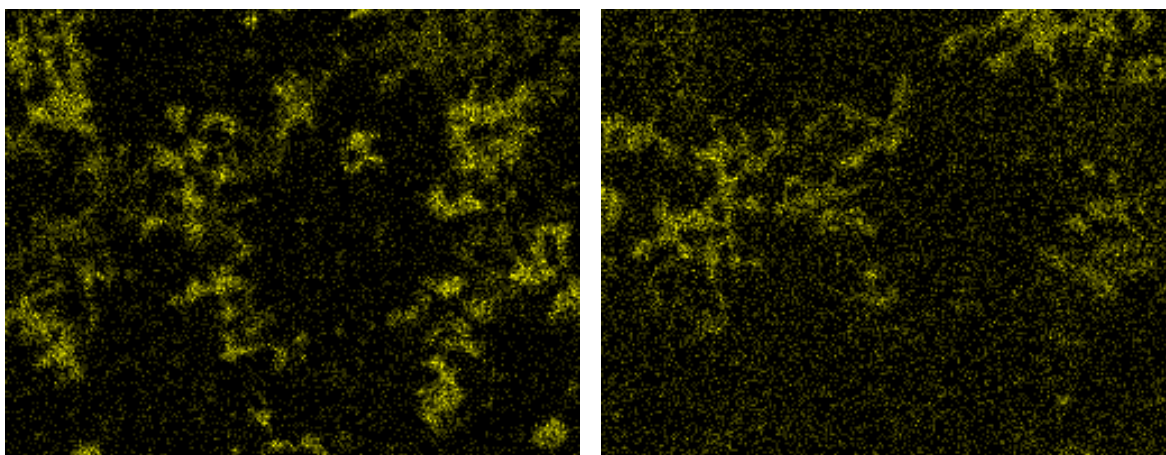


Figure 6.23 Barium EDS Map of Barium-Doped High-Sodium Sample before (left) and after (right) Leaching.

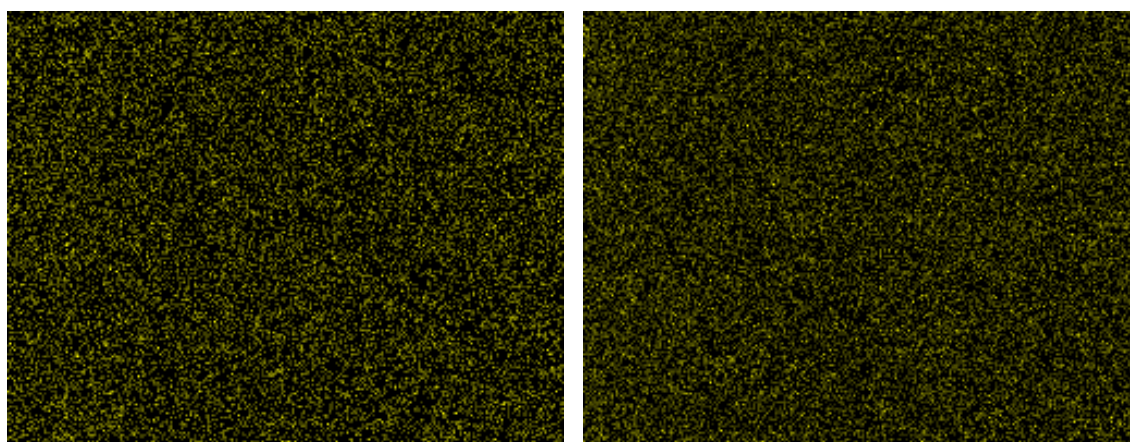


Figure 6.24 Barium EDS Map of Barium-Doped High-Silica Sample before (left) and after (right) Leaching.

6.5 TCLP Leach Tests

The TCLP leach was conducted by an off-site laboratory familiar with the procedure for industrial slag samples. For each of the three impurity elements (barium, lead, and arsenic), graphs of extract impurity concentration in parts per million are presented. A phase diagram which correlates the samples' locations in ternary space with their leached amounts is also presented.

Most of the samples leached amounts under the EPA regulatory limit. For barium, that mark is 100 ppm. All but one of the samples in this study reported a concentration under that limit, but the sample which exceeded the limit (Slag N, slow-cooled, 8.84 wt% BaO) returned a concentration more than four times the limit at 406 ppm. Five parts per million is the maximum allowable extract concentration for lead and arsenic. Samples N and M exceeded the limit for lead and arsenic.

From the EDS maps in Figure 6.19, it was seen that the barium forms a sodium-barium-silicate, as predicted by Figure 3.28. Given that sodium silicates are soluble and barium regions disappeared after leaching (Figure 6.23), it seems likely that the sodium-barium-silicates also solubilized.

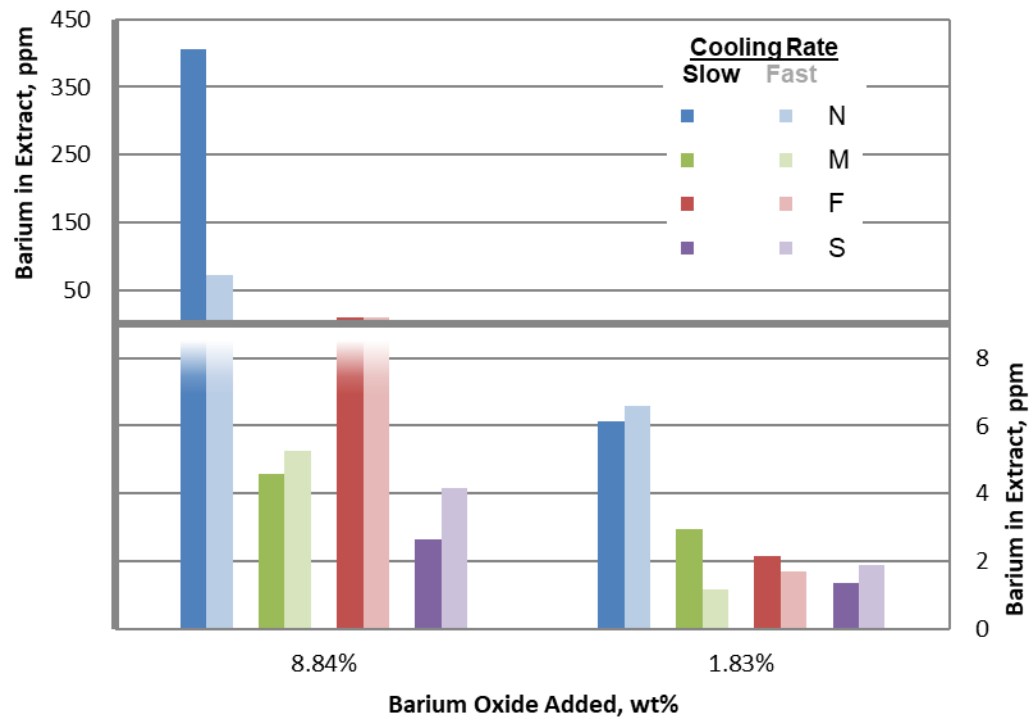


Figure 6.25 TCLP Leach Results for Barium.

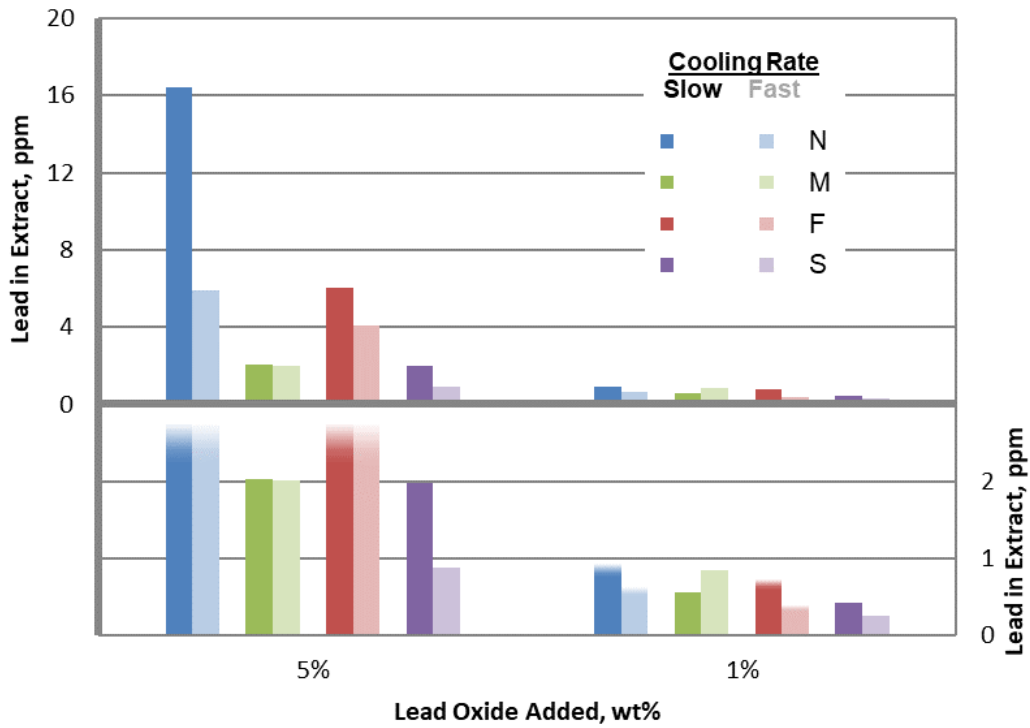


Figure 6.26 TCLP Leach Results for Lead.

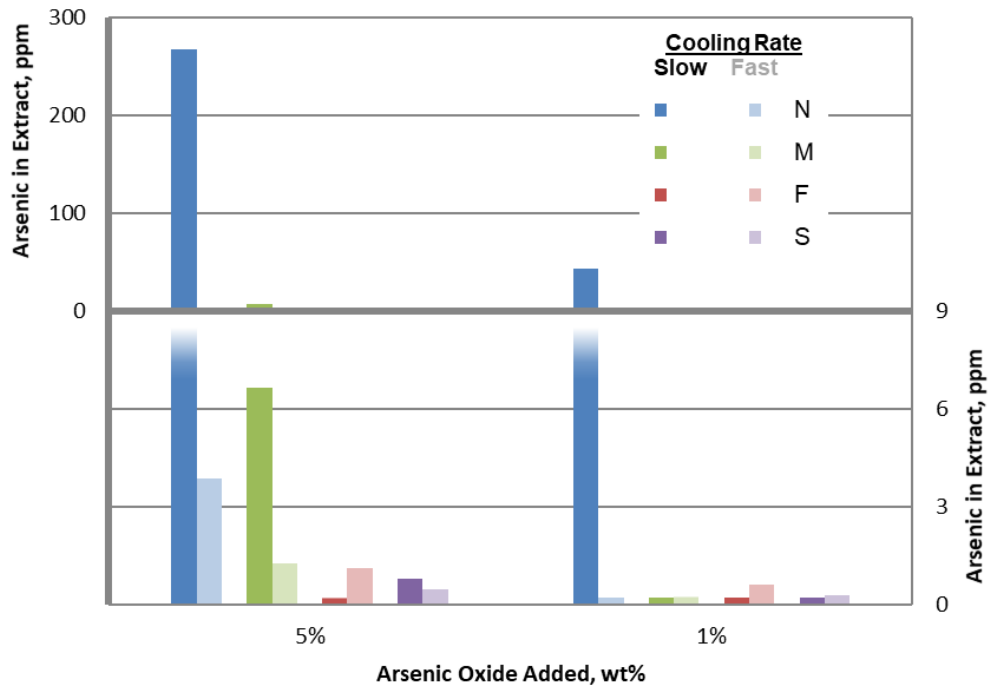


Figure 6.27 TCLP Leach Results for Arsenic.

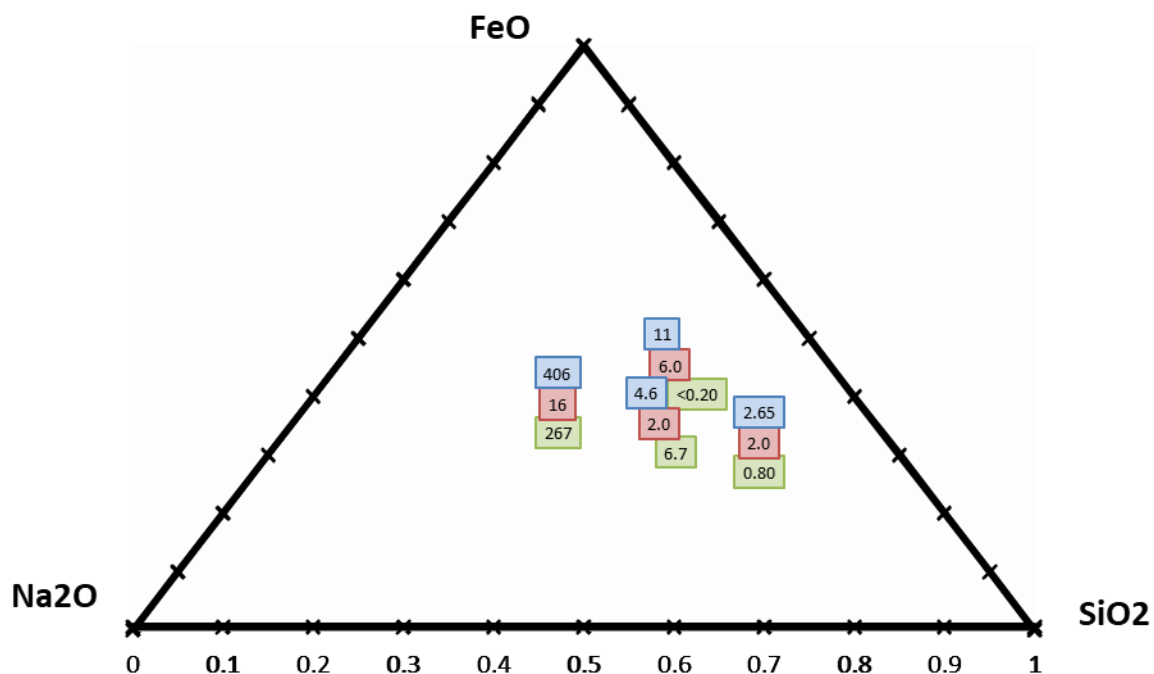


Figure 6.28 TCLP Leach Results (in ppm) for Barium (blue), Lead (red), and Arsenic (green) overlaid on the Na_2O - FeO - SiO_2 ternary diagram. Lead values are centered on the tests' targeted mole percent compositions.

Four more barium-doped samples were prepared and leached. These tests' compositions were targeted as 60:20:20 mol% for each component ($\text{Na}_2\text{O}:\text{FeO}:\text{SiO}_2$) as well as the center, 33:33:33 mol%. They were all cooled at the slow rate (2 °C/min) used previously. These composition outlier tests' data is plotted along with the initial four compositions in Figure 6.29. There, it can be seen that the region whose samples produced the highest extract concentrations were not the low-silica ones – the 60:20:20 sample leached 8.5 ppm and the iron outlier leached 37 ppm – but the region approximately in the center of the phase diagram, where similar to the 406 ppm leached by the high-sodium sample, 269 ppm barium was leached.

Two of the pseudo-binary phase diagrams generated by Moosavi-Khoonsari are presented again in Figure 6.30; one along the FeO - Na_2SiO_3 join and one along the Fe_2SiO_4 - Na_4SiO_4 join. Also shown in Figure 6.31 is an overlay of the TCLP experimental compositions on the liquidus contour plot, with solid and dashed arrows representing the respective pseudo-binary joins. The ternary phase, $\text{Na}_2\text{FeSiO}_4$, lies in the center of each figure, and is the point at which they cross.

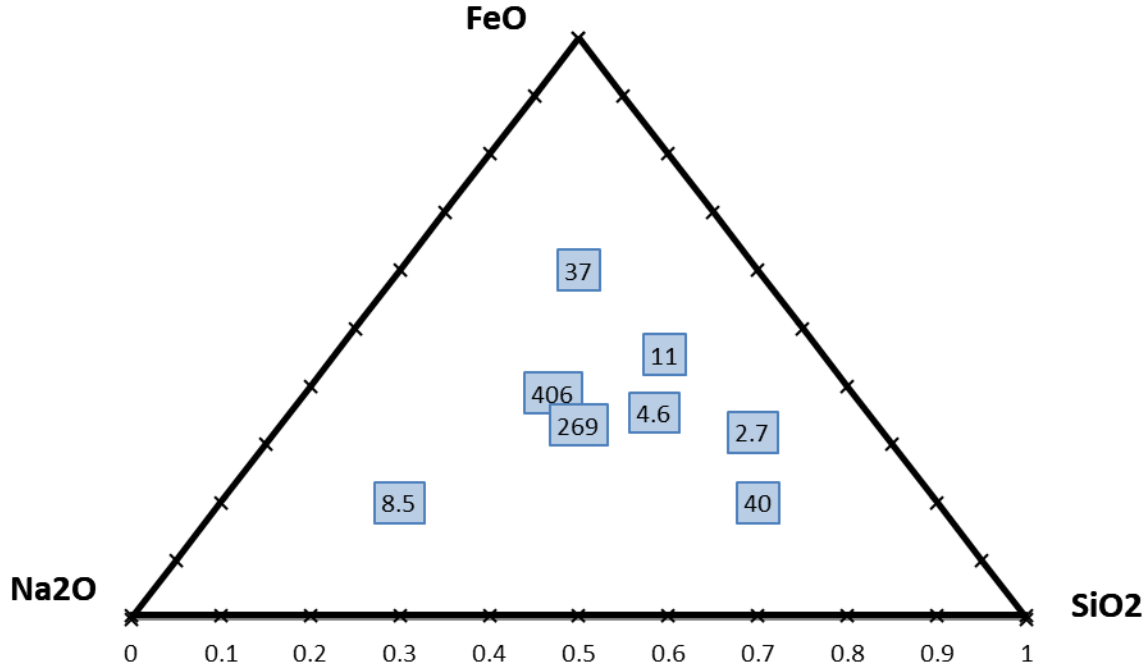


Figure 6.29 TCLP Leach Results (in ppm) for all Barium tests. Values are centered on the tests' targeted mole percent compositions.

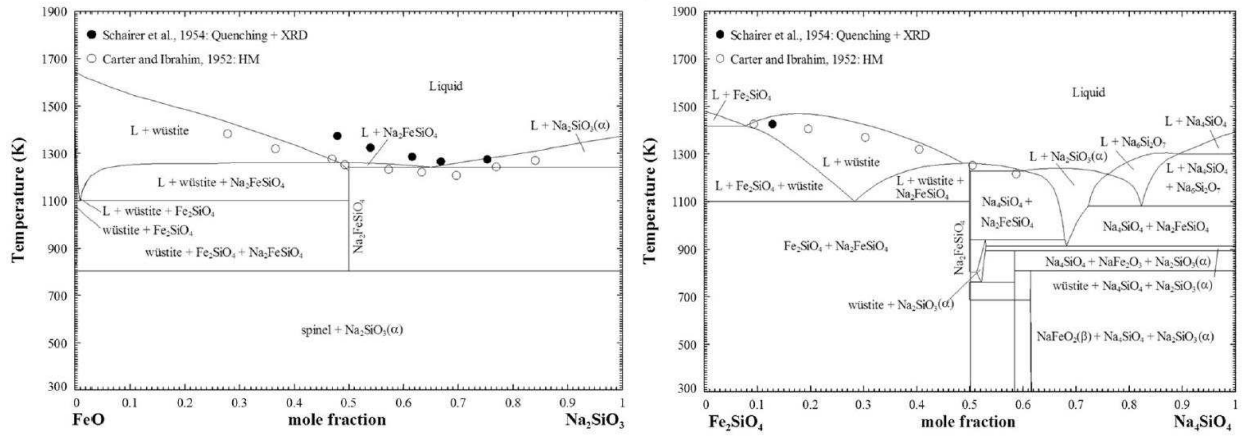


Figure 6.30 Pseudo-Binary Phase Diagrams for FeO-Na₂SiO₃ (left) and Fe₂SiO₄-Na₄SiO₄ (right).

In Figure 6.31 the locations of the experimental points if they were along the binary pseudo-diagrams can be seen. If the composition of the center sample were perfect, it would form one single phase. The initial high-sodium sample would lie slightly to the left of the centerline in the left image in Figure 6.30. The 60-20-20 point would be at the 0.4 mole fraction in the figure.

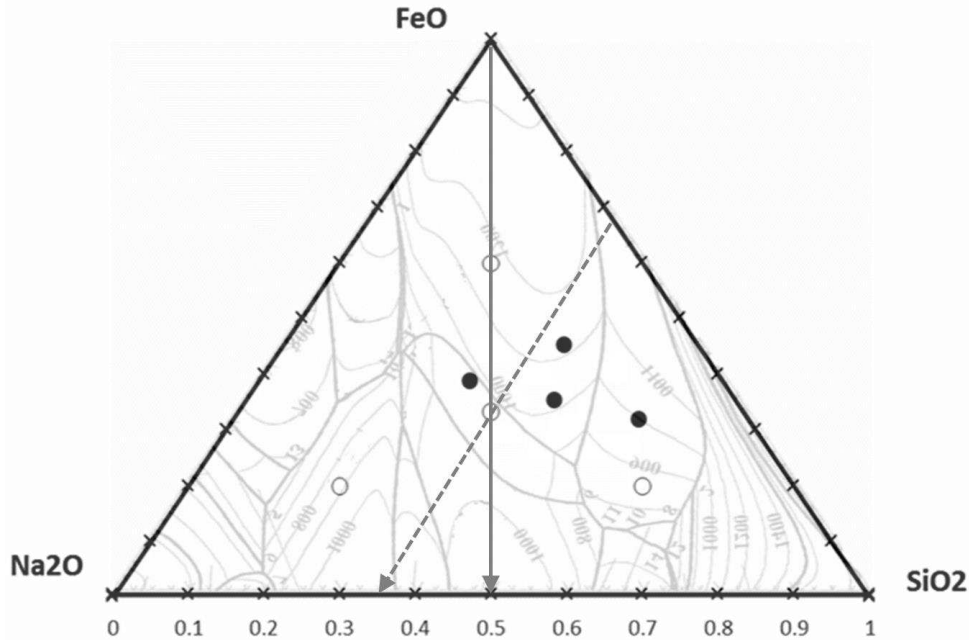


Figure 6.31 Overlay of TCLP Experimental Points onto Liquidus Contours. The dashed line is the $\text{Fe}_2\text{SiO}_4\text{-Na}_2\text{SiO}_4$ join and the solid line is the $\text{FeO-Na}_2\text{SiO}_3$ join.

The appearance of the iron oxide primary phase in the Sample 7 EDS images (specifically Figure 6.19) suggests that all three of these compositions remained to the left of the centerline. Thus, all three would have formed primary wüstite, a large amount of $\text{Na}_2\text{FeSiO}_4$, and a final wüstite and fayalite eutectic. The right half of the right binary join displays the complex sodium silicates which form at sodium-rich compositions of the ternary space. Although there is no diagram to display phases in the region between the 60-20-20 and 20-60-20 points (ie, the left side of the phase diagram), the following proposal is given.

Sample 7 showed evidence of primary iron oxide in its EDS images. Thus, its composition lies to the left of the centerline in Figure 6.30-Left. However, there is more sodium in that sample than for it to perfectly fit on that pseudo-binary join. Comparison of the right-hand sides of the two binary joins reveals that adding more sodium may drastically increase the complexity of the possible phases. This, combined with a eutectic valley beyond the composition of Sample 7, suggests that there are complex sodium silicate phases present as Sample 7 (and the 33-33-33 sample) cool. Noting also the intrusion of the liquid region terminating at approximately 0.7 mole fraction Na_2SiO_4 there exists the possibility for the barium to remain in the liquid until a final barium silicate and sodium silicate solidifies at around 700 °C. This phase development stands in contrast to that of the other samples, which would form iron oxide solutions

and sodium-iron-silicates. Fayalite was not seen in the EDS images, and its lack of presence has been suggested to be due to the greater ease of infiltration of the sodium ions into the silicate network.

The cooling rate range was extended for barium as well. Two more rates were investigated using the high sodium and high silicon composition: an extra-fast water quench and an extra-slow rate of 0.5 °C/min. For the high-sodium sample, it can be seen that as the cooling rate is decreased, more barium will leach. Table 6.7 shows that the quenched sample only leached 3 ppm Ba, while the slowest-cooled sample leached 65 ppm Ba. Although this is still under the 100 ppm regulatory limit, it is noted that this sample was only doped with 1 wt% Ba. Samples with similar compositions which were cooled slowly leached several hundred ppm Ba.

The trend for the high-silica sample is not as apparent. The extreme samples leached more than the moderate ones: 1.63 and 1.35 ppm for the fast-cooled and slow-cooled samples versus 11 ppm Ba for the extra-fast sample and 28 ppm Ba for the extra-slow sample. Given that the repeatability of the samples is ± 3 ppm, the moderate samples are essentially equal. The high amount leached from the quenched samples is likely a function of its particle size. Figure 6.32 shows the two quenched samples side-by-side. In the image, it is apparent that the particle size distribution of sample S is finer than that of sample N and that less mass was recovered for sample S. Most of the slag product for Sample S was used for the TCLP leach, while Sample N was split in half. Therefore, the sample had a higher specific surface area, which would have increased the amount leached. It has been shown (Figure 3.31) that higher-density slags will have a smaller particle size when quenched.



Figure 6.32 Image of Quenched Samples N (left) and S (right), taken after drying.

Table 6.7 Barium Leached from Temperature Outlier Tests.

Sample	BaO, wt%	Cooling Rate	Extract ppm Ba
N	1.86	Extra Fast	3.02
	1.83	Fast	6.57
	1.83	Slow	6.13
	1.86	Extra Slow	64.86
S	1.86	Extra Fast	11.33
	1.83	Fast	1.63
	1.83	Slow	1.35
	1.86	Extra Slow	28.22

CHAPTER SEVEN ECONOMIC ANALYSIS

An economic estimate was made to show that increasing the slag TCLP pass rate without affecting the lead throughput would increase a smelter's daily profit. A simple profit function (Equation 7.1) was developed:

$$\begin{aligned}
 \text{Daily Profit} = & \frac{\$}{\text{ton Pb}} \times \frac{\text{tons Pb}}{\text{day}} \\
 & - \frac{\text{tons Pb}}{\text{day}} \times \frac{\text{tons slag}}{\text{tons Pb}} \times \left(\begin{aligned} & \frac{\$}{\text{ton NH Slag}} \times \frac{\text{tons NH Slag}}{\text{tons Slag}} \\ & + \left(\frac{\$/\text{ton Haz Slag}}{\$/\text{ton NH Slag}} \right) \times \frac{\$}{\text{ton NH Slag}} \times \frac{\text{tons Haz Slag}}{\text{tons Slag}} \end{aligned} \right) \quad (7.1)
 \end{aligned}$$

The equation consists of terms which generate revenue: the daily throughput and price per ton of lead; and terms which affect the cost of slag disposal: slag-to-lead ratio, TCLP pass rate (written as tons of nonhazardous slag per total tons of slag produced), and the disposal costs of nonhazardous and hazardous slag (the latter of which is written as a factor multiplied times the former). Using that equation, the sensitivity of the profit to changes in these factors was analyzed. The analysis is presented graphically in Figure 7.1.

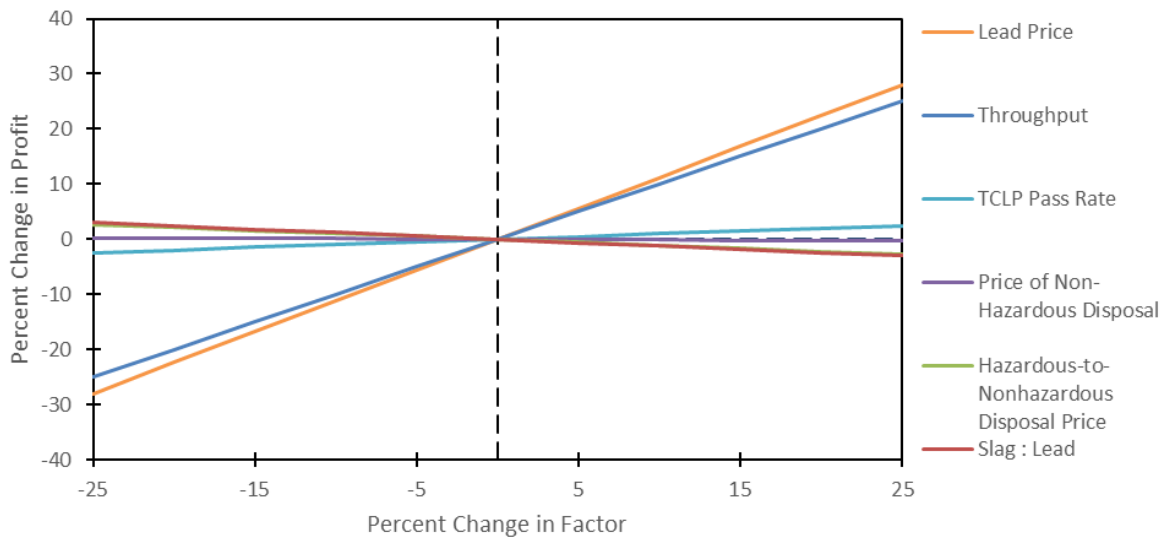


Figure 7.1 Daily Profit Sensitivity Analysis.

The throughput and price per ton of lead strongly positively influenced the daily profit. Compared to those factors, the influence of the TCLP rate was slight, but it was still positive: increasing the TCLP pass rate would increase daily profit. To better compare the remaining factors, the data is re-plotted in Figure 7.2 excluding the lead price and throughput. An increase in the hazardous disposal price would decrease daily profit more than an increase in non-hazardous disposal. (The equation was modified so that the increase in nonhazardous price did not increase the hazardous price.) An increase in the hazardous price would decrease profit slightly more than an increase in the slag-to-lead ratio, and slightly more than an equal-percent change in the TCLP pass rate would increase it.

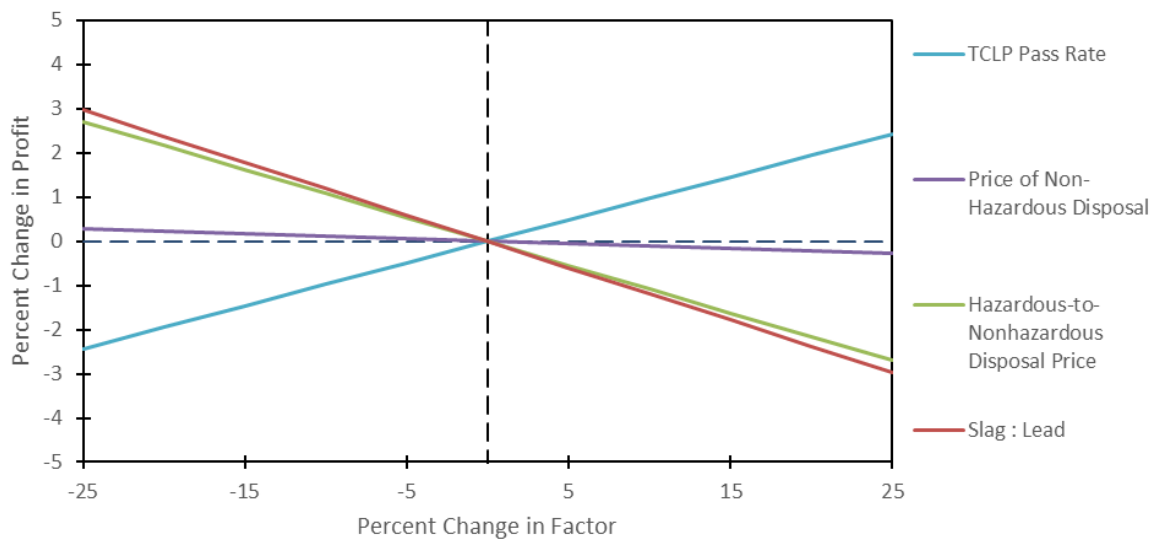


Figure 7.2 Daily Profit Sensitivity Analysis, Excluding Lead Price and Throughput.

It is clear from the figure that the production and sale of lead have the most significant effects on the daily profit. Any process changes aimed at controlling the characteristics of the slag (viscosity or TCLP pass rate) would therefore only be carried out if they do not produce more slag (especially hazardous slag) or sacrifice production of lead. The economic benefit of such a change, should it be enacted, would be partially offset by an increase in capital costs for new monitoring or process equipment as well as increased operating costs related to the labor or energy required to implement new process controls.

CHAPTER EIGHT CONCLUSIONS

Slag viscosity increased with decreasing temperature and increasing silica content. At constant silica content, more iron led to a higher viscosity while more sodium led to a lower viscosity. An Arrhenius-type model was produced to predict slag viscosity as a function of composition and temperature. It showed good agreement between predicted and measured values. Density measurements conducted by this study were not precise enough to establish trends with temperature or composition.

The slag samples tested in this study formed iron oxides and sodium silicates. Satmagan analysis suggested the iron was mostly, but not completely, reduced. HSC modeling to match the Satmagan-determined magnetite content predicts a ferric content of $Fe^{3+}/\Sigma Fe = 0.167$. The impurities formed barium silicates and sodium-barium-silicates, lead silicates, and sodium arsenates.

In the composition region studied, the samples with more silicon tended to leach less. Further investigation revealed that compositions in the center of the phase diagram (not simply those with less silica) produced extracts with the highest concentration of barium (which exceeded the TCLP regulatory limits). Similarly-high extract concentrations were seen with lead and arsenic from the same high-sodium composition.

Composition appears to be a more significant predictor of the extract impurity concentration than temperature in the moderate range of cooling rates. However, when quenching and extra-slow cooling are considered, the cooling rate becomes significant. Barium concentrations were higher for the high-sodium samples which had been cooled more slowly. Quenching, however, can lead to morphological effects which can be detrimental when high-silicon compositions are used.

Relating the two phenomena, the compositions which had the lowest viscosities also leached the most. While this would be beneficial for phase separation (as viscosity is in the denominator for terminal velocity of a sphere in a fluid), the leaching characteristics of this slag when solidified would be industrially undesirable.

An economic incentive for avoiding this region is that increasing the TCLP pass rate will reduce the expense of hazardous slag disposal. By increasing the TCLP pass rate by 25%, daily profit can be increased by 2.43%.

CHAPTER NINE

RECOMMENDATIONS FOR FUTURE WORK

Regarding the viscosity data, tests should be performed while holding the melts at a given temperature immediately and after a certain amount of time has elapsed. This would elucidate the effects of potential precipitation, which, over time, would increase the melts' apparent viscosity. The tests should also be performed on more-complicated systems (five to ten components) to validate the empirical model proposed.

The main shortcoming of the density investigation was its lack of precision. Multiple elements of the experimental setup can be altered to improve that precision. A platinum double-bob spindle should be used, as that has been shown to be the most accurate. If an enclosure were placed around the bob, it would be protected from convective currents from the furnace and melt, which would reduce the error generated from a swinging bob. Longer equilibration times would ensure the bob has reached the correct height and thus that the proper mass is recorded. A finer mechanism for adjusting the height would reduce the error in the height measurement, as well as prevent constant adjustment if the desired height is missed.

A broader range of compositions should be investigated to determine the actual phase development. These could be thermodynamic modelling and cooling from different temperatures. Combined with quantitative phase analysis (such as QEMSCAN), this would show the actual phase development.

The dramatically increased leaching of all impurities towards the center of the phase diagram should be investigated more closely. A study could be conducted which includes compositions spaced at regular intervals between the points in this study. Quantitative before-and-after-leaching imagery would show which phases become more prominent with composition, as well as which are more likely to disappear. If the sample composition were known and the leach solutions were analyzed, a mass balance could be created to back up the "leachable" phases assertion. A thorough literature search or laboratory investigation of pure compounds could also determine their relative solubility in acetic acid and their respective leaching kinetics.

REFERENCES

- [1] P. B. Queneau, R. Leiby, and R. Robinson, "Recycling Lead and Zinc in the United States," *World of Metallurgy - ERZMETALL*, 2015.
- [2] M. W. Iles, *Lead-Smelting*. New York: John Wiley & Sons, 1902.
- [3] R. W. Ruddle, "Difficulties Encountered in Smelting in the Lead Blast Furnace," *Institution of Mining and Metallurgy*, 1957.
- [4] P. B. Queneau, "MTGN 527 Lecture," *Colorado School of Mines*, 2013.
- [5] D. Schriener, P. R. Taylor, and J. Grogan, "A Review of Slag Chemistry in Lead Recycling," in *Advances in Molten Slags, Fluxes, and Salts: Proceedings of The 10th International Conference on Molten Slags, Fluxes and Salts (MOLTEN16)*, Seattle, USA, 2016, pp. 879–888.
- [6] F. Kongoli, "Kongoli (2003) Slags And Fluxes In Pyrometallurgical Processes (Keynote).pdf," in *Metallurgical and Materials Processing: Principles and Technologies*, vol. 1, F. Kongoli, K. Itagaki, C. Yamaguchi, and H. Y. Sohn, Eds. 2003.
- [7] H. Flood and K. Grjotheim, "Thermodynamic Calculation of Slag Equilibria," *J. Iron Steel Inst.*, 1952.
- [8] J. F. Elliott, D. C. Lynch, and T. B. Braun, "A Criticism of the Flood-Grjotheim Ionic Treatment of Slag-Equilibria," *Metall. Trans. B*, vol. 6B, 1975.
- [9] M. Blander, "Inconsistencies in a criticism of the Flood-Grjotheim Treatment," *Metall. Trans. B*, vol. 8B, 1977.
- [10] K. Grjotheim and M. K. Brun, "Application of the Flood-Grjotheim Thermodynamic Treatment to the Slag-Metal Equilibria," *The Metallurgical Society of CIM*, 1977.
- [11] D. R. Poirier and G. H. Geiger, *Transport Phenomena in Materials Processing. The Minerals, Metals & Materials Society*, 1994.
- [12] T. Rosenquist, *Principles of Extractive Metallurgy*. USA: McGraw-Hill, Inc., 1974.
- [13] L. J. Beyers, G. A. Brooks, B. Blanpain, and F. Verhaeghe, "Effects of Structure on the Thermodynamic and Transport Properties of Na₂O-CaO-SiO₂-FeO-Fe₂O₃ Melts," in *Advances in Molten Slags, Fluxes, and Salts: Proceedings of The 10th International Conference on Molten Slags, Fluxes and Salts (MOLTEN16)*, Seattle, USA, 2016, pp. 511–518.
- [14] B. O. Mysen, "Magmatic Silicate Melts: Relations between bulk composition, structure and properties," in *Magmatic Processes: Physicochemical Principles*, The Geochemical Society, 1987, pp. 375–399.
- [15] Z. Wang, T. F. Cooney, and S. K. Sharma, "High Temperature Structural Investigation of Na₂O-0.5Fe₂O₃-3SiO₂ and Na₂O-FeO-3SiO₂ Melts and Glasses," *Contrib. Mineral. Petrol.*, vol. 115, pp. 112–122, 1993.

- [16] V. C. Kress and I. S. E. Carmichael, "Stoichiometry of the iron oxidation reaction in silicate melts," *Am. Mineral.*, vol. 73, pp. 1267–1274, 1988.
- [17] D. B. Dingwell and D. Virgo, "The Effect of Oxidation State on the Viscosity of melts in the system Na₂O-FeO-Fe₂O₃-SiO₂," *Geochim. Cosmochim. Acta*, vol. 51, pp. 195–205, 1987.
- [18] S. Sridhar, "Estimation Models for Molten Slag and Alloy Viscosities," *J. Miner. Met. Mater. Soc.*, pp. 46–50, 2002.
- [19] H. D. Weymann, "On the Hole Theory of Viscosity, Compressibility, and Expansivity of Liquids," *Kolloid-Z. Z. Für Polym.*, vol. 181, no. 2, pp. 131–137, 1962.
- [20] G. Urbain and M. Boiret, "Viscosities of Liquid Silicates," *Ironmak. Steelmak.*, vol. 17, no. 4, pp. 255–260, 1990.
- [21] P. V. Riboud and M. Larrecq, "Lubrication and Heat Transfer in a Continuous Casting Mold," *Rev. Metall.*, vol. 78, pp. 29–44, 1981.
- [22] K. C. Mills, L. Chapman, A. B. Fox, and S. Sridhar, "'Round robin' project on the estimation of slag viscosities," *Scand. J. Metall.*, vol. 30, pp. 396–403, 2001.
- [23] K. C. Mills, "Standard Reference Material for High Temperature Viscosity Measurements: Results of Interlaboratory Comparison Programme," National Physical Laboratory, DMA(A) 175, 1989.
- [24] J. R. Van Wazer, J. W. Lyons, K. Y. Kim, and R. E. Colwell, *Viscosity and Flow Measurement*. John Wiley & Sons, 1963.
- [25] S. Wright and W. Y. Kim, "Viscosity Measurement at the International Conferences on Molten Slags and Fluxes from 1980 to Present," in *Advances in Molten Slags, Fluxes, and Salts: Proceedings of the 10th International Conference on Molten Slags, Fluxes, and Salts (MOLTEN16)*, Seattle, USA, 2016, pp. 369–395.
- [26] C. P. Broadbent, M. Franken, D. Gould, and K. C. Mills, "Standard Reference Material (SRM) for High Temperature Viscosity Measurements," in *Proceedings of the 4th International Conference on Molten Slags and Fluxes*, Sendai, Japan, 1992, pp. 439–443.
- [27] L. Shartsis and S. Spinner, "Viscosity and Density of Molten Optical Glasses," *J. Res. Natl. Bur. Stand.*, vol. 46, no. 3, pp. 176–194, 1951.
- [28] L. Shartsis, S. Spinner, and W. Capps, "Density, Expansivity, and Viscosity of Molten Alkali Silicates," *J. Am. Ceram. Soc.*, vol. 35, no. 6, pp. 155–160, 1952.
- [29] J. D. Mackenzie, "The Discrete Ion Theory and Viscous Flow in Liquid Silicates," *Trans. Faraday Soc.*, pp. 1488–1493, 1957.
- [30] G. Urbain, "Viscosity of SiO₂-PbO Melts," *Rev. Int. Hautes Tempatures Refract.*, vol. 21, no. 2, pp. 107–111, 1984.
- [31] S. K. Gupta, "Viscosity of PbO-SiO₂ Melts," *Metall. Mater. Trans. B*, vol. 26B, pp. 281–287, 1995.

- [32] D. B. Dingwell and D. Virgo, "Viscosities of Melts in the Na₂O-FeO-Fe₂O₃-SiO₂ System and Factors Controlling Relative Viscosities of Fully Polymerized Silicate Melts," *Geochim. Cosmochim. Acta*, vol. 52, pp. 395–403, 1988.
- [33] S. Sukenaga et al., "Effect of Oxidation State of Iron Ions on the Viscosity of Silicate Melts." .
- [34] R. Altman, G. Stavropoulos, K. Parameswaran, and R. P. Goel, "Viscosity Measurements of Industrial Lead Blast Furnace Slags," in *Physical Chemistry of Extractive Metallurgy*, 1985, pp. 97–116.
- [35] T. P. Battle and J. P. Hager, "Viscosities and activities in lead-smelting slags," *Metall. Trans. B*, vol. 21B, 1990.
- [36] R. G. Reddy and Z. Zhang, "Viscosity Measurements of Lead Slags," in *Recycling of Metals and Engineered Materials*, D. L. Stewart, S. R. Stephens, and J. C. Daley, Eds. The Minerals, Metals & Materials Society, 2000.
- [37] Z. Zhang and R. G. Reddy, "Viscosities Of Lead Silicate Slags," presented at the SME Annual Meeting, 2001.
- [38] J. O. Bockris, J. W. Tomlinson, and J. L. White, "The structure of the liquid silicates: partial molar volumes and expansivities," *Trans. Faraday Soc.*, vol. 52, pp. 299–310, 1956.
- [39] S. A. Nelson and I. S. E. Carmichael, "Partial Molar Volumes of Oxide Components in Silicate Liquids," *Contrib. Mineral. Petrol.*, no. 71, pp. 117–124, 1979.
- [40] D. Dingwell, M. Brearley, and J. E. Dickinson, "Melt Densities in the Na₂O-FeO-Fe₂O₃-SiO₂ System and the Partial Molar Volume of Tetrahedrally-coordinated Ferric Iron in Silicate Melts," *Geochim. Cosmochim. Acta*, vol. 52, pp. 2467–2475, 1988.
- [41] Y. Bottinga and D. F. Weill, "Densities of Liquid Silicate Systems Calculated from Partial Molar Volumes of Oxide Components," *Am. J. Sci.*, vol. 269, pp. 169–182, 1970.
- [42] X. Mo, I. S. E. Carmichael, M. Rivers, and J. Stebbins, "The Partial Molar Volume of Fe₂O₃ in Multicomponent Silicate Liquids and the Pressure Dependence of Oxygen Fugacity in Magmas," *Mineralogical Magazine*, vol. 45, pp. 237–245, 1982.
- [43] R. Lange and I. S. E. Carmichael, "Densities of Na₂O-K₂O-CaO-MgO-FeO-Fe₂O₃-Al₂O₃-TiO₂-SiO₂ Liquids: New Measurements and Derived Partial Molar Properties," *Geochim. Cosmochim. Acta*, vol. 51, pp. 2931–2946, 1987.
- [44] R. Lange and I. S. E. Carmichael, "Ferric-ferrous Equilibria in Na₂O-FeO-Fe₂O₃-SiO₂ melts: Effect of Analytical Techniques on Derived Partial Molar Volumes," *Geochim. Cosmochim. Acta*, vol. 53, pp. 2195–2204, 1989.
- [45] E. Jak and P. C. Hayes, "Phase Equilibria Determination in Complex Slag Systems," presented at the VII International Conference on Molten Slags, Fluxes, and Salts, 2004.
- [46] H. Gaye and J. Lehmann, "Modelling and prediction of reactions involving metals, slags and fluxes," presented at the VII International Conference on Molten Slags Fluxes and Salts. The South African Institute of Mining and Metallurgy, 2004.

- [47] K. Denbigh, *The Principles of Chemical Equilibrium*. Cambridge: University Press, 1963.
- [48] F. Rhines, *Phase Diagrams in Metallurgy: Their Development and Application*. New York: McGraw-Hill, Inc., 1956.
- [49] D. Gaskell, *Introduction to the Thermodynamics of Materials*. New York: Taylor & Francis Group, 2008.
- [50] T. R. Bieler, *Course Pack for MSE 360 - Fundamentals of Microstructural Design*. Michigan State University, 2012.
- [51] E. Moosavi-Khoonsari and I.-H. Jung, "Critical Evaluation and Thermodynamic Optimization of the Na₂O-FeO-Fe₂O₃ System," *Metall. Mater. Trans. B*, vol. 47B, pp. 576–594, 2016.
- [52] M. D. Allendorf and K. E. Spear, "Thermodynamic Analysis of Silica Refractory Corrosion in Glass-Melting Furnaces," *J. Electrochem. Soc.*, vol. 148, no. 2, pp. B59–B67, 2001.
- [53] P. Wu, G. Eriksson, A. D. Pelton, and M. Blander, "Prediction of the Thermodynamic Properties and Phase Diagrams of Silicate Systems - Evaluation of the FeO-MgO-SiO₂ System," *ISIJ Int.*, vol. 33, no. 1, pp. 26–36, 1993.
- [54] A. Romero-Serrano, A. Cruz-Ramirez, B. Zeifert, M. Hallen-Lopez, and A. Hernandez-Ramirez, "Thermodynamic Modeling of the BaO-SiO₂ and SrO-SiO₂ Binary Melts," *Glass Phys. Chem.*, vol. 36, no. 2, pp. 171–178, 2010.
- [55] NIST Standard Reference Database 31. ACerS-NIST Phase Equilibria for Ceramics Program.
- [56] P. T. Carter and M. Ibrahim, "The Ternary System Na₂O-FeO-SiO₂," *J. Soc. Glass Technol.*, vol. 36, no. 170, pp. 156–161, 1952.
- [57] *Slag Atlas*. 1981.
- [58] R. P. Gunawardane and F. P. Glasser, "Phase Equilibria and Crystallization of Melts in the System Na₂O-BaO-SiO₂," *J. Am. Ceram. Soc.*, vol. 57, no. 5, pp. 201–204, 1974.
- [59] D. A. Vinnik, E. A. Trofimov, and D. A. Zhrebtsov, "Experimental Study and Thermodynamic Modeling of Phase Equilibria in BaO-Fe₂O₃ System," *Mater. Sci. Forum*, vol. 843, pp. 16–21, 2016.
- [60] R. J. Gambino and F. Leonhard, "Growth of Barium Ferrite Single Crystals," *J. Am. Ceram. Soc.*, vol. 44, no. 5, pp. 221–224, 1961.
- [61] S. Yamashita, H. Fujiwara, E. Ichise, and M. Iwase, "Thermochemical Activities and Phase Relationships in BaO + SiO₂ + Fe_xO Ternary Slags by Solid Oxide Galvanic Cells at 1673 K," *Trans. Iron Steel Soc.*, pp. 57–63, 1992.
- [62] F. P. Glasser, "New Data on Kentrolite and Melanotekite: Ternary Phase Relations in the System PbO-Fe₂O₃-SiO₂," *Am. Mineral.*, vol. 52, pp. 1085–1093, 1967.
- [63] N. P. Dergacheva, I. Z. Babievskaya, V. A. Krenev, S. N. Meshkova, and Y. V. Rumyantsev, "Thermodynamic Modeling of the Melting of Arsenic Oxide with the Oxides of Sodium, Calcium,

- Magnesium, Iron, Aluminum, and Silicon,” *Russ. J. Inorg. Chem.*, vol. 39, no. 10, pp. 1663–1666, 1994.
- [64] C. J. Beyke, “Characterization study of secondary lead blast furnace slags and mattes,” in *Process Mineralogy XIII: Applications to Beneficiation Problems, Pyrometallurgical Products, Advanced Mineralogical Techniques, Precious Metals, Environmental Concerns, Ceramic Materials, Hydrometallurgy, and Minerals Exploration*, R. D. Hagni, Ed. The Minerals, Metals & Materials Society, 1995.
- [65] A. E. Lewis and A. Hugo, “Characterization and batch testing of a secondary lead slag,” *J. South Afr. Inst. Min. Metall.*, 2000.
- [66] H. Tobo, K. Watanabe, M. Kuwayama, S. Goto, H. Goto, and T. Tanaka, “Effect of Water Granulation Conditions on Density and grain Size of Granulated Blast Furnace Slag,” *ISIJ Int.*, vol. 55, no. 11, pp. 2499–2508, 2015.
- [67] W. F. Pickering, “The Competing Roles of Dissolution, Sorption, and Complex Formation in Element Mobilisation,” in *Weathering: Its Products and Deposits*, Athens, Greece: Theophrastus Publications, 1989, pp. 259–306.
- [68] P. B. Queneau, L. D. May, and D. E. Cregar, “Application of Slag Technology to Recycling of Solid Wastes,” presented at the 1991 Incineration Conference, Knoxville, TN, 1991.
- [69] “Part 261--Identification and Listing of Hazardous Waste,” in *Code of Federal Regulations Title 40: Protection of Environment*, US Environmental Protection Agency, 2011.
- [70] “EPA Test Method 1311 - TCLP, Toxicity Characteristic Leaching Procedure.” 1992.
- [71] S. Jahanshahi, F. R. A. Jorgensen, F. J. Moyle, and L. Zhang, “The Safe Disposal Of Toxic Elements In Slags,” in *Pyrometallurgy for Complex Materials & Wastes*, M. Nilmani, T. Lehner, and W. J. Rankin, Eds. The Minerals, Metals & Materials Society, 1994.
- [72] G. M. Habashy and G. A. Kolta, “Thermal Decomposition of the Hydrates of Barium Hydroxide,” *J. Inorg. Nucl. Chem.*, vol. 34, pp. 57–67, 1972.
- [73] D. Montgomery, *Introduction to Statistical Quality Control*, 7th ed. Hoboken, NJ: John Wiley & Sons, 2013.
- [74] A. Napolitano, P. B. Macedo, and E. G. Hawkins, “Viscosity and Density of Boron Trioxide,” *J. Am. Ceram. Soc.*, vol. 48, no. 12, pp. 613–616, 1965.
- [75] A. Lozhechnikova, “Determination of Slurry’s Viscosity Using Case-Based Reasoning Approach,” Master’s Thesis, Lappeenranta University of Technology, 2011.

APPENDIX A
VISCOSITY DATA

Data for the viscosity tests is presented in the following tables. Values which have been struck through were determined to be unrealistic, either due to high variability in the percent torque value recorded or because it was suspected that precipitation of solid particles was affecting the measurement.

Table A.1 Viscosity Test Data for Sample 1.

	RPM	100	60	50	30	20	12	10	6.0	5.0	4.0	3.0	2.5	2.0	1.5	1.0	0.6	0.5	0.3		
% Torque	1299		24.2	18.7	10.9																
	1199		44.3	36.7	24.1	13.5	8.8														
	1100				71.0	46.7	28.1	23.8	15.1	12.8	10.7	8.9									
	1000						96.0	79.6	49.4	41.6	34.3	26.7	22.8	19.3	15.3	11.1	8.1				
	900														79.9	51.5	32.0	28.1	18.1		
SR	21.40	12.84	10.70	6.42	4.28	2.57	2.14	1.28	1.07	0.86	0.64	0.54	0.43	0.32	0.21	0.13	0.11	0.06			
τ	1299		7,597	5,871	3,422																
	1199		13,908	11,522	7,566	4,238	2,763														
	1100				22,290	14,661	8,822	7,472	4,741	4,018	3,359	2,794									
	1000						30,139	24,990	15,509	13,060	10,768	8,382	7,158	6,059	4,803	3,485	2,543				
	900														25,084	16,168	10,046	8,822	5,682		
η	1299		590	547	531																
	1199		1,080	1,073	1,175	987	1,072														
	1100				3,461	3,414	3,424	3,480	3,680	3,743	3,911	4,338									
	1000						11,698	11,639	12,039	12,165	12,538	13,013	13,335	14,110	14,914	16,230	19,740				
	900														77,886	75,303	77,983	82,175	88,219		
		<i>Intercept as calculated</i>				<i>Intercept set to zero</i>				<i>Brookfield Method</i>											
	TEMP	SLOPE	R ²	INT	log η	SLOPE	R ²	log η	INT	η_{AVG}	R ²	log η					10 ⁴ /T, K	ln η			
	1299	639	0.9918	-753	2.81	569	0.9982	2.75	473	556	0.8082	2.75					6.36	6.34			
	1199	1,090	0.9940	-25	3.04	1,087	0.9987	3.04	1,057	1,077	0.0334	3.03					6.79	6.99			
	1100	3,376	0.9993	392	3.53	3,477	0.9992	3.54	3,934	3,681	0.4367	3.57					7.28	8.15			
	1000	11,226	0.9999	1,140	4.05	11,964	0.9974	4.08	15,781	13,766	0.5003	4.14					7.86	9.39			
	900	75,197	0.9977	-214	4.88	78,005	0.9991	4.89	86,109	77,057	0.4896	4.89					8.53	11.26			
	R ² (10 ⁴ /T)				0.9866			0.9917					0.9951				Ea	1.902E-03			

Table A.2 Viscosity Test Data for Sample 2.

	RPM	100	60	50	30	20	12	10	6.0	5.0	4.0	3.0	2.5	2.0	1.5	1.0	0.6	0.5	0.3		
% Torque	1300																				
	1197		8.5																		
	1097		16.5	13.9	8.2																
	999		44.1	36.8	22.0	14.8	9.2														
	900								68.2	54.2	41.5										
	SR	21.20	12.72	10.60	6.36	4.24	2.54	2.12	1.27	1.06	0.85	0.64	0.53	0.42	0.32	0.21	0.13	0.11	0.06		
τ	1300																				
	1197		4,742																		
	1097		9,204	7,754	4,574																
	999		24,600	20,528	12,272	8,256	5,132														
	900								38,044	30,234	23,150										
	η	1300																			
1197			372																		
1097			722	730	717																
999			1,929	1,932	1,925	1,942	2,012														
900									29,831	28,449	27,229										
			<i>Intercept as calculated</i>				<i>Intercept set to zero</i>				<i>Brookfield Method</i>										
	TEMP	SLOPE	R ²	INT	log η	SLOPE	R ²	log η	INT	η_{AVG}	R ²	log η			$10^4/T, K$						
	1300																				
	1197					373		2.57		372		2.57			6.80		5.92				
	1097	731	0.9995	-56	2.86	726	1.0000	2.86	713	723	0.2734	2.86		7.30		6.59					
	999	1,919	0.9999	159	3.28	1,937	1.0000	3.29	1,990	1,948	0.4577	3.29		7.86		7.57					
	900	35,127	0.9992	-6,759	4.55	-	28,916	0.9987	4.46	-	21,996	28,503	0.9987	4.45	-	-	8.53		10.27		
	R ² ($10^4/T$)				1.0000			0.9945				0.9940			Ea		2.072E-03				

Table A.3 Viscosity Test Data for Sample 5.

	RPM	100	60	50	30	20	12	10	6.0	5.0	4.0	3.0	2.5	2.0	1.5	1.0	0.6	0.5	0.3	
% Torque	1300		4.0																	
	1198		4.2	3.6																
	1100		7.6	5.9																
	998																			
	900																			
SR	21.20	12.72	10.60	6.36	4.24	2.54	2.12	1.27	1.06	0.85	0.64	0.53	0.42	0.32	0.21	0.13	0.11	0.06		
τ	1300		2,231																	
	1198		2,343	2,008																
	1100		4,239	3,291																
	998																			
	900																			
η	1300		175																	
	1198		184	189																
	1100		332	310																
	998																			
	900																			
		<i>Intercept as calculated</i>				<i>Intercept set to zero</i>			<i>Brookfield Method</i>											
TEMP	SLOPE	R ²	INT	log η	SLOPE	R ²	log η	INT	η_{AVG}	R ²	log η		$10^4/T, K$	ln η						
1300					475		2.24		475		2.24		6.36	5.17						
1198	158	1.0000	335	2.20	186	0.9998	2.27	215	186	1.0000	2.27		6.80	5.23						
1100	447	1.0000	-1,450	2.65	324	0.9988	2.51	196	321	1.0000	2.51		7.28	5.78						
998																				
900																				
R ² ($10^4/T$)				1.0000			1.0000				1.0000		Ea	9.475E-04						

Table A.4 Viscosity Test Data for Sample 8.

	RPM	100	60	50	30	20	12	10	6.0	5.0	4.0	3.0	2.5	2.0	1.5	1.0	0.6	0.5	0.3	
% Torque	1300		8.0																	
	1198		17.8	14.0	8.7															
	1100		29.8	23.7	13.3	8.4														
	998		70.2	56.9	32.7	21.0	12.7	10.4	6.7											
	900																			
SR	21.20	12.72	10.60	6.36	4.24	2.54	2.12	1.27	1.06	0.85	0.64	0.53	0.42	0.32	0.21	0.13	0.11	0.06		
τ	1300		4,463																	
	1198		9,929	7,810	4,853															
	1100		16,623	13,220	7,419	4,686														
	998		39,159	31,740	18,241	11,714	7,084	5,801	3,737											
	900																			
η	1300		350																	
	1198		779	735	761															
	1100		1,303	1,244	1,164	1,102														
	998		3,071	2,987	2,861	2,756	2,778	2,729	2,931											
	900																			
		<i>Intercept as calculated</i>				<i>Intercept set to zero</i>			<i>Brookfield Method</i>											
TEMP	SLOPE	R ²	INT	log η	SLOPE	R ²	log η	INT	η_{AVG}	R ²	log η		10 ⁴ /T, K	ln η						
1300					351		2.55		350		2.54		6.36	5.86						
1198	784	0.9910	-223	2.89	763	0.9993	2.88	744	758	0.0470	2.88		6.80	6.64						
1100	1,400	0.9986	-1,383	3.15	1,259	0.9978	3.10	1,010	1,203	0.9931	3.08		7.28	7.14						
998	3,099	0.9986	-862	3.49	2,999	0.9989	3.48	2,745	2,873	0.6082	3.46		7.87	8.01						
900																				
R ² (10 ⁴ /T)				0.9987			0.9922				0.9900		Ea	1.148E-03						

Table A.5 Viscosity Test Data for Sample 12.

	RPM	100	60	50	30	20	12	10	6.0	5.0	4.0	3.0	2.5	2.0	1.5	1.0	0.6	0.5	0.3	
% Torque	1300		68.9	59.9	36.5	24.4	15.0	12.8												
	1200				67.4	45.3	28.1	23.3	14.7	12.4	10.2									
	1097						76.2	59.9	36.9	29.8	25.2	19.4	16.3	13.6	10.7					
	1000										94.0	67.9	56.1	45.6	35.4	25.0	16.7	14.3	10.9	
	900																			
	SR	21.40	12.84	10.70	6.42	4.28	2.57	2.14	1.28	1.07	0.86	0.64	0.54	0.43	0.32	0.21	0.13	0.11	0.06	
τ	1300		21,631	18,805	11,459	7,660	4,709	4,018												
	1200				21,160	14,222	8,822	7,315	4,615	3,893	3,202									
	1097						23,923	18,805	11,585	9,356	7,911	6,091	5,117	4,270	3,359					
	1000										29,511	21,317	17,612	14,316	11,114	7,849	5,243	4,489	3,422	
	900																			
η	1300		1,679	1,752	1,779	1,784	1,828	1,872												
	1200				3,285	3,312	3,424	3,407	3,582	3,626	3,729									
	1097						9,285	8,759	8,992	8,715	9,212	9,455	9,533	9,943	10,430					
	1000										34,361	33,094	32,811	33,338	34,508	36,555	40,698	41,819	53,126	
	900																			
		<i>Intercept as calculated</i>				<i>Intercept set to zero</i>				<i>Brookfield Method</i>										
	TEMP	SLOPE	R ²	INT	log η	SLOPE	R ²	log η	INT	η_{AVG}	R ²	log η		10 ⁴ /T, K	ln η					
	1300	1,674	0.9987	516	3.22	1,731	0.9993	3.24	1,873	1,782	0.8713	3.25		6.36	7.46					
	1200	3,224	1.0000	458	3.51	3,339	0.9994	3.52	3,673	3,481	0.7646	3.54		6.79	8.11					
	1097	8,945	0.9970	262	3.95	9,110	0.9989	3.96	9,840	9,369	0.3689	3.97		7.30	9.12					
	1000	32,916	0.9966	588	4.52	34,044	0.9980	4.53	44,110	37,812	0.4965	4.58		7.86	10.44					
	900																			
	R ² (10 ⁴ /T)				0.9921			0.9915					0.9892		Ea:	1.660E-03				

Table A.6 Viscosity Test Data for Sample 13.

	RPM	100	60	50	30	20	12	10	6.0	5.0	4.0	3.0	2.5	2.0	1.5	1.0	0.6	0.5	0.3	
% Torque	1298		8.2	6.9	4.3															
	1199		15.0	13.2	8.0															
	1100		27.4	22.5	13.2	8.9														
	1000		56.4	47.6	28.9	19.9	12.4	10.4	6.8											
	900					71.5	42.4	34.9	21.4	18.0	14.9	11.4	9.8							
	SR	21.20	12.72	10.60	6.36	4.24	2.54	2.12	1.27	1.06	0.85	0.64	0.53	0.42	0.32	0.21	0.13	0.11	0.06	
τ	1298		4,574	3,849	2,399															
	1199		8,367	7,363	4,463															
	1100		15,284	12,551	7,363	4,965														
	1000		31,461	26,552	16,121	11,101	6,917	5,801	3,793											
	900							19,468	11,937	10,041	8,312	6,359	5,467							
η	1298		359	362	376															
	1199		656	693	700															
	1100		1,198	1,181	1,155	1,168														
	1000		2,467	2,498	2,528	2,611	2,712	2,729	2,974											
	900							9,159	9,361	9,448	9,776	9,973	10,288							
		<i>Intercept as calculated</i>				<i>Intercept set to zero</i>				<i>Brookfield Method</i>										
	TEMP	SLOPE	R ²	INT	log η	SLOPE	R ²	log η	INT	η_{AVG}	R ²	log η	$10^4/T, K$	ln η						
	1298	342	1.0000	223	2.53	363	0.9998	2.56	394	366	0.9796	2.56	6.37	5.89						
	1199	624	0.9931	558	2.80	677	0.9992	2.83	744	683	0.7140	2.83	6.79	6.52						
	1100	1,218	0.9996	-290	3.09	1,189	0.9998	3.08	1,141	1,176	0.7306	3.07	7.28	7.08						
	1000	2,424	0.9999	733	3.38	2,509	0.9994	3.40	2,837	2,646	0.7080	3.42	7.86	7.83						
	900	8,804	0.9999	776	3.94	9,385	0.9991	3.97	10,367	9,667	0.7905	3.99	8.53	9.15						
	R ² ($10^4/T$)				0.9918			0.9882				0.9892		Ea	1.217E-03					

APPENDIX B
DENSITY DATA

Data for the six density tests is presented in this appendix. Values recorded at each temperature were the height (in centimeters) at which the platform was positioned, the mass recorded at each height, the change in mass between the two submerged points, the volume change from the difference in spindle immersion depths, and the calculated density.

Table B.1 Density Data for Tests 1, 2, and 3.

1	H	m	Δm	Vol	ρ	2	H	m	Δm	Vol	ρ	3	H	m	Δm	Vol	ρ
1300	67.8	44.63				1300	66.25	42.48				1299	65.3	88.65			
	66.7	44.30					65.2	42.04					64.2	88.00			
	65.7	43.86	0.44	0.178	2.47		64.2	41.52	0.52	0.178	2.92		63.2	86.87	1.13	0.317	3.56
1198	67.8	44.67				1197	66.25	42.53				1199	65.3	88.61			
	66.7	44.39					65.2	42.14					64.2	87.97			
	65.7	43.86	0.53	0.178	2.98		64.2	41.64	0.50	0.178	2.81		63.2	86.88	1.09	0.317	3.44
1100	67.8	44.67				1097	66.25	42.28				1100	65.3	88.73			
	66.7	44.37					65.1	41.83					64.2	87.88			
	65.7	43.86	0.51	0.178	2.87		64.15	41.39	0.44	0.169	2.60		63.2	86.94	0.94	0.317	2.97
						999	66.25	42.16				1000	65.3	88.68			
							65.15	41.98					64.2	87.90			
							64.15	41.45	0.53	0.178	2.98		63.1	86.93	0.97	0.349	2.78
						900	66.25	42.12				900	65.3	88.76			
							65.2	42.04					64.2	87.82			
							64.1	41.47	0.57	0.196	2.91		63.2	87.03	0.79	0.317	2.49

Table B.2 Density Data for Tests 4, 5, and 6.

4	H	m	Δm	Vol	ρ	5	H	m	Δm	Vol	ρ	6	H	m	Δm	Vol	ρ
1298	63.4	38.95				1300	69.8	43.50				1300	66.7	90.54			
	62.4	38.52					68.6	43.02					65.7	89.61			
	61.4	38.04	0.48	0.178	2.70		67.6	42.53	0.49	0.178	2.75		64.7	88.69	0.92	0.317	2.90
1199	63.4	39.09				1198	70	43.48				1200	66.7	90.33			
	62.4	38.75					68.6	43.19					65.7	89.10			
	61.4	38.19	0.56	0.178	3.15		67.6	42.65	0.54	0.178	3.03		64.7	88.15	0.95	0.317	3.00
1100	63.4	38.96				1100	70	43.45				1097	66.7	90.77			
	62.4	38.71					68.6	43.19					65.7	89.60			
	61.3	38.24	0.47	0.196	2.40		67.6	42.71	0.48	0.178	2.70		64.7	88.74	0.86	0.317	2.71
1000	63.4	39.14				998	70	43.58				1000	66.7	91.31			
	62.4	38.88					68.6	43.20					65.7	89.69			
	61.3	38.28	0.60	0.196	3.06		67.5	42.63	0.57	0.196	2.91		64.7	88.91	0.78	0.317	2.46
						900	70	43.50				899	66.7	91.86			
							68.6	43.26					65.7	89.32			
							67.6	42.75	0.51	0.178	2.87		64.7	88.17	1.15	0.317	3.63

APPENDIX C
TCLP SAMPLE DATA

Data for the TCLP samples is presented in this appendix. Targeted and actual compositions, recovery (from an assumed 400.00-g charge), and impurity extract compositions are presented in the following tables. Samples are organized by impurity, impurity amount, cooling rate, and composition.

Table C.1 TCLP Leach Data for Barium Oxide-Doped Samples.

Doped	Targeted Compositon, wt%				Targeted Compositon, mol%				Actual Composition					Recovery	Leached			
	%	Cooling Rate	Recipe	Na ₂ O	FeO	SiO ₂	Impurity	Na ₂ O	FeO	SiO ₂	Impurity	Na ₂ O	FeO	SiO ₂	Impurity	Balance	%	ppm Imp.
Barium	8.84	Slow	7	30.16	40.61	24.23	8.84	33.67	39.11	23.23	3.99	29.51	36.61	15.71	9.04	9.13	103	405.9
			6	15.84	47.19	31.99	8.84	18.08	46.48	31.36	4.08	16.40	38.88	27.80	8.63	8.28	70	10.86
			13	21.73	37.41	35.86	8.84	24.59	36.52	34.85	4.04	19.13	32.71	32.60	8.15	7.42	84	4.56
			2	13.30	34.20	47.50	8.84	15.26	33.85	46.79	4.10	12.97	30.38	38.93	8.43	9.28	95	2.65
	8.84	Fast	7	30.16	40.61	24.23	8.84	33.67	39.11	23.23	3.99	28.39	36.87	23.81	8.25	2.69	97	68.08
			6	15.84	47.19	31.99	8.84	18.08	46.48	31.36	4.08	15.81	41.25	31.06	8.89	2.99	81	9.02
			13	21.73	37.41	35.86	8.84	24.59	36.52	34.85	4.04	20.92	33.89	15.71	8.29	21.18	89	5.25
			2	13.30	34.20	47.50	8.84	15.26	33.85	46.79	4.10	13.43	29.89	41.60	8.24	6.83	70	4.16
	1.83	Slow	7	31.43	42.32	25.25	1.83	34.78	40.40	24.00	0.82	28.75	36.98	22.46	1.74	10.07	99	6.13
			6	16.50	49.17	33.33	1.83	18.69	48.05	32.42	0.84	16.73	43.54	24.49	1.78	13.46	69	1.91
			13	22.65	38.98	37.37	1.83	25.42	37.74	36.02	0.83	22.28	33.20	34.99	1.99	7.53	71	2.96
			2	13.86	35.64	49.50	1.83	15.78	35.00	48.38	0.84	13.57	29.30	43.20	1.97	11.95	96	1.35
1.83		Fast	7	31.43	42.32	25.25	1.83	34.78	40.40	24.00	0.82	30.21	38.97	24.15	1.97	4.70	95	6.57
			6	16.50	49.17	33.33	1.83	18.69	48.05	32.42	0.84	16.92	42.69	32.21	1.83	6.35	60	1.69
			13	22.65	38.98	37.37	1.83	25.42	37.74	36.02	0.83	23.04	35.53	32.57	2.18	6.68	74	1.17
			2	13.86	35.64	49.50	1.83	15.78	35.00	48.38	0.84	15.41	33.01	47.93	2.09	1.57	64	1.63
1.86	Extra Slow	7	31.35	42.22	25.18	1.86	34.78	40.40	23.99	0.83	26.69	34.34	19.66	1.86	17.45	98	64.86	
		2	13.83	35.55	49.38	1.86	15.77	34.99	48.38	0.86	8.59	19.44	24.89	1.12	45.96	82	28.22	
	1.86	Extra Fast	7	31.35	42.22	25.18	1.86	34.78	40.40	23.99	0.83	21.17	33.28	20.09	1.30	24.17	91	3.02
			2	13.83	35.55	49.38	1.86	15.77	34.99	48.38	0.86	12.88	26.47	40.55	1.70	18.40	39	11.33
8.84	Slow		51.37	19.85	19.94	8.84	57.60	19.20	19.20	4.01	39.61	15.50	16.04	6.47	22.38	105	8.53	
			16.16	56.19	18.82	8.84	19.15	57.46	19.15	4.24	14.61	34.32	15.74	2.93	32.40	104	36.74	
			16.13	18.69	56.34	8.84	19.15	19.15	57.45	4.24	14.95	14.93	34.82	5.20	30.10	85	39.9	
			27.43	31.79	31.94	8.84	31.95	31.95	31.95	4.16	21.25	24.90	19.30	5.22	29.32	107	269.2	

Table C.2 TCLP Leach Data for Lead Oxide-Doped Samples.

Doped	Targeted Compositon, wt%							Targeted Compositon, mol%				Actual Composition					Recovery	Leached
	%	Cooling Rate	Recipe	Na ₂ O	FeO	SiO ₂	Impurity	Na ₂ O	FeO	SiO ₂	Impurity	Na ₂ O	FeO	SiO ₂	Impurity	Balance	%	ppm Imp.
Lead	5.00	Slow	7	30.16	40.61	24.23	5.00	34.51	40.09	23.81	1.59	29.67	36.03	21.43	4.34	8.53	92	16.4
			6	15.84	47.19	31.99	5.00	18.55	47.67	32.16	1.63	15.72	40.38	28.32	4.52	11.07	68	6.00
			13	21.73	37.41	35.86	5.00	25.22	37.44	35.73	1.61	19.46	33.52	31.01	4.39	11.61	73	2.03
		Fast	2	13.30	34.20	47.50	5.00	15.65	34.72	48.00	1.63	13.43	31.33	39.40	4.34	11.50	97	1.97
			7	30.16	40.61	24.23	5.00	34.51	40.09	23.81	1.59	29.12	34.32	22.33	4.37	9.87	93	5.87
			6	15.84	47.19	31.99	5.00	18.55	47.67	32.16	1.63	16.22	39.04	28.57	4.76	11.41	59	2.66
	1.00	Slow	13	21.73	37.41	35.86	5.00	25.22	37.44	35.73	1.61	20.79	33.08	31.51	4.45	10.17	80	2.01
			2	13.30	34.20	47.50	5.00	15.65	34.72	48.00	1.63	13.86	29.43	41.22	4.07	11.43	59	0.88
			7	31.43	42.32	25.25	1.00	34.96	40.61	24.12	0.31	30.88	40.88	22.82	0.89	4.53	98	0.54
		Fast	6	16.50	49.17	33.33	1.00	18.79	48.30	32.59	0.32	16.88	44.71	32.19	1.03	5.19	99	0.73
			13	22.65	38.98	37.37	1.00	25.55	37.94	36.20	0.31	23.70	33.26	27.93	0.99	14.11	73	0.55
			2	13.86	35.64	49.50	1.00	15.86	35.18	48.64	0.32	14.50	31.17	41.26	0.86	12.21	93	0.42
			7	31.43	42.32	25.25	1.00	34.96	40.61	24.12	0.31	30.75	39.88	23.76	0.99	4.62	92	0.64
			6	16.50	49.17	33.33	1.00	18.79	48.30	32.59	0.32	16.96	43.41	32.45	0.98	6.21	62	0.39
			13	22.65	38.98	37.37	1.00	25.55	37.94	36.20	0.31	22.73	33.11	33.09	0.95	10.12	63	0.85
			2	13.86	35.64	49.50	1.00	15.86	35.18	48.64	0.32	14.10	28.16	41.79	1.04	14.91	55	0.26

Table C.3 TCLP Leach Data for Arsenic Oxide-Doped Samples.

Doped				Targeted Compositon, wt%				Targeted Compositon, mol%				Actual Composition					Recovery	Leached
	%	Cooling Rate	Recipe	Na ₂ O	FeO	SiO ₂	Impurity	Na ₂ O	FeO	SiO ₂	Impurity	Na ₂ O	FeO	SiO ₂	Impurity	Balance	%	ppm Imp.
Arsenic	5.00	Slow	7	30.16	40.61	24.23	5.00	34.44	40.01	23.76	1.79	28.80	36.18	21.77	4.39	8.85	77	267.20
			6	15.84	47.19	31.99	5.00	18.51	47.57	32.10	1.83	14.38	37.39	21.60	3.72	22.91	99	0.20
			13	21.73	37.41	35.86	5.00	25.16	37.36	35.66	1.81	21.46	32.29	30.18	4.79	11.29	64	6.66
		Fast	2	13.30	34.20	47.50	5.00	15.62	34.64	47.90	1.84	13.12	32.31	41.81	4.24	8.52	92	0.78
			7	30.16	40.61	24.23	5.00	34.44	40.01	23.76	1.79	30.72	34.86	21.45	4.54	8.44	61	3.84
			6	15.84	47.19	31.99	5.00	18.51	47.57	32.10	1.83	16.13	42.56	27.33	3.89	10.08	90	1.12
	1.00	Slow	13	21.73	37.41	35.86	5.00	25.16	37.36	35.66	1.81	22.18	32.84	30.03	4.8	10.15	74	1.25
			2	13.30	34.20	47.50	5.00	15.62	34.64	47.90	1.84	13.23	28.88	42.39	5.05	10.46	45	0.45
			7	31.43	42.32	25.25	1.00	34.95	40.59	24.11	0.35	30.38	38.01	23.16	0.98	7.47	75	43.41
		Fast	6	16.50	49.17	33.33	1.00	18.78	48.28	32.58	0.36	17.22	44.03	25.13	1.13	12.49	101	0.20
			13	22.65	38.98	37.37	1.00	25.54	37.92	36.19	0.35	21.60	33.53	28.40	1.07	15.39	71	0.20
			2	13.86	35.64	49.50	1.00	15.85	35.17	48.62	0.36	14.00	33.32	40.87	0.89	10.92	89	0.22

Table C.4 TCLP Leach Data for Quality Control Samples.

	Doped		Targeted Compositon, wt%					Targeted Compositon, mol%					Actual Composition					Recovery	Leached
	%	Cooling Rate	Recipe	Na ₂ O	FeO	SiO ₂	Impurity	Na ₂ O	FeO	SiO ₂	Impurity	Na ₂ O	FeO	SiO ₂	Impurity	Balance	%	ppm Imp.	
Lead	5.00	Slow	2	13.30	34.20	47.50	5.00	15.65	34.72	48.00	1.63	13.43	31.33	39.40	4.34	11.50	97	1.97	
Lead	5.00	Slow	2-R	13.30	34.20	47.50	5.00	15.65	34.72	48.00	1.63	14.91	32.53	42.58	4.27	5.71	96	1.47	
Barium	1.83	Fast	2	13.86	35.64	49.50	1.83	15.84	35.13	48.57	0.46	15.41	33.01	47.93	2.09	1.57	64	1.63	
Barium	1.83	Fast	2-R	13.86	35.64	49.50	1.83	15.84	35.13	48.57	0.46	14.95	32.50	43.65	1.83	7.07	64	1.90	
Barium	1.83	Slow	6	16.50	49.17	33.33	1.83	18.77	48.23	32.54	0.46	16.73	43.54	24.49	1.78	13.46	69	1.91	
Barium	1.83	Slow	6-R	16.50	49.17	33.33	1.83	18.77	48.23	32.54	0.46	16.88	43.12	29.32	1.92	8.76	66	2.14	
Lead	5.00	Fast	6	15.84	47.19	31.99	5.00	18.55	47.67	32.16	1.63	16.22	39.04	28.57	4.76	11.41	59	2.66	
Lead	5.00	Fast	6-R	15.84	47.19	31.99	5.00	18.55	47.67	32.16	1.63	16.00	41.51	33.07	4.51	4.92	62	2.66	
Lead	1.00	Slow	7	31.43	42.32	25.25	1.00	34.96	40.61	24.12	0.31	30.88	40.88	22.82	0.89	4.53	98	0.54	
Lead	1.00	Slow	7-R	31.43	42.32	25.25	1.00	34.97	40.61	24.11	0.31	28.20	38.49	26.12	1.51	5.69	84	0.93	
Barium	8.84	Fast	7	30.16	40.61	24.23	8.84	34.51	40.09	23.81	1.59	29.12	34.32	22.33	4.37	9.87	97	68.08	
Barium	8.84	Fast	7-R	30.16	40.61	24.23	8.84	34.27	39.80	23.63	2.30	28.71	35.57	22.91	8.41	4.40	99	71.81	
Barium	8.84	Slow	13	21.73	37.41	35.86	8.84	25.03	37.17	35.47	2.33	19.13	32.71	32.60	8.15	7.42	84	4.56	
Barium	8.84	Slow	13-R	21.73	37.41	35.86	8.84	25.03	37.17	35.47	2.33	22.36	33.64	15.71	7.76	20.53	70	4.16	
Lead	1.00	Fast	13	22.65	38.98	37.37	1.00	25.55	37.94	36.20	0.31	22.73	33.11	33.09	0.95	10.12	63	0.85	
Lead	1.00	Fast	13-R	22.65	38.98	37.37	1.00	25.55	37.94	36.20	0.31	22.73	35.45	36.04	1.34	4.45	97	0.37	
Arsenic	1.00	Fast	13	22.65	38.98	37.37	1.00	25.54	37.92	36.19	0.35	22.94	35.23	33.51	0.99	7.33	78	22.2	
Arsenic	1.00	Fast	2	13.86	35.64	49.50	1.00	15.85	35.17	48.62	0.36	13.52	26.79	41.47	1.34	16.88	46	8.7	
Arsenic	1.00	Fast	13	22.65	38.98	37.37	1.00	25.54	37.92	36.19	0.35	--	--	--	--	--	86	0.24	